PHOTONICS

CMDITR Review of Undergraduate Research

Contributions from undergraduate research experiences within the
NSF Center on Materials and Devices for Information Technology Research

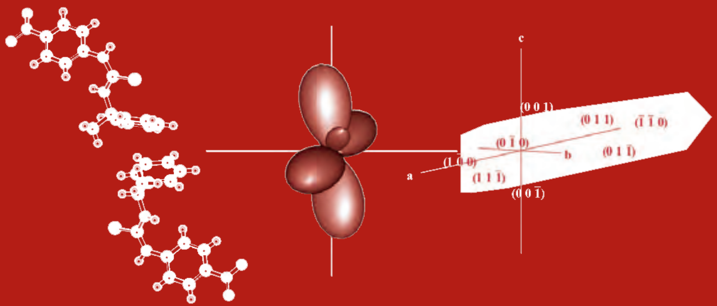

Volume 4, Number 1

This material is based upon work supported by the STC Program of the
National Science Foundation No. DMR 0120967.

Printed in the United States at the University of Washington, Seattle, WA

Inquires should be addressed to:

Center on Materials and Devices for Information Technology Research

Educational Partnership Programs

University of Washington
Department of Chemistry
Box 351700
Seattle, WA 98195-1700

ehrdo@u.washington.edu

http://stc-mditr.org

Volume 4, Number 1

Table of contents

Welcome to the Fourth Edition of CMDITR Review of Undergraduate Research

This volume of the “Photonics” features extended abstracts written by student participants in the National Science Foundation (NSF) Center on Materials and Devices for Information Technology Research (CMDITR) sponsored Summer 2007 Research Experiences for Undergraduates (REU) program.

The REU experience is intended to serve as a catalyst for entry by undergraduates into careers involving science, technology, engineering, and mathematics. The REU experience provides a rich learning opportunity not only for the undergraduate participants who experience research first-hand prior to committing to graduate study, but also for the student mentor, be they faculty members, research scientists, post-doctoral fellows, or graduate students. While working with REU students, mentors develop teaching and mentoring skills, and benefit from reflecting on the excitement of cutting-edge research upon which their careers have been built.

The CMDITR REU Program placed undergraduate students from across the United States in CMDITR research laboratories at the University of Washington, The University of Arizona, and the Georgia Institute of Technology. All of the participants worked on authentic interdisciplinary research projects that contributed to advancements in information technology encompassing activities in chemistry, physics, optics, materials science and engineering. The Program emphasized the teamwork nature of scientific research, and was supplemented by a collection of activities including ethics training and workshops in scientific communication.

The role of “Photonics” is to offer a forum for participates to share their research with their REU peers, future REU students, CMDITR graduate students and faculty, and others interested in the research activities of CMDITR. To learn more about this REU program please visit http://stc-mditr.org/REU.

A special thanks to all of the REU participants for their hard work, to their mentors for their time and patience, and to the REU program coordinators (Olanda Bryant, Kimberly Sierra-Cajas, and Jaclyn Yetter) for their organizational efforts. A final, but important thanks goes to Suzy Hunter and Marya Dominik for their work in the production of this volume.

The extended abstracts included here are presented in alphabetical order by the participant’s last name.

Philip Reid, Editor.

Self-Assembled Rigid Monolayers of 4'-Substituted-biphenyl-4-thiols on Gold Surfaces

ERIKA ABERNATHY, Bethune-Cookman University
Dr. Simon Jones, Marder Lab, Dept. of Chemistry, Georgia Institute of Technology

Introduction

Self-assembly is a coordinated action of independent molecules to produce a larger ordered arrangement, for example on a surface. During the past fifteen years there has been great interest in the preparation of Self-Assembled Monolayers (SAMs) and their use in nanotechnology. Self-assembly is predicted to be an important avenue for fabrication and employment of supramolecular nanostructures with useful properties.[1] Components can be formed in a building block format and can be made up of polymers, DNA and proteins, nanoparticles and/or surfactants. In order for these components to self-assemble they must have very strong attractive interactions at their interfaces. Studies of molecular recognition, biomaterial interfaces, cell growth, crystallization, and many other systems have been proven to be a success when SAMs were used during the design of interfacial interaction. The rigid character of the biphenyl group can result in a molecular dipole moment that affects both the kinetics of biphenylthiol adsorption onto gold surfaces, as well as the equilibrium structure of mixed SAMs,[1,2] and therefore, a variety of surfaces with specific interactions can be produced with fine structural control.[2]

One deficiency of SAMs is that thermal disorder results in surface-gauche effects for SAMs made from flexible alkyl derivatives. Studies show that the cause of this problem occurs when the SAM interacts strongly with another condensed phase. This problem takes place in very polar surface groups, such as alcohol, and this is where the introduced disorder may be considerably important and not to cause restrain to the surface.

Problem

Investigate biphenylthiol SAMs so i) make them first (expensive) and ii) make SAMs with them. Then, send to collaborator after initial characterization.

Materials and Methods

We are interested in improving chemical and/or electronic contact between molecules and surfaces for optoelectronic device applications through the use of conjugated thiol ligands. We plan to investigate the structural and electronic properties of various biphenyl thiols on gold surfaces using Scanning Tunneling Microscopy (STM) in collaboration with the Stellacci group at MIT. The object of my research project is the preparation and characterization of simple model molecules based on a range of donor and acceptor substituted biphenyl thiols that are useful for an initial parameterization. Such molecules are not easily available commercially, but are relatively straightforward to synthesize.

We have examined biphenyl thiols with different substituents by the 4-postion where X= F, Me_2N, H, EtO, or NO_2. These substituents are either electron acceptor or electron donor groups.

Experimental Section

Reaction Scheme:

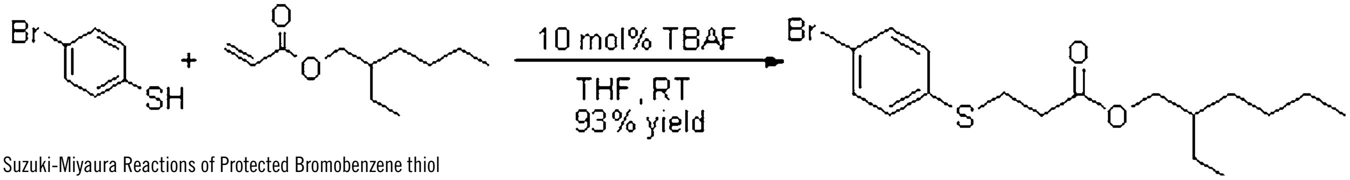

Suzuki-Miyaura Reactions of Protected Bromobenzene thiol

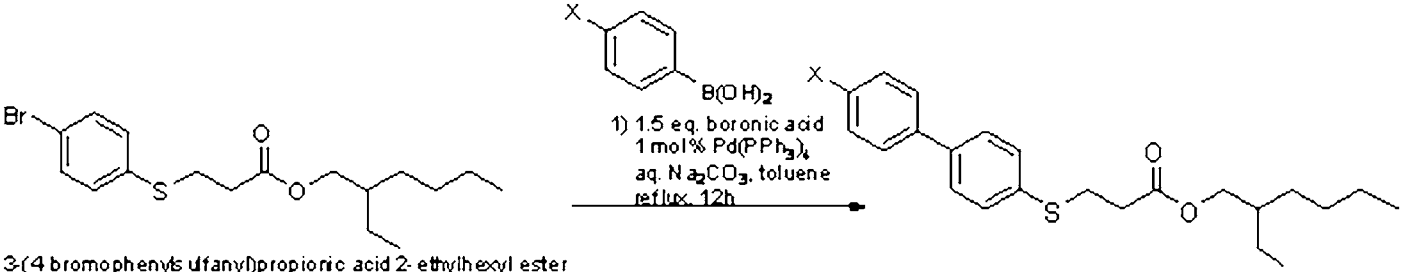

3-(4 bromophenylsulfanyl)propionic acid 2-ethylhexyl ester

De-protection Process

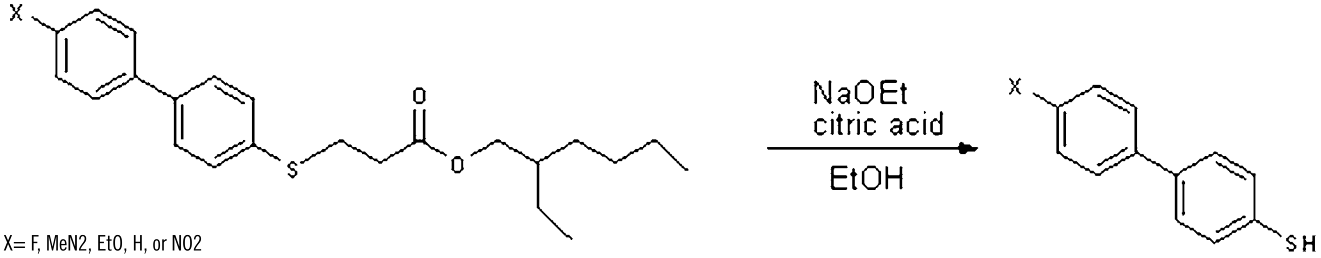

X= F, MeN2, EtO, H, or NO2

TARGETS

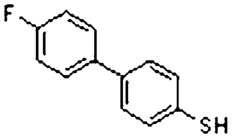

4'-Fluorobiphenyl-4-thiol

98%

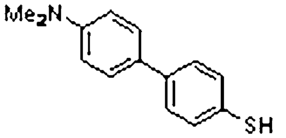

4'-(Dimethylamino)biphenyl-4-thiol

81%

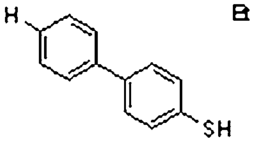

Biphenyl-4-thiol

95%

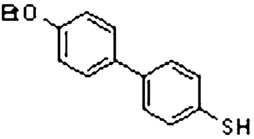

4'-Ethoxybiphenyl-4-thiol

92%

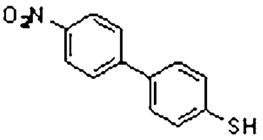

4'-Nitrobiphenyl-4-thiol

32%

3-(4-Bromophenylsulfanyl)propionic Acid 2-Ethylhexyl Ester

To a round-bottom flask were added 4-Bromothiophenol (6.09 g, 32.2 mmol), 2-ethylhexyl acrylate (5.94 g, 32.2 mmol), tetrahydofuran (60 mL), and tetrabutylammonium fluoride (6.75 mL, 32.2 mmol). The mixture was heated at a set temperature of 110° in an oil bath for 20 hours and 45 minutes. The mixture, ethyl acetate (50 mL) and water (30 mL) was poured into separatory funnel. After separation, the aqueous layer was extracted with ethyl acetate (50 mL), and magnesium sulfate was added to the mixture to remove any extra water excess by vacuum filtration. After water was removed, the mixture poured into round-bottom flask which was placed onto rotary evaporator. The crude product was purified by column chromatography on silica gel to afford 3-(4-bromo-phenylsulfanyl)-propionic acid 2-ethylhexyl ester (12.02 g, 50% yield) as a slightly yellowish oil which was characterized by ^{1}H NMR spectroscopy.

General procedure for palladium-catalyzed Suzuki-Miyaura reaction and deprotection

To an oven-dried ampoule flask were added 3-(4-bromo-phenylsulfanyl)-propionic acid 2-ethylhexyl ester (400 mg, 1 mmol), 4-(substituted) phenyl boronic acid (2 mmol), Na_2CO_3 (212 mg, 2 mmol), and catalyst Pd $(PPh_3)_4$ (62 mg, 5 mol %) degassed by three vacuum/ N_2 cycles. Dry toluene (8 mL) and purged water (2.3 mL) were added to the ampoule flask. The mixture was degassed three vacuum/ N_2 cycles and heated at a temperature of 110° C in a oil bath for 15 hours. The mixture was cooled for 30 minutes and ethyl acetate and water were added to the ampoule flask. The mixture was poured into separatory funnel and after separation,

organic layer was extracted from the funnel. Magnesium sulfate was added to the mixture to remove any extra water excess. Magnesium sulfate was removed from solution by vacuum filtration and solution was poured into round-bottom flask and placed onto rotary evaporator. The product was purified by column chromatography on silica gel to afford the 4'-substituted-biphenyl-4-thiol, which was characterized by ^{1}H NMR spectroscopy.

De-protection Process for 4-(Dimethylamino)-biphenylsulfanyl-propionic acid 2-ethylhexyl ester

To a round-bottom flask were added 4-(Dimethylamino)-biphenylsulfanyl-propionic acid 2-ethylhexyl ester (102.5 mg, 0.248 mmol), sodium ethoxide (19.43 mL, 0.248 mmol), and ethanol (14.47 mL, 0.248 mmol). The mixture was stirred at ambient temperature for five hours and was acidified with aqueous citric acid. The mixture was poured into separatory funnel and after separation, organic layer was extracted from the funnel. Magnesium sulfate was added to the mixture to remove any extra water excess. Magnesium sulfate was removed from solution by vacuum filtration and solution was poured into round-bottom flask and placed onto rotary evaporator. Product was dissolved in ethanol and placed into freezer for re-crystallization. The desired product was collected by vacuum filtration and product was allowed to dry. This material was then characterized by ^{1}H NMR spectroscopy.

Applying 4'-(Dimethylamino)-biphenyl-4-thiol onto gold surface: The gold surface was placed into piranha solution for 30 seconds. After removing the gold surface from piranha solution, the gold surface was placed into flask containing thiol product mixed with ethanol as the solvent; making sure that gold surface was completely covered. After about 24 hours, the gold surface was removed from thiol product solvent and cleaned with 200 mL of ethanol and dried by nitrogen gas. The gold surface was placed into clean flask making sure that gold surface was face down and both sides of the metal were dry. The substrate containing the gold surface was characterized by IR-RAS spectroscopy.

Results

Thiol derivatives were prepared using a palladium coupling reaction.[2] 3-(4-bromo-phenylsulfanyl)-propionic acid 2-ethylhexyl ester (50% yield), 4'-(Dimethylamino)-biphenylsulfanyl-propionic acid 2-ethylhexyl ester (92% yield), 4'-Fluorobiphenyl sulfanyl-propionic acid 2-ethylhexyl ester (98% yield), 4'-Ethoxylbiphenyl sulfanyl-propionic acid 2-ethylhexyl ester (81% yield), 4'-Nitrobiphenyl sulfanyl-propionic acid 2-ethylhexyl ester (32% yield), and Biphenyl sulfanyl-propionic acid 2-ethylhexyl ester (95% yield). The 'H NMR spectra are indicative of pure materials.

De-protection The process for 4-(Dimethylamino)-biphenylsulfanyl-propionic acid 2-ethylhexyl ester: process was performed to give 4'-(dimethylamino)-biphenyl-4-thiol in 53% yield.

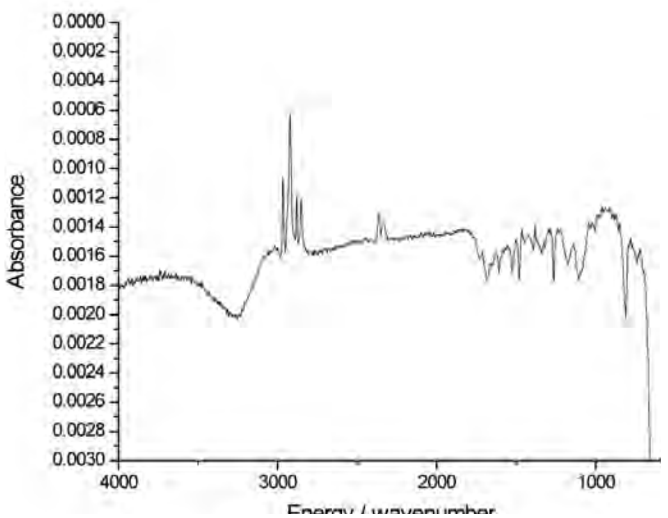

IR-RAS spectrum of 4’-dimethylaminobiphenyl-4-thiol on gold using dodecanethiol-coated gold as a reference:

Conclusion

After completing the proper procedures, and viewing the ‘H NMR spectra, and IR-RAS spectrum, results show that most of the desired compounds were obtained in high yields> 80%. Products that were made will be sent to MIT laboratory where Scanning Tunneling Microscopy experiments will take place.

Acknowledgments:

National Science Foundation (NSF)

Center of Materials and Devices for Information Technology Research (CMDITR) Georgia Institute of Technology

Dr. Seth Marder, Professor: Director of the Center of Organic Photonics and Electronics (COPE), Georgia Tech.

Dr. Simon Jones, Mentor:

Dr. Marder Research Group

REU Program Coordinators

References

1. Ulman, A.; Kang, J. F.; Shnidman, Y.; Liao, S.; Jordan, R.; Choi, G.- Y.; Zaccaro, J.; Myerson, A. S.; Rafailovich, M.; Sokolov, J.; Fleischer, C. *Rev. Mol. Biotechnol.* 2000, 74, 175-188.
2. Kang, J.; Ulman, A.; Liao, S.; Jordan, R.; Yang, G.; Liu, G. *Langmuir* 2001, 17, 95-106.
3. Miyaura, N.; Suzuki, A. *Chem. Rev.* 1995, 95, 2457-2483.
4. Itoh, T.; Mase, T. J. *Org. Chem.*, 2006, 71, 2203-2206.

ERIKA ABERNATHY is currently finishing her senior year at Bethune-Cookman University and after graduation, she plans to enter the Air Force and continue her education.

Electronic Properties of a Series of Fused Polycyclic Organic Structures

ANTOINETTE ADDISON[1,2,] Jean-Luc Brédas[1], Veaceslav Coropceanu[1], Seyhan Salman[1]
Georgia Institute of Technology, School of Chemistry and Biochemistry, Atlanta, Georgia 30332-04001
Florida A&M University, College of Arts and Science, Tallahassee, Florida 323072

Introduction

The commercial market today is dedicated to providing its consumers with more advanced technologies like cellular phones, car stereos, digital cameras or even light powered operating devices. The development of organic-polymer based elements had introduced the possibility of thinner, lighter, cheaper and easier-to-produce devices. The goal with organic based devices is not necessarily to attain or exceed the level of performance of inorganic semiconductor technologies (silicon is still the best), but to benefit from a unique set of characteristics by combining the electrical properties of semiconductors with the properties of typical plastics.[1] Interest in conjugated polymer picked up significantly after the 1976 discovery that a conjugated polymer can be made highly conductive after a redox chemical treatment. By the mid-eighties, many research teams, both in academia and industry, were investigating π-conjugated oligomers and polymers for their nonlinear optical properties and their semiconducting properties, which paved the way to the emergence of the fields of plastic electronics and photonics.[1] Oligoacene-based materials represent the most studied and a promising class of π-conjugated semiconductors that are used as active elements in new generations of plastic (opto)-electronics devices.[2] In particular, pentacene shows very interesting performances as an active semiconductor layer in organic field-effect transistors with hole mobility reaching 2-3 cm^2 V^{-1} s^{-1}.[2,3] The aim of the present project is to study a series of fused polycyclic organic materials containing nitrogen, oxygen, selenium and sulfur. Changing the heteroatom can change the solid state packing and electronic couplings, which can cause an increase in charge mobility and electron charge transfer rate. Studying these fused systems will give an understanding of how electrons and holes move and behave in these systems. Once there is enough knowledge about these systems they probably can be used in organic light emitting diodes (OLEDs), where electrons and hole recombine to emit light, or in photovoltaic devices, where electrons and holes separate to produce a current following light absorption.

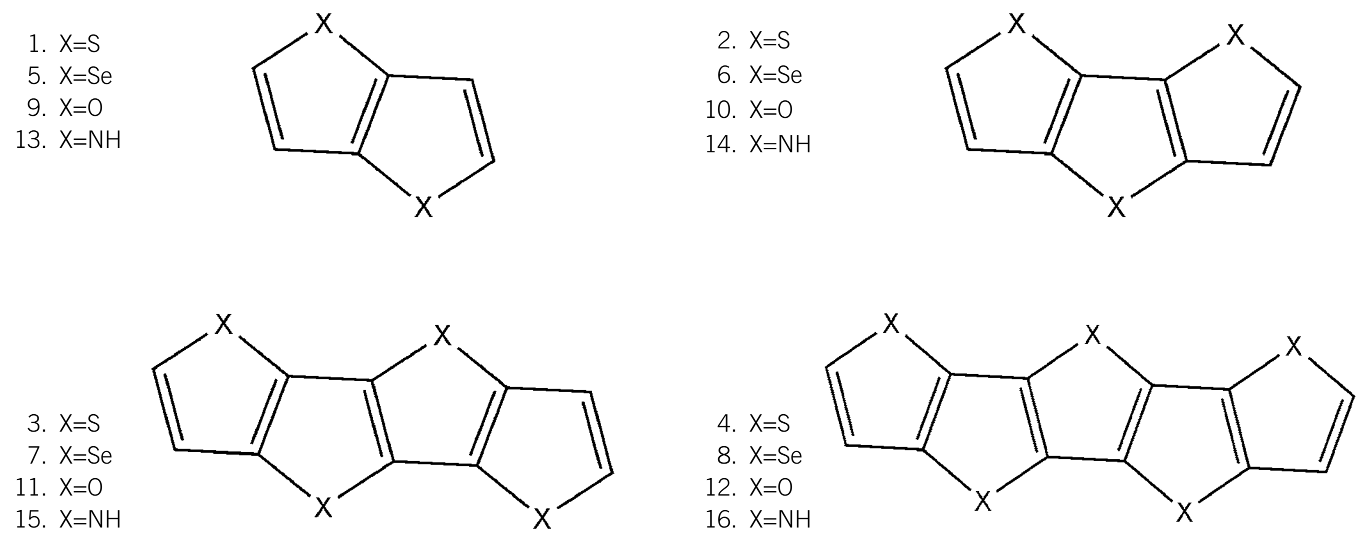

1. X=S
5. X=Se
9. X=O
13. X=NH

2. X=S
6. X=Se
10. X=O
14. X=NH

3. X=S
7. X=Se
11. X=O
15. X=NH

4. X=S
8. X=Se
12. X=O
16. X=NH

FIGURE 1. Chemical structure of the investigated systems.

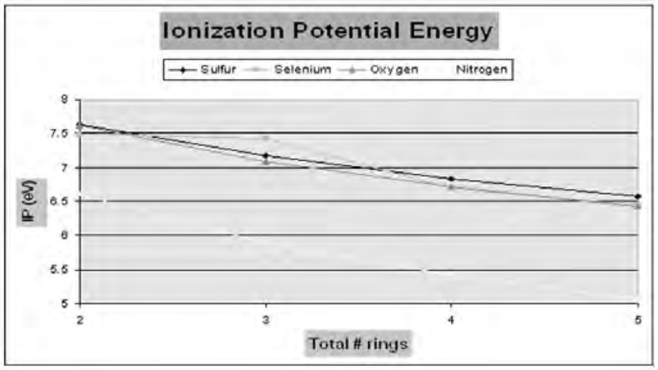

FIGURE 2. Ionization potential energy (eV) of sulfur, selenium, oxygen and nitrogen-based systems as the total number of rings increases.

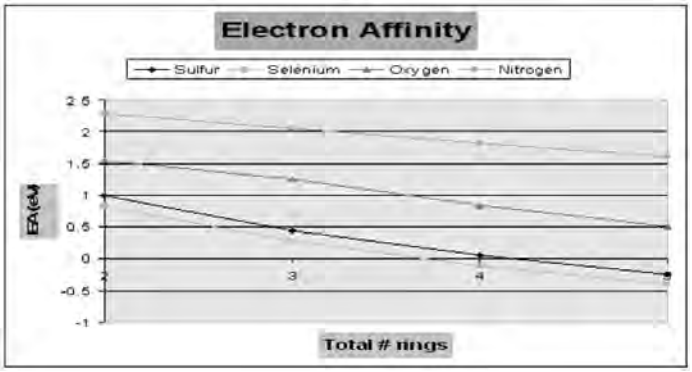

FIGURE 3. Electron affinity (eV) of sulfur, selenium, oxygen and nitrogen based systems as the total number of rings increases.

	HOMO	LUMO	1^{St} Ionization Energy	Affinity
1	-5.770	-0.541	-7.635	-1.004
2	-5.513	-0.882	7.172	0.452
3	-5.311	-1.118	6.828	-0.058
4	-5.180	-1.297	6.580	0.242
5	-5.81	-0.826	7.488	- 0.833
6	-5.672	-1.190	7.427	- 0.286
7	-5.342	-1.450	6.692	0.1011
8	-5.335	1.626	6.445	0.3934
9	-5.46	0.376	7.620	-1.550
10	-5.116	- 0.765	7.088	-1.258
11	-5.116	- 0.765	7.088	-1.258
12	- 4.893	- 1.068	6.710	- 0.842
13	.-4.636	0.985	6.598	-2.296
14	-3.955	0.679	5.89	-2.063
15	-3.870	0.646	5.418	-1.820
16	-3.660	0.489	5.068	-1.624

TABLE 1. The energies of the frontier orbitals, first ionization potential energies, and electron affinities (in eV) of the investigated systems.

Research Method

All geometry optimizations of the neutral, anion and cation states were performed using semiempirical and DFT (Density functional theory) methods. All DFT calculations were done with the Gaussian 98 program package, using the B3LYP functional and 6-31G (d,p) basis set. Table 1 summarizes the energies of highest occupied molecular orbitals (HOMO), lowest unoccupied molecular orbitals (LUMO), ionization potential, and electron affinity. The changes in ionization potential energy and electron affinity as a function of number of rings are shown in Figures 2 and 3. The reorganization energies for hole transfer and electron transfer processes are shown in Table 3. The ionization potential is the energy required to remove an electron from a molecule. This energy is important because it tells us how hard it is to remove an electron from the HOMO. When an electron is removed from HOMO, it gives rise to a hole. The ionization energy was calculated by the difference between total energy of the neutral state and total energy of the cation state. All systems show a decrease in ionization potential with increased number of rings, but the IP's in pyrrole-based systems were 1 eV lower than in the other systems. Pyrrole-based compounds can more easily have an electron removed from their systems than the other systems. Electron affinity is the energy required to add an electron to a molecule. The smaller (more negative) the affinity, the easier it is for the system to accommodate an extra electron in the lowest unoccupied molecular orbital (LUMO). The electron affinity was calculated by the difference between the total energy of the anion state and total energy of the neutral state. All systems show an decrease in their electron affinities as the total number of rings increases. In the case of the selenophene and thiophene systems, these are the only systems that once the ring size reached four for the selenophene series and five for the thiophene series, the affinity became negative. A negative affinity means the anion state is more stable than the neutral state. This type of materials would be excellent for charge transport. Reorganization energy is the energy required for

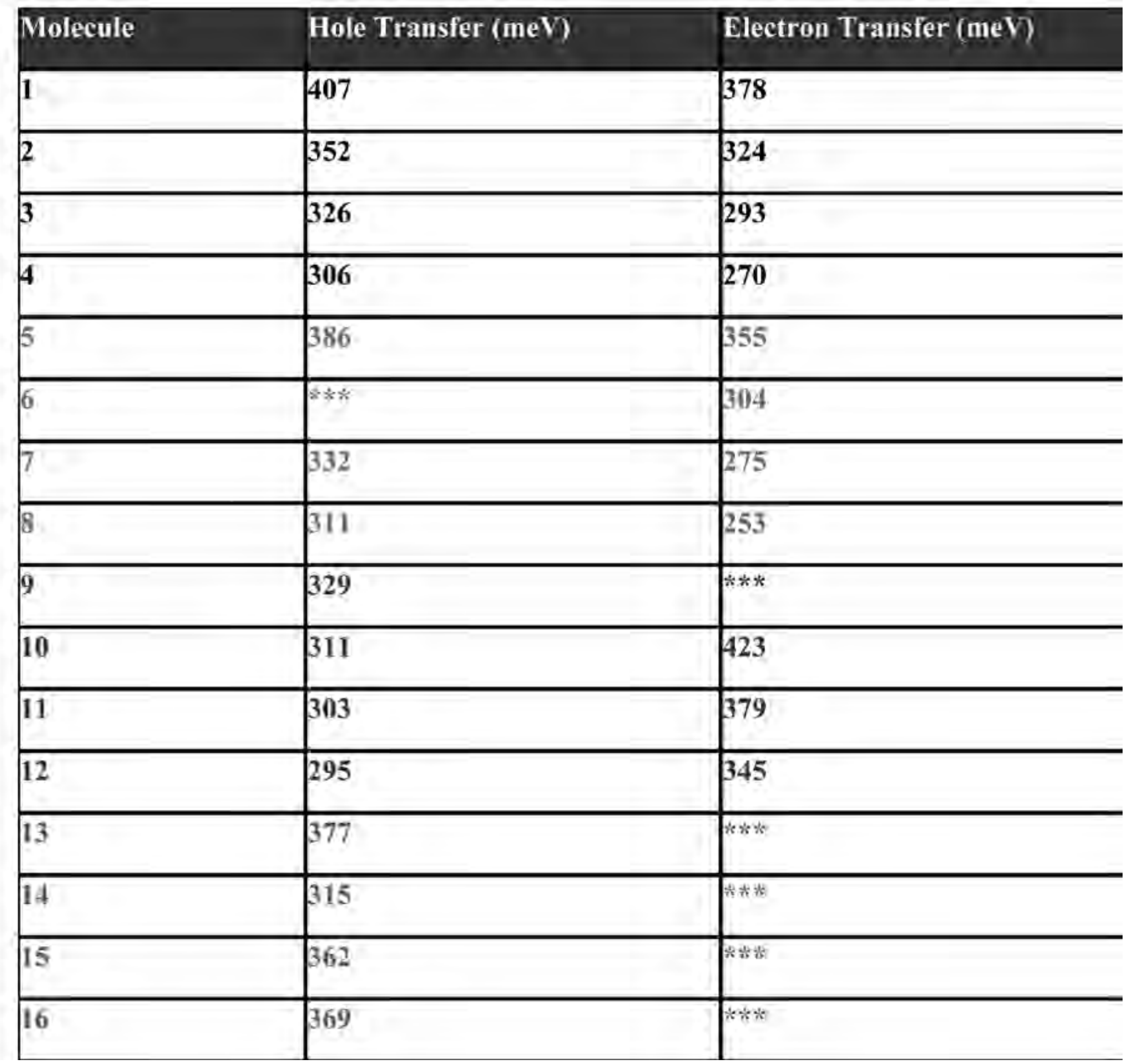

Molecule	Hole Transfer (meV)	Electron Transfer (meV)
1	407	378
2	352	324
3	326	293
4	306	270
5	386	355
6	***	304
7	332	275
8	311	253
9	329	***
10	311	423
11	303	379
12	295	345
13	377	***
14	315	***
15	362	***
16	369	***

TABLE 2. Reorganization energies for electron transfer ET (meV) and hole transfer HT (meV) for the fused systems studied: S, Se, O, N (*** research still in progress).

all structural adjustments (in the reactants and in the surrounding medium) in response to a change in the overall charge distribution corresponding to charge transfer. The reorganization energy for the studied systems showed a similar trend as the oligoacene family (most studied and promising class); as the total number of rings increases, the reorganization energy decreases, but the reorganization energies in the studied systems were three to four times higher in energy. It is very important to have small reorganization energies because as the reorganization energy decreases the electron transfer rate and mobility will increase.

Conclusion

In summary, this work presents an analysis of the electronic properties of the studied fused polycyclic systems. All values of the reorganization energies are higher than the values obtained with oligoacenes. Pyrrole-based systems have the smallest ionization potential energy and selenophene and thiophene based systems have the strongest electron affinity. Future work includes the investigation of the excited states and intermolecular electronic couplings.

Acknowledgements

My research was funded by the National Science Foundation (NSF) and Center on Materials and Devices for Information Technology Research (CDMITR). I would like to thank my advisor Dr. Jean-Luc Brédas, my mentors Dr. Veaceslav Coropceanu, Ms. Seyhan Salman and Ms. PaDreyia Lawson.

References

1. Brédas, J.L.; Bejonne, D.; Coropceanu, V.; Cornil, J.; *Chem Rev.* 2004, 104, 5003.
2. Coropceanu, V.; Kwon, O.; Wex, B.; Kaafarani, B.R.; Gruhn, N.E.; Douglas, N.C; Brédas, J.L.; *Chem Eur. J.* 2006 2073-2080.
3. Boudreault, P.L.T.; Wakim, S.; Blouin, N,; Simard, M.; Tessier, C.; Tao, Y.; Leclerc, M.; J. *Am. Chem. Soc.* 2007 ASAP.

My name is **ANTOINETTE ADDISON**, and I currently attend Florida A&M University where I am working toward earning a degree in Bio-Chemistry. After I graduate Spring 2008, I plan to attend Medical school and eventually explore the career opportunities in clinic research.

Adventures with Carbon Nanotubes:

First Steps Towards the Realization of New Back Contacts for Organic Light Emitting Diodes and Organic PhotoVoltaics

ETHAN AMEZCUA (Cabrillo Community College), Derek Mangelsdorf, Diogenes Placencia, Judith L. Jenkins, Gulraj Chawla,
Dr. Neal R. Armstrong; Hooked on Photonics – University of Arizona at Tucson Department of Chemistry

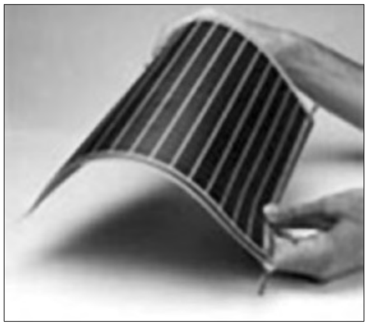

FIGURE 1. Flexible Solar Cell

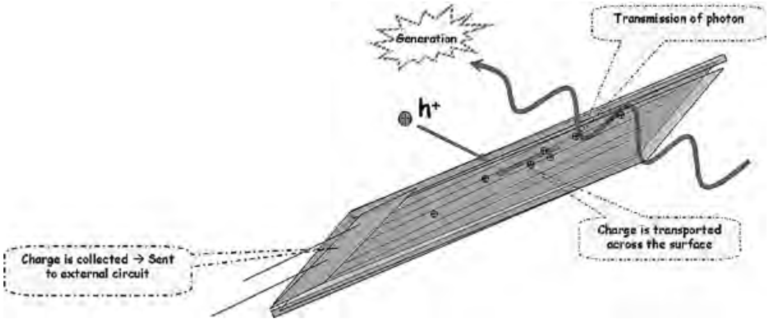

FIGURE 3. The back contact

Introduction

There is a critical need for cheap, energy efficient electrical and optical (EO) materials. One focus is on the transparent, conductive (TC) coatings which are important components for organic photovoltaics and organic light emitting diodes

Optical transparency in these materials is just as important as electrical conductivity, because the active site for absorption (or emission) of light energy is embedded between two conducting layers. The current TC standard material is indium tin oxide (ITO) – yet ITO is the most expensive material in modern EO devices, and is chemically unstable. The objective for this project was to assess the electical properties of different carbon nanotube (CNT) films, and test the hypothesis that this cheap, and perhaps more processable material, may replace the costly, and problematic rare metal-oxide electrodes.

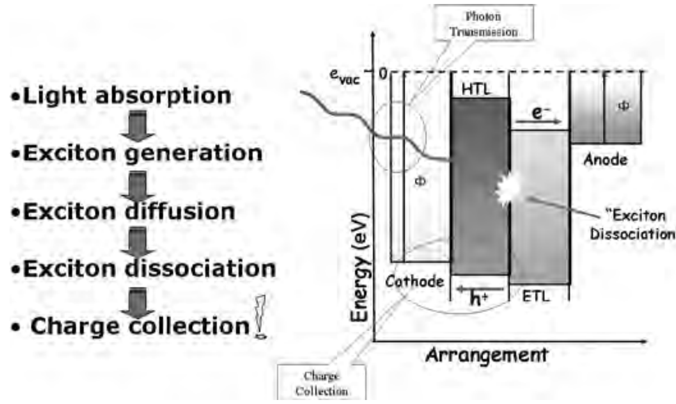

FIGURE 2. Basic schematic of the OPV, which is fundamentally similar to the OLED. Active layers — hole transporting (HTL) and electron transporting (ETL) — sandwiched between two electrodes, one of which *must* be transparent.

The Back Contact

The back contact plays an important role in an organic solar cell. To generate power from light energy, the back contact must:

- Show high electrical conductivity
- Show high optical transparency
- Must present a surface wettable by non-polar organic materials
- Show surface roughness less than 1nm (rms)

The back contact must permit the photons to access the active core of the device; *simultaneously,* the back contact must transport charge that is generated by the active layer.

Previous work has reported that transparent and conducting carbon nanotube electrodes can be successfully implemented in flexible, polymer-fullerene bulk-heterojunction solar cells.[1] Using vacuum deposition on cellulosic or porous alumina filters, films of randomly oriented CNT have been fabricated with an rms roughness of 7nm, a tendency to prohibit charge recombination, and a 2.5% power conversion efficiency[1] – close to that of an ITO based solar cell.

In this study, fabrication of CNT films employed soft lithography techniques – with polydimethylsiloxane (PDMS) stamps – so that patterned grids could be printed.

By orienting the CNTs into grids, this research was directed towards testing whether current would be conducted more efficiently along the major CNT axes. If this improvement was observed, then it is likely that the alignment of nanotubes enhances the coherence of electronic pathways – perhaps by decreasing the energy barriers electrons perceive at the 'dead-ends' of a randomly oriented network.

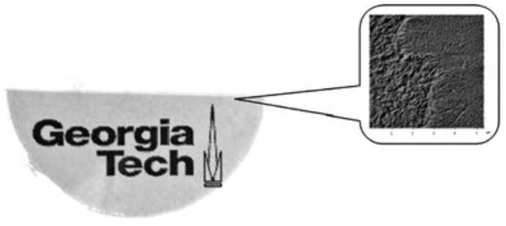

FIGURE 4. Demonstration of the transparency of a CNT film on plastic. The AFM image of the films edge confirms that the CNT network is random (film developed by Roderick Jackson of the Georgia Institute of Technology — STC MDITR)

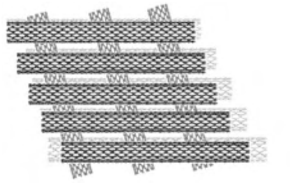

FIGURE 5. Idealized representation of the project goal of obtaining grid-patterned carbon nanotubes

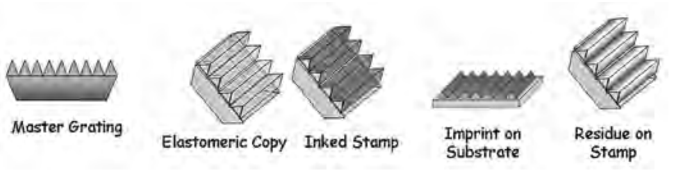

FIGURE 6. The soft lithography approach

Carbon Nanotube Electrodes

Use of carbon (graphite crystals) in electrodes is common; however, graphite crystals would be inappropriate for TC layers because conductivity can only be accomplished when the graphite crystals are densely packed enough to [nearly] touch each other – making for thick and opaque electrodes. But electrons travel much further along a CNT, moving freely from one unhybridized p-orbital to another – along an endless delocalized ϖ bond. Although nanoscale materials tend to exhibit different properties than what is observed on the macroscale, it is likely that the resistances of graphite crystals and CNT are still directly proportional to their length, and inversely proportional to their cross-sectional area. Therefore, CNT electrodes can be significantly more transparent because their quasi one dimensional structure readily offers a low resistance pathway of coherent electronic states.

Dispersal and Printing of CNT 'Ink'

Toluene; 1,2-orthodichlorobenzene (ODCB); and dimethylformamide (DMF) and a surfactant solution (1mg/mL sodium dodecyl sulfate (SDS) in nanopure water – 1% SDS in nanopure) was used to solubilize the CNTs. Many different concentrations of each organic solvent were tested. These, and the 1mg/mL CNT in SDS went through similar dispersion processes – between 20 and 90 minutes in the ultra-sonicator, followed immediately by 5 minutes in the centrifuge at 9k rpm. Numerous methods for adhering the CNTs to the substrate were then tested; however, samples were initially inked with a spin cast technique (at 1200 rpm for 15 seconds) in order to roughly determine the quality of CNT dispersal and concentration of CNT in the solvent. Elastomeric stamps with grooved features were then used to transfer the ink onto glass, silicon and HOPG substrates.

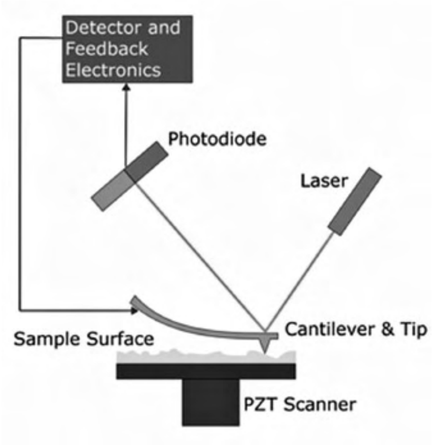

FIGURE 7. Schematic of the AFM instrument

A variety of methods were used to get the ink to transfer from the PDMS stamp to the substrate. Micro contact printing (μCP) and micro molding in capillary (MIMIC) were the two chief techniques employed. In both methods, PDMS was used to make a copy of the master grating and was inked with the CNT dispersion.

The μCP method required most of the solvent in the ink to evaporate, so that the stamp would leave an accurate imprint of its features when the stamp was gently forced against the surface, then retracted. Therefore, only organic solvents with a low boiling point were used with this method. The MIMIC technique was used with all solvents. The elastomeric stamp was placed on the substrate, and 1-5 μL were placed adjacent to the stamp. One minute was permitted for the ink to be pulled between the stamp and substrate by capillary forces, then 40g aluminum weights were placed on the stamps. The whole combination was then placed in an oven at 70˚C for 4 hours. Some SDS samples were submerged in nanopure for 30 seconds.

Surface Characterization — Atomic force Microscopy (AFM)

Surface features of the substrate were characterized using a non-optical imaging microscope.

In the *non-contact mode*, this instrument can gently probe a surface with a very sharp tip, by scanning just above the surface at a resonant frequency. Drive frequency is compared to tip frequency in order to detect the changes in dispersion forces between the moving tip and the surface features on the substrate. Integral to this design are adjustable operational amplifiers which raise and lower the tip over surface features for more accurate readouts. The difference between flat and patterned surfaces is demonstrated by images α, β and γ. (see following page)

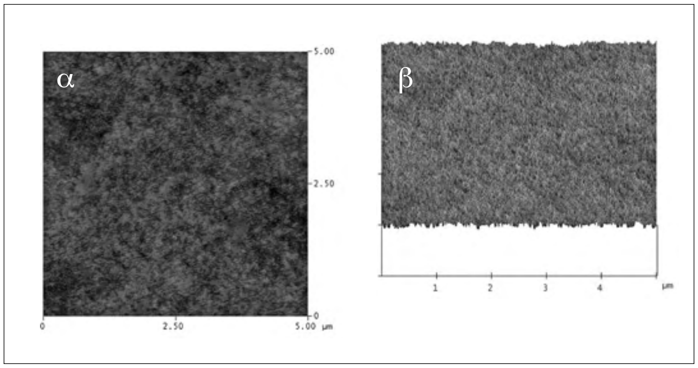

FIGURE 8. Image α and β: AFM images of glass cleaned with a standard sonication and plasma-O_2 process. Image α is a top-down view; image β is tilted to show roughness

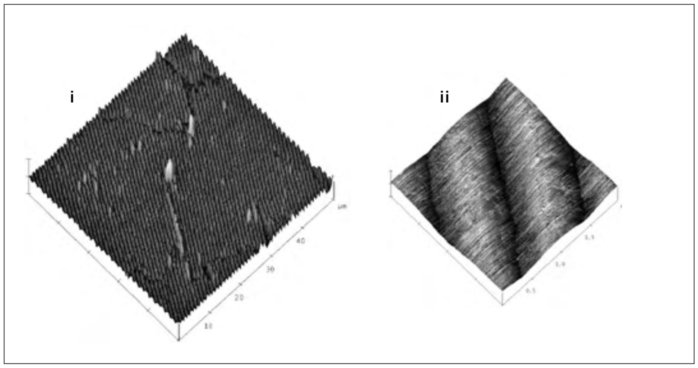

FIGURE 10. Image i and ii: 0.006 wt% CNT in ODCB

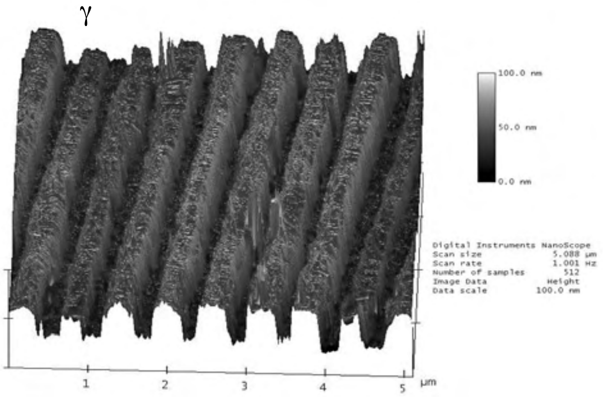

FIGURE 9. Image γ: AFM image of an 1800 gr/mm grating from 1g/mL CNT in SDS on a silicon wafer (MIMIC method)

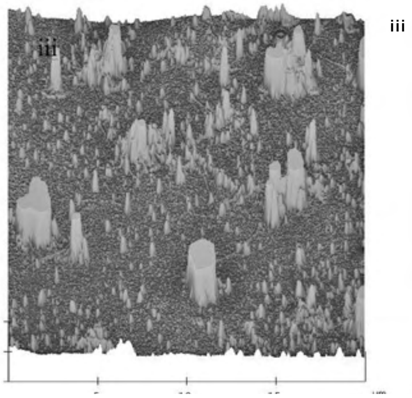

FIGURE 11. Image iii: 0.1 wt% CNT in toluene

AFM Surface Data

AFM surface images were taken for each different combination of solvent and stamping method. From the organic solvent dispersions, only the imprints made using MIMIC with 0.006 wt% CNT in ortho-dichlorobenzene yielded smooth enough features to gather AFM data (see image i, and ii below). Surface features on CNT in toluene samples were too difficult to characterize with the AFM (see image iii below).

AFM images of MIMIC imprints from the CNTs dispersed in SDS were consistently clear, although clumps can still be seen (images β, A and B).

Conclusion

Although this research was unable to establish a clear process for obtaining *conductive* grids of carbon nanotubes, surface images reveal that imprints of the stamp patterns were successfully transferred using the MIMIC technique. The AFM data provided evidence that the grid-patterned structures have dimensions that are on a similar scale to that of the carbon nanotube lengths (ie. an 1800 gr/mm stamp can print an array of 500 nm wide rows, which are about 20nm high) – and therefore must contain a dense array of CNTs. Unfortunately, no clear images were obtained of the CNT in the gratings, and rinsing techniques were unsuccessful.

The µCP method was not successfully employed to transfer the CNT ink from the PDMS to the substrate. Instead, AFM images revealed that either zero transfer occurred, or that randomly spaced clumps interfered with the AFM imaging. In many cases, insufficient adhesion to the substrate seemed to be the major shortcoming (even with MIMIC); perhaps strong intermolecular forces between CNT's caused clumping as the solvent evaporated. This seemed to be the most evident when using toluene, which was nearly impossible to obtain images for – the AFM tip would often be contaminated by material from the substrate surface that was in such large clumps that the tip couldn't pass over without colliding.

Future efforts should be directed towards the following:

- Obtain pure metallic, single wall CNTs
- Develop a better ink or dispersing agent; otherwise, improve rinsing technique
- Groove patterns smaller than nanotubes are long

200nm long nanotubes are more likely to align within the 100nm pattern of a 40 gr/µm grating

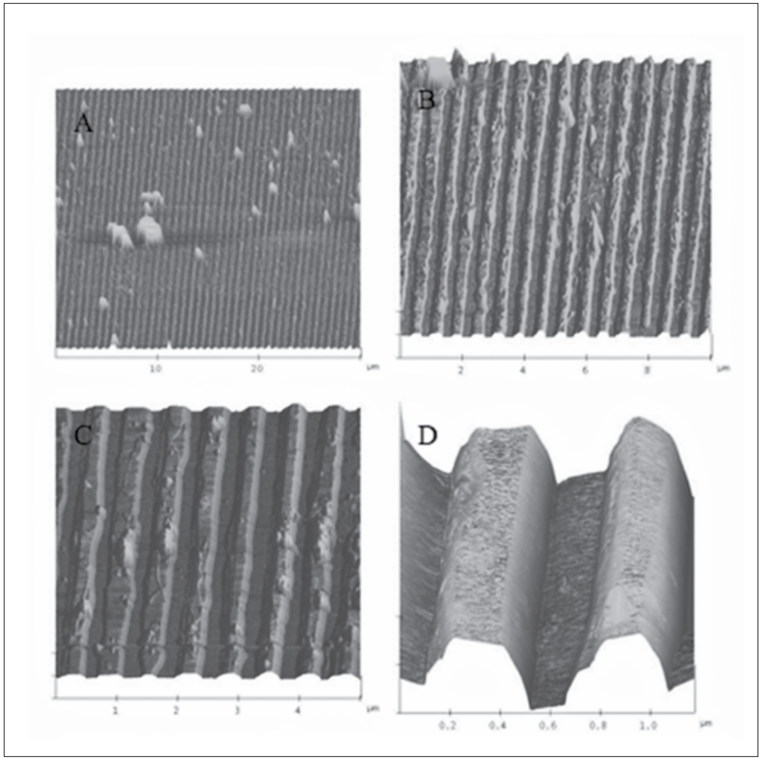

FIGURE 12. Images A, B, C & D: AFM image of 1800 gr/mm gratings – no DI rinse – from 1 g/mL CNT in SDS on glass (MIMIC method)

Acknowledgements

This work was made possible by the NSF sponsored Science & Technology Center on Materials and Devices for Information Technology Research, No. DMR-0120967; and the Department of Chemistry at the University of Arizona, Tucson

References

1. Jao van de Lagemaat – Organic Solar Cells with Carbon Nanotubes Replacing In_2O_3:Sn as the Transparent Electrode, Applied Physics and Letters 88, 233503 (2006)
2. Dimitrios Tasis – Chemistry of Carbon Nanotubes, Chem. Rev. 2006, 106, 1105-1136
3. G.M. Whitesides: Soft Lithography, Annual Review of Materials Science 28: 153-184 1998
4. MRS Bulletin – Scanning Probe Microscopy in Materials Science, July 2004
5. G. Gruner – Carbon Nanotube Films for Transparent and Plastic Electronics, Journal of Materials Chemistry, 16: 3533 (2006)

Novel Poly(aniline) Films

as Electroactive Supports for Artificial Photosynthesis in a Planar Membrane

JENNIFER FAUST, Illinois Wesleyan University
Kristina Orosz, Zeynep Ozkan, S. Scott Saavedra, The University of Arizona

Abstract

In order to develop a solar-powered energy conversion device that mimics photosynthesis, stable architectures are sought for planar-supported lipid bilayers across which a proton gradient can be generated. Specific investigations are focusing on two areas: the polymer interface and the substrate electrode.

In Part I, the polymer interface studied consisted of alternating layers of poly(aniline) (PANI) and poly(acrylic acid) (PAA). When taking multiple cyclic voltammograms (CVs) of $(PANI/PAA)_2$ on an indium-tin oxide (ITO) electrode, the current decreased with each potential cycle, suggesting instabilities in these self-assembled polyion films. In response to this phenomenon, the effects of potential cycling on the structural and electrochemical properties of the $(PANI/PAA)_2$ thin film were investigated.

In Part II, the ITO electrode was replaced with an alkanethiol-modified gold electrode to seek a more stable base for the polymer layers and the lipid bilayer.

Results indicated that after potential cycling, $(PANI/PAA)_2$/ITO became more hydrophilic, but the pH response and roughness surprisingly remained similar. In comparison to ITO, the modified gold electrode provided a smoother and more stable support for the polymer interface. Moreover, $(PANI/PAA)_2$ films on modified gold electrodes and on ITO showed a comparable pH response. This is a unique finding, in as much as gold electrodes, without modifying layers, do not respond potentiometrically to solution pH changes.

Introduction

In the natural world, plants and other organisms convert solar energy into chemical energy through the process of photosynthesis. Our team is working to produce a solar-powered energy conversion device that mimics photosynthesis in purple bacteria. Moore, Gust, and Moore have already created C-P-Q triads (carotenoid-porphyrin-quinone) that function as artificial photosynthetic reaction centers.[1] By inserting C-P-Q; benzoquinone (BQ), which is a redox-driven "proton shuttle;" and F_0F_1-ATP synthase into the membrane of a liposome, Moore, Gust, and Moore have been able to generate a transmembrane proton gradient and even synthesize ATP.[2]

Work is underway to extend these advances to a planar device that will transduce light energy into a proton gradient across an artificial biomembrane, complete with C-P-Q and BQ, which will be coupled to an electrode. A pH-sensitive, electrochemically active interface is necessary to bridge the electrode and lipid bilayer. The current approach involves layer-by-layer (LbL) self-assembly of alternating PANI and PAA layers on an ITO electrode. This ultrathin polymer film is of the form $(PANI/PAA)_2$, as diagrammed in Figure 1a.

PANI was specifically selected for the device because it is both electrochemically and spectroscopically active. Moreover, the redox equilibria among the main forms of PANI, shown in Figure 1b, are pH-dependent. Normally PANI only functions as a pH sensor in the acidic range, but by doping PANI with a poly(anion) such as PAA, the film's electroactivity shifts to the neutral range.[3] Additionally, PAA increases the hydrophilic character of the thin film to make it more compatible with a lipid bilayer.

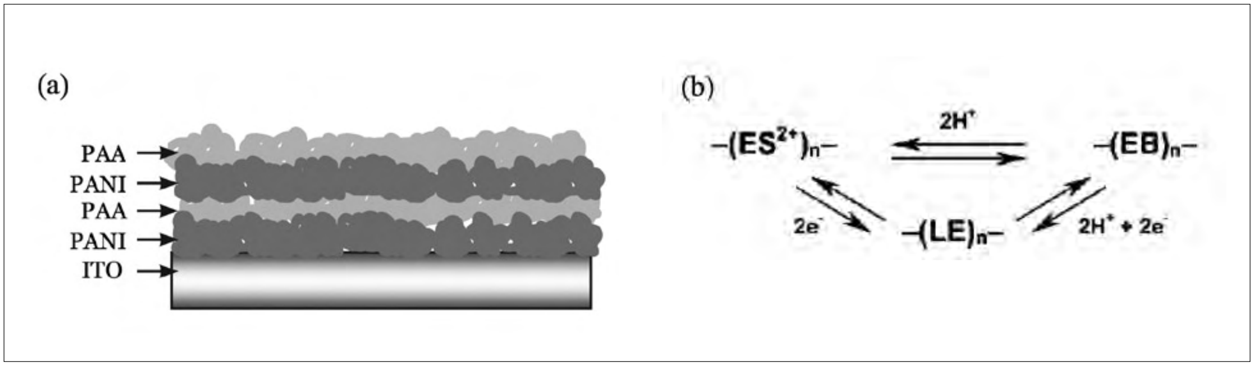

FIGURE 1. (a) The current structure includes a thin film composed of alternating PANI and PAA layers on an ITO electrode. This architecture is used to support a planar membrane across which a proton gradient will be generated. (b) The emeraldine salt (ES) and emeraldine base (EB) are both partially oxidized forms of PANI, and leucoemeraldine (LE) is the fully reduced form. Equilibria among these forms are pH-dependent.

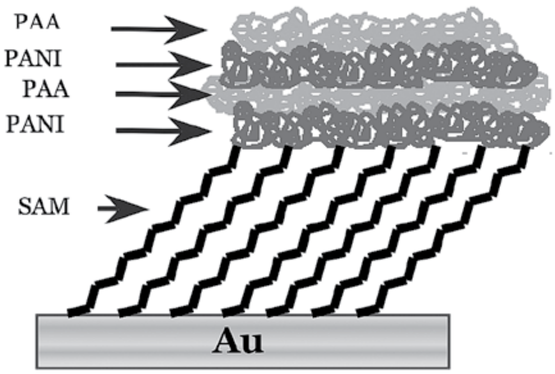

FIGURE 2. (PANI/PAA)2 bilayers were deposited on a gold electrode that had been modified with a self-assembled monolayer (SAM) of 11-mercaptoundecanoic acid.

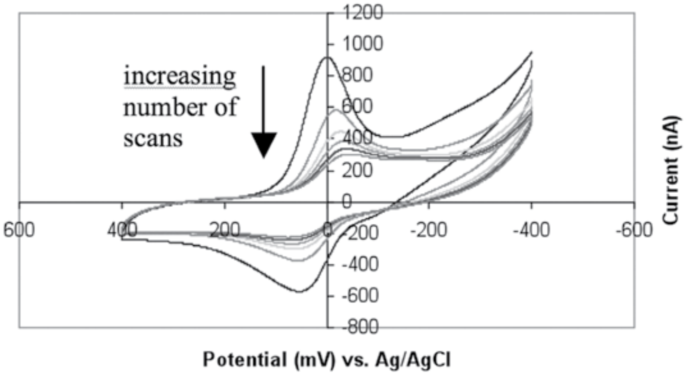

FIGURE 3. CVs taken for potential cycles 1, 5, 10, 15, 20, and 25 of (PANI/PAA)2/ITO in 0.1 M phosphate buffer at pH 7. The potential was scanned vs. Ag/AgCl. at a rate of 10 mV/sec.

The stability of the $(PANI/PAA)_2$/ITO architecture has proven to be marginal. The film is electrochemically unstable, and the rough surface of the ITO electrode is believed to make the deposition of a functional lipid bilayer less likely. To seek a more stable film structure that remains responsive to pH, the following two areas were investigated: (I) the change in $(PANI/PAA)_2$ structure and pH response after potential cycling; (II) the use of modified gold instead of ITO as the electrode, as shown in Figure 2.

Experimental Methods

PANI, emeraldine base form, M_v 10,000; 1-methyl-2-pyrrolidinone (NMP), anhydrous, 99.5%; PAA, M_v 2000; and 11-mercaptoundecanoic acid (11-MUA), 99.5% were purchased from Aldrich and used without further purification. PANI was dissolved in NMP, PAA was dissolved in deionized (DI) water (18 MΩ/cm), and 11-MUA was dissolved in absolute ethanol.

ITO was obtained from Delta Technologies, Limited and had been coated on SiO_2 passivated, unpolished float glass with a resistance of 8-12 Ω/cm^2 and a thickness of 0.7 mm. The cleaning procedure for ITO has been described elsewhere.[4]

Gold substrates were obtained from EMF Corporation and were coated on glass slides to a thickness of 1000 Å. The electrodes were cleaned by immersion in Piranha, a 3:1 mixture of concentrated sulfuric acid and 30% hydrogen peroxide, for 15 minutes. After removal from the Piranha solution, the electrodes were rinsed first with DI water and then with ethanol before drying under a N_2 stream. Cleaned gold electrodes were then modified with a self-assembled monolayer (SAM) by immersion in a 5 mM solution of 11-MUA in ethanol for at least 24 hours. Previous studies have indicated that this length of time is sufficient for deposition.[5]

PANI and PAA were deposited on cleaned ITO and on SAM-modified gold electrodes by the LbL self-assembly method. PANI and PAA solutions were 1 mg/mL and 15 mg/mL, respectively. Further details have been described elsewhere.[4]

To characterize the properties of the thin films, CVs were taken on an EG&G potentiostat (Princeton Applied Research, model 263A) in a standard three-electrode cell. The working electrode was either polymer-coated ITO or gold, the counterelectrode was Pt, and the reference electrode was Ag/AgCl (3 M NaCl). The area of the working electrode in contact with solution was 0.28 cm^2. Another electrochemical cell with an area of 0.64 cm^2 was also used in order to prepare larger samples for analysis by contact angle and atomic force microscopy (AFM).

Contact angles were measured on a Krüss DSA 10 Mk2 using a drop size of 0.5 μL of DI water. Ellipsometry was performed at a wavelength of 633 nm with a reflection angle of 70° (Sentech SE400). All AFM images were generated in tapping mode (Digital Instruments Dimension 3100). Purchased from MikroMasch, the tips had an average resonance frequency of 325 kHz and an average force constant of 40 N/m. The pH response of the films was monitored potentiometrically by injecting solutions of 0.1 M universal buffer (phosphate, borate, acetate), pH 3-9, and allowing the potential to equilibrate. Measurements were taken on a high-impedance pH meter (Denver Instruments, model 215).

Cycle Number	1	5	25
Electroactive Surface Coverage (nmol/cm^2)	1.3	0.94	0.70

TABLE 1. Electroactive Surface Coverage of (PANI/PAA)2/ITO

Cycle	0*	1†	5‡	10†	25‡
Response	-37	-44	-37	-38	-42
(mV/pH)	±5		±1		±5

TABLE 2. pH Response of (PANI/PAA)2/ITO

* Measurement is an average of three trials.

† Only one trial was completed.

‡ Measurements are an average of two trials.

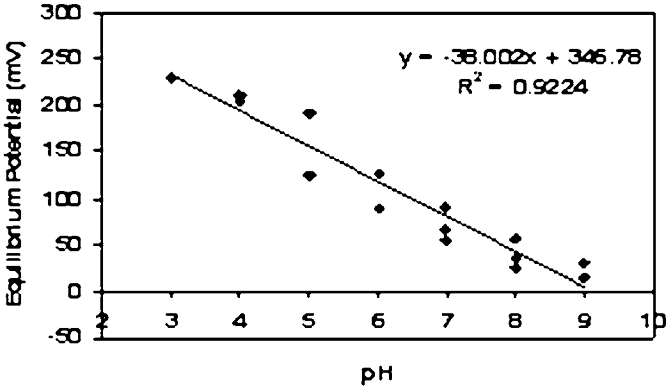

FIGURE 4. pH response graph of (PANI/PAA)2/ITO after 25 cycles. In this particular trial, the slope was -38 mV/pH with a correlation coefficient of 0.9224.

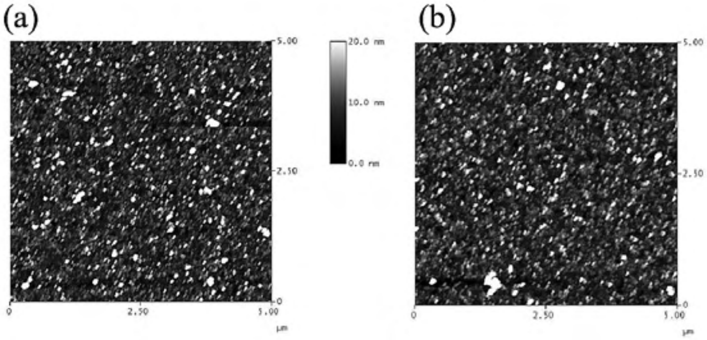

FIGURE 5. AFM images of (PANI/PAA)2 on ITO (a) after 0 cycles and (b) after 25 cycles. Images are 5 x 5 microns taken at a scan rate of 1 Hz. The average rms roughness of the samples was (a) 2.9 nm, ± 0.3 nm and (b) 3.4 nm, ± 0.5 nm

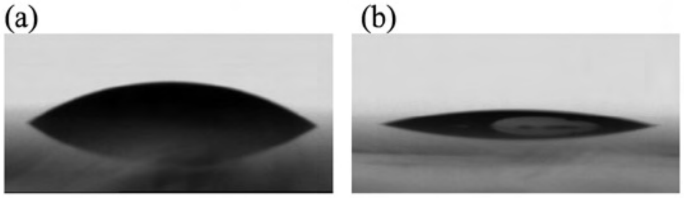

FIGURE 6. The contact angle of DI water on (PANI/PAA)2/ITO was **(a)** 33° ± 3° after 0 cycles and **(b)** 15° ± 2° after 25 cycles.

Results and Discussion

I. Effects of Potential Cycling on $(PANI/PAA)_2$/ITO

As shown in the CVs in Figure 3, the current declined during progressive cycling of $(PANI/PAA)_2$/ITO. Unless specified otherwise, all CVs were taken in 0.1 M phosphate buffer (pH 7) vs. Ag/AgCl. The scan rate was 10 mV/sec, and the potential window was -400 mV to 400 mV. Table 1 reveals that a loss of electroactivity accompanied the change in current. After applying one cycle to $(PANI/PAA)_2$/ITO, the electroactive surface coverage was 1.3 nmol/cm^2, but after 25 cycles, the surface coverage decreased to 0.70 nmol/cm^2. Concomitant changes in the film's properties were studied to evaluate how potential cycling will affect the deposition of a stable, functional lipid bilayer.

Surprisingly, potentiometric experiments revealed that the pH response of $(PANI/PAA)_2$/ITO remained similar before and after cycling. Measurements are summarized in Table 2. Figure 4 presents the plot of one of the response trials. Before cycling, the film's potential changed -37 mV (± 5 mV) per pH unit. In turn, the pH response was -44 mV/pH after one cycle and -37 mV/pH (± 1 mV/pH) after five cycles. Finally, after 25 cycles, the film had a pH response of -42 mV/pH (± 5 mV/pH). Because the values showed no clear trend and remained in the neighborhood of -40 mV/pH, it was concluded that potential cycling did not reduce the film's viability as a pH sensor.

In addition to electrochemical properties, the morphological properties of $(PANI/PAA)_2$/ITO were also compared before and after cycling. Based on AFM, the average root mean square (rms) roughness of the films did not change as a result of cycling (see Figure 5). Initially, the roughness was 2.9 nm (± 0.3 nm). It did increase slightly to 3.4 (± 0.5 nm) after 25 cycles, but this increase remained within the limits of the standard deviation. Cycling did not appear to change the surface topography of the film.

Although cycling essentially did not alter the pH response or roughness of the film, its wettability did in fact increase, as shown in Figure 6. Uncycled $(PANI/PAA)_2$/ITO was moderately hydrophilic: a 0.5 μL drop of DI water spread to an angle of 33° (± 3°). After 25 cycles, in contrast, the film had a contact angle of 15° (± 2°). The decrease in contact angle with cycling showed a steady trend: after 1 cycle, the contact angle was 25° (± 0°), and after 5 cycles, the contact angle was 21° (± 1°). Based on this data, it is possible that potential cycling caused PANI to desorb from the film because the contact angle approached that of bare ITO (less than 5°). However, it is more likely that cycling resulted in a restructuring of the film, causing PANI to migrate toward ITO and PAA to move toward the surface. As a result, cycling may actually make $(PANI/PAA)_2$/ITO more compatible with a lipid bilayer by increasing the hydrophilic character of the film.

II. PANI Films on Modified Gold Electrodes

Although McBee et al. have successfully deposited planar supported lipid bilayers on (PANI/PAA)$_2$/ITO,[6] the surface chemistry of ITO nevertheless renders it less than ideal as an electrode. Not only is ITO relatively rough (average rms roughness = 1.8 nm ± 0.07 nm), but it also is non-uniform as a conductor.[7] In comparison to ITO, gold is both a smoother substrate and a better electrode. However, PANI will not adsorb directly to gold, so the electrode must be modified with a SAM.

The Knoll group has extensively characterized the properties of PANI films on gold electrodes modified with 3-mercapto-1-propanesulfonic acid (MPS),[3] but in this study, 11-MUA was selected for the monolayer. Contact angle measurements, summarized in Table 3, confirmed that 11-MUA successfully adsorbed to the gold electrode. With a contact angle of 72° (± 3°), bare gold was initially hydrophobic, but after deposition of the SAM, the contact angle was 30° (± 3°). Indeed, carboxy-terminated SAMs like 11-MUA are frequently used to increase surface wettability.[8] From ellipsometry, the thickness of the SAM layer was measured as 1.1 nm (± 0.2 nm).

Contact angle measurements also showed that PANI adsorbed to the SAM-modified gold electrode: after LbL self-assembly of a PANI monolayer, the contact angle was 51° (± 2°). After deposition of two PANI/PAA bilayers on SAM-modified gold, the contact angle decreased to 35° (± 1°), which was comparable to the contact angle of (PANI/PAA)$_2$ on ITO.

Unlike ITO, SAM-modified gold is relatively smooth, as evidenced by AFM. The rms roughness of bare gold after cleaning was 1.07 nm (± 0.03 nm). The roughness of SAM-modified gold, calculated as 1.07 nm (± 0.05 nm), was essentially the same. The rms roughness of bare ITO after cleaning, on the other hand, averaged 1.80 nm (± 0.07 nm). Thus, the roughness decreased by about 40% from ITO to gold. This difference is visible in the AFM images shown in Figure 7. In addition, (PANI/PAA)$_2$/SAM/Au was also slightly smoother than (PANI/PAA)$_2$/ITO: the rms roughness of the bilayers on gold was 1.8 nm (± 0.5 nm) compared to 2.9 nm (± 0.3 nm) on ITO.

Cyclic voltammetry enabled the electrochemical properties of PANI films on SAM-modified gold to be characterized. As shown in Figure 8a, SAM-modified gold electrodes showed no peaks within the -400 mV to 400 mV potential range. This agrees with data that Clark and Bowden have previously collected for 11-MUA on gold.[9] Once PANI adsorbed to the SAM-modified gold electrode, anodic and cathodic peaks confirmed electrochemical activity. Therefore, it follows that the chain length of 11-MUA is not too long to prevent electron tunneling between PANI and the gold substrate.

	Au	SAM/ Au	PANI/ SAM/Au	(PANI/PAA)$_2$/ SAM/Au
Contact Angle	72° ±3°	30° ±3°	51° ±2°	35° ±1°

TABLE 3. Contact Angle Measurements

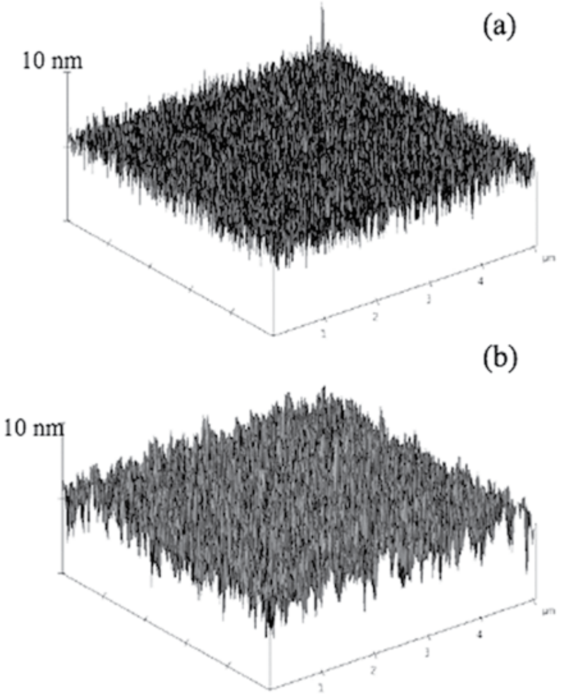

FIGURE 7. AFM surface plots of **(a)** SAM-modified gold and **(b)** bare ITO.

To better compare the electrochemical stability of SAM-modified gold with ITO, (PANI/PAA)$_2$ bilayers were cycled on modified gold electrodes. CVs for both SAM/Au and PANI/SAM/Au were taken in 4.4 mM phosphate buffer (10 mM ionic strength) at pH 7. The potential was scanned vs. Ag/AgCl at a rate of 50 mV/sec over a potential window of -400 mV to 400 mV. In contrast, CVs of (PANI/PAA)$_2$/SAM/Au were taken in 0.1 M phosphate buffer at a scan rate of 10 mV/sec to match the parameters for (PANI/PAA)$_2$/ITO.

Unlike (PANI/PAA)$_2$ on ITO, the bilayers on SAM-modified gold showed no appreciable decrease in current with cycling (see Figure 8b). This difference was attributed to stronger intermolecular interactions between PANI and 11-MUA than between PANI and the surface moieties of ITO. Figure 9 depicts possible electrostatic forces between positively charged forms of PANI and deprotonated carboxy groups on 11-MUA as well as possible hydrogen bonding between PANI and the carboxy groups on 11-MUA.

Based on previous studies, it is not surprising that current declines on ITO electrodes but not on SAM-modified gold electrodes. For instance, Bartlett and Simon reported a decline in current with potential cycling for PANI films on glassy carbon electrodes.[10] On the other hand, Tian et al. found no decrease in the current of PANI films deposited on gold electrodes modified with MPS, a three-carbon alkanethiol.[11] The results of this study on 11-MUA further reinforce the trend that carboxy-terminated alkanethiols maintain the electrochemical stability of the overall film structure.

Electroactive surface coverage values both verified this stability and confirmed that SAM-modified gold electrodes were more electrochemically active than ITO electrodes. After 5 cycles of (PANI/

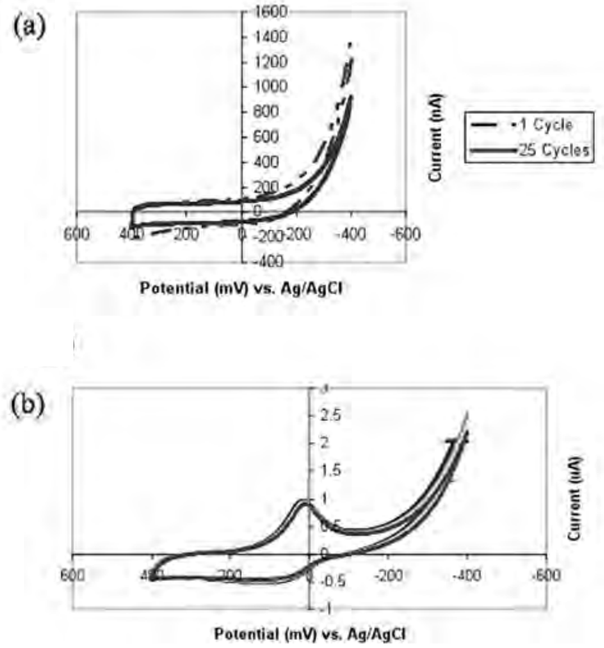

FIGURE 8. **(a)** Cycles 1 and 25 of SAM-modified gold in 4.4 mM phosphate buffer (pH 7) at a scan rate of 50 mV/sec. **(b)** Cycles 5, 10, 15, 20, and 25 of (PANI/PAA)2/SAM/Au in 0.1 M phosphate buffer (pH 7) at a scan rate of 10 mV/sec.

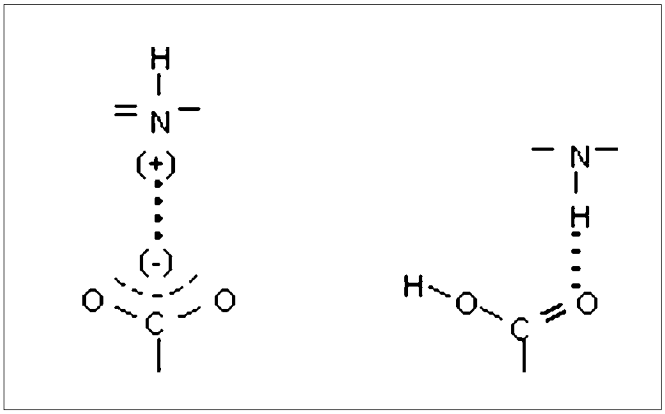

FIGURE 9. Two proposed interactions between 11-MUA and PANI

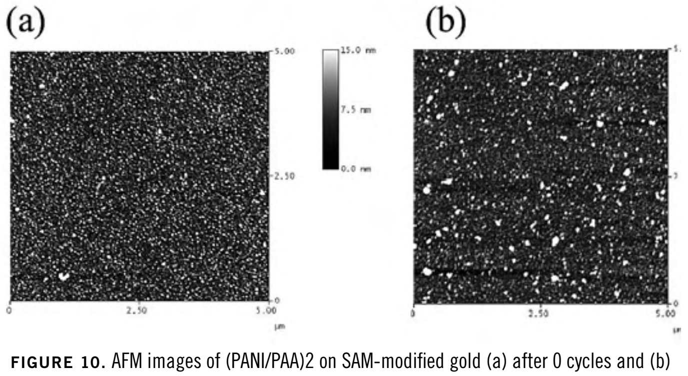

FIGURE 10. AFM images of (PANI/PAA)2 on SAM-modified gold (a) after 0 cycles and (b) after 25 cycles. Images are 5 x 5 microns taken at a scan rate of 1 Hz. The average rms roughness of the samples was (a) 1.8 nm, ± 0.5 nm and (b) 2.4 nm, ± 0.3 nm.

PAA)$_2$/SAM/Au, the electroactive surface coverage was 1.4 nmol/cm^2, and after 25 cycles the value decreased by about 6% to 1.3 nmol/cm^2. On ITO, in contrast, the electroactive surface coverage decreased by over 25% from 5 cycles to 25 cycles. In addition, the electroactive surface coverage was consistently greater on SAM-modified gold than on ITO (see Table 1 for comparison). These results make sense because gold is a better conductor than ITO, which has patchy regions of electrochemical conductivity.[7]

Despite differences in the electrochemical stability, uncycled (PANI/PAA)$_2$ exhibited a comparable pH response on modified gold electrodes as on ITO: the film had a pH response of -39 mV/pH (± 1 mV/pH) on SAM-modified gold vs. -37 mV/pH (± 5 mV/pH) on ITO. As a result, (PANI/PAA)$_2$/SAM/Au holds potential applications as a pH sensor.

To further compare (PANI/PAA)$_2$ on SAM-modified gold to (PANI/PAA)$_2$ on ITO, the effect of potential cycling on the pH response of (PANI/PAA)$_2$/SAM/Au was analyzed. As on ITO, films on modified gold electrodes showed no change: after 25 cycles of (PANI/PAA)$_2$/SAM/Au, the pH response remained -39 mV/pH. However, individual pH response measurements for the films on Au, which were within a 2 mV/pH range, did not vary as much as on ITO, where the range was 15 mV/pH. This observation was consistent with the general trend that films were more stable on SAM-modified gold than on ITO.

Analysis of AFM images of (PANI/PAA)$_2$/SAM/Au (see Figure 10) did not show a statistically significant difference in roughness. Following 25 cycles of (PANI/PAA)$_2$/SAM/Au, the average rms roughness had risen from 1.8 nm (± 0.5 nm) to 2.4 nm (± 0.3 nm). Nevertheless, films on gold electrodes remained smoother than on ITO even after 25 cycles (see Figure 5b for comparison).

Interestingly, cycling actually made (PANI/PAA)$_2$/SAM/Au slightly more hydrophobic, whereas the film became more hydrophilic on ITO. The film's contact angle on SAM-modified gold, which was 35° (± 1°) before cycling, increased to 39° (± 1°) after 25 cycles. Such a change is of minimal significance, especially in comparison to the 18° decrease in contact angle observed on ITO. Indeed, the fact that the contact angle did not change nearly as much on gold as on ITO was consistent with the film's added stability on modified gold electrodes.

Conclusion

Preliminary results indicated that potential cycling had no statistically significant effect on the pH response or roughness of (PANI/PAA)$_2$ ultrathin films on ITO. However, because the films became more hydrophilic, potential cycling may actually establish a more favorable environment for the adsorption of a lipid bilayer. Future work will focus on depositing phosphatidylcholine lipids onto (PANI/PAA)$_2$/ITO after cycling.

Results also revealed that while (PANI/PAA)$_2$ films on ITO and on modified gold electrodes displayed similar sensitivities as pH sensors, the 11-MUA monolayer offered a smoother, more electrochemically stable support for the deposition of a (PANI/PAA)$_2$ polymer cushion. Accordingly, a stable lipid bilayer is expected to be more compatible with polymer-coated modified gold electrodes than with ITO.

Acknowledgments

This material is based upon work supported by the STC Program of the National Science Foundation No. DMR 0120967, and CHE 0453596. The following individuals also deserve special recognition: Dr. Neal R. Armstrong and Dr. Dennis H. Evans for their electrochemical insights; Yimin Hua, Karen Bryden-Joyce, Mariola Macech, and James Joubert for instrument training; and all the members of the Saavedra group for their support and advice.

References

1. Steinberg-Yfrach, G.; Liddell, P. A.; Hung, S. C.; Moore, A. L.; Gust, D.; Moore, T. A.; *Nature* 1997, 385, 239-241.
2. Steinberg-Yfrach, G.; Rigaud, J.; Durantini, E. N.; Moore, A. L.; Gust, D.; Moore, T. A.; *Nature* 1998, 392, 479-482.
3. Tian, S.; Baba, A.; Liu, J.; Wang, Z.; Knoll, W.; Park, M.; Advincula, R.; *Adv. Func. Mater.* 2003, 13, 473-479.
4. Ge, C.; Armstrong, N. R.; Saavedra, S. S.; *Anal. Chem.* 2007, 79, 1401-1410.
5. Boldt, F.; Baltes, N.; Borgwarth, K.; Heinze, J.; *Surf. Sci.* 2003, 597, 51-64.
6. McBee, T. W.; Wang, L.; Ge, C.; Beam, B. M.; Moore, A. L.; Gust, D.; Moore, T. A.; Armstrong, N. R.; Saavedra, S. S.; *J. Am. Chem. Soc.* 2006, 128, 2184-2185.
7. Armstrong, N. R.; Carter, C.; Donley, C.; Simmonds, A.; Lee, P.; Brumbach, M.; Kippelen, B.; Domercq, B.; Yoo, S.; *Thin Solid Films* 2003, 445, 342-352.
8. Deval, J; Umali, T. A.; Spencer, B. L.; Lan, E. H.; Dunn, B.; Ho, C; *Mat. Res. Soc. Symp. Proc.* 2003, 774, 05.8.1-05.8.6.
9. Clark, R. A.; Bowden, E. F.; *Langmuir* 1997, 13, 559-565.
10. Bartlett, P. N.; Simon, E; *Phys. Chem. Chem. Phys.,* 2000, 2, 2599-2606.
11. Tian, S.; Liu, J.; Zhu, T.; Knoll, W.; *Chem. Mater.,* 2004, 16, 4103-4108.

JENNIFER FAUST is currently working toward a B.S. in chemistry at Illinois Wesleyan University and plans to pursue either a master's degree in chemical engineering or a Ph.D. in chemistry.

Fabrication and Temperature Dependence of Fiber Bragg Gratings

IZA FERREIRA, College of Optical Sciences, The University of Arizona
Dr. Nasser Peyghambarian, Dr. Axel Schülzgen, Shigeru Suzuki, College of Optical Sciences, The University of Arizona

Introduction

Fiber Bragg gratings are structures inside optical fibers that have the property of reflecting a specific wavelength and transmitting the rest of the incoming spectrum. In other words, these gratings work as a mirror for a specific wavelength, but not for the rest of the spectrum. The reflected wavelength is called the Bragg wavelength. The Bragg wavelength of a certain fiber Bragg grating is dependent on the index of refraction of the optical fiber (n_{eff}) and the period of the grating (Λ). The formula for the Bragg wavelength is shown below.

$$\lambda_B = 2n_{eff}\Lambda \quad (1)$$

Tuning of the Bragg wavelength can be done using temperature. The Bragg wavelength is dependent on temperature because a change in temperature effectively modifies both the index of refraction of the fiber and the period of the grating. The variation in index of refraction with temperature is determined by the thermo-optic coefficient. For silica glass this coefficient is around $7*10^{-6}$/°C.[2] The change in temperature also makes the optical fiber expand or contract, according to the coefficient of thermal expansion. For silica glass, the coefficient of thermal expansion is around $5*10^{-7}$/°C. [1]

A change in Bragg wavelength with temperature can be a desired characteristic for certain devices: For a temperature sensor it is desired to have a change in a physical property of the device that represents a change in temperature. In the case of a fiber laser, it is preferred that the characteristics of the fiber Bragg grating remain constant during the operation of the laser. For this type of application, the thermo-optic coefficient and the thermal-expansion coefficient can be combined in a way to reduce the temperature sensitivity of the grating.

Fiber Bragg gratings are possible because of a nonlinear effect called photosensitivity. This effect makes the index of refraction of photosensitive optical fibers change when they are exposed to light. It has been demonstrated that ultraviolet (UV) lasers are the most efficient light source for making fiber Bragg gratings.[2] Ordinary silica fibers are not photosensitive, but other types of fibers that are photosensitive are available. Currently, research is being done in many institutions to increase the photosensitivity of optical fibers. This usually involves doping optical fibers with rare-earth ions. At the College of Optical Sciences at the University of Arizona, research is being done to increase the photosensitivity of Germanium-doped phosphate fibers, in order to create fiber lasers consisting of only phosphate fibers.[3, 4]

This paper contains information about a research performed at the College of Optical Sciences complementary to the one mention above. The purpose of this research is to fabricate fiber Bragg gratings that can be used in the research for compact fiber lasers, and to measure the Bragg wavelengths of fiber Bragg gratings as a function of temperature. Three types of photosensitive optical fibers were utilized for the gratings:

- Newport F-SBG-15
- Nufern 980
- Nufern PSGDF

For each of theses optical fibers, two gratings were to be made, one with a reflectivity of 20% ± 5% and another with a reflectivity of 50% ± 5%. Additional fiber Bragg gratings were to be made for the temperature-dependence measurements.

Research Methods

There are a few possible methods for the fabrication of fiber Bragg gratings. The method utilized in this research is the most common and efficient method, currently. In general terms, this method is a UV exposure of an optical fiber through a phase mask. This method utilizes the fact that the claddings of optical fibers are transparent to UV radiation, however, their cores absorb this type of radiation. As a consequence, the fibers can be exposed transversely, without the need to remove their claddings. Figure 1 shows a schematic of the setup.

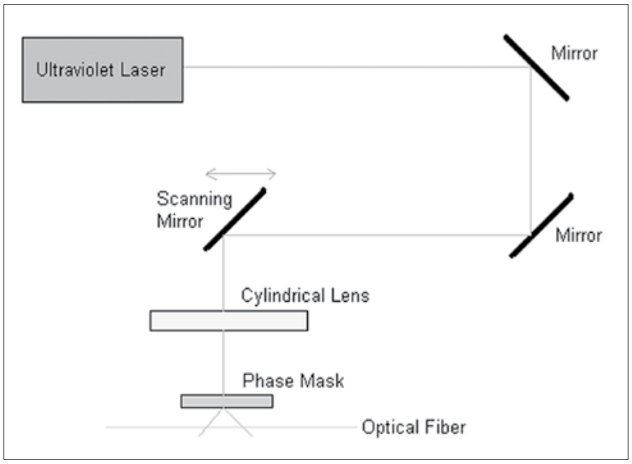

FIGURE 1. Schematic of setup to fabricate fiber Bragg gratings.

The components of the setup are explained next. The ultraviolet laser is an Argon laser source, with a wavelength of 488 nm, combined with a frequency-doubling crystal that makes the final wavelength be 244 nm. The mirrors are used to guide the laser beam. The scanning mirror has the purpose of guiding the laser beam so that it reaches the desired length of the optical fiber where the grating will be located. The cylindrical lens focuses the laser beam on the optical fiber. And finally, the phase mask diffracts the laser beam creating an interference pattern that makes the grating periodic. Figure 2 is a picture of the setup:

The reflectivity of the fiber Bragg gratings was measured as the gratings were made. The transmittance spectrum was used to determine the reflectivity of the gratings. The process was the following: the transmittance spectrum was set to a reference point, then as the reflectivity began to increase, the transmittance spectrum began to show a dip. This dip demonstrates that part of the spectrum is being reflected as the grating is formed. Since the only change in the fiber is the grating, it is a good assumption to say that the dip determines the reflectivity of the grating. This method eliminates the need to account for losses in the fiber, because the reference point already takes into account these losses. This is the reason why the transmittance spectrum is used, instead of the reflectance spectrum. Figure 3 shows a schematic of the method used to measure the transmittance spectrum.

The reflectance spectrum was also obtained. The bandwidth of the spectrum was determined using the reflectance spectrum. The temperature dependence test was performed using the reflectance spectrum as well. Figure 4 shows the schematic of the method used to measure the reflectance spectrum.

For the temperature dependence test, the Bragg wavelength was monitored as the temperature of the grating was varied. The grating was positioned inside a glass container sitting on top of a hot plate. A temperature probe was placed near the grating, and the Bragg wavelength was recorded from an optical spectrum analyzer. The range of temperatures used was 30 to 120 °C, at a step size of 10 °C. Figure 5 shows this setup.

FIGURE 2. Picture of the setup for the fabrication of fiber Bragg gratings.

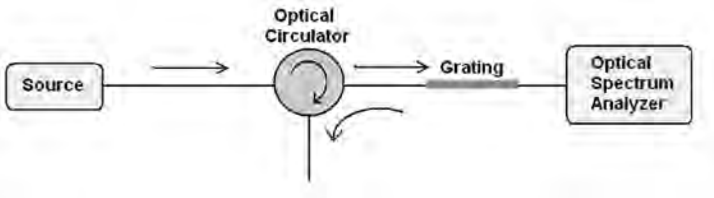

FIGURE 3. Schematic of process to measure transmittance spectrum.

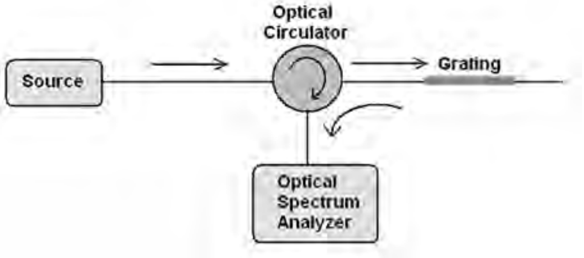

FIGURE 4. Schematic of process to measure reflectance spectrum.

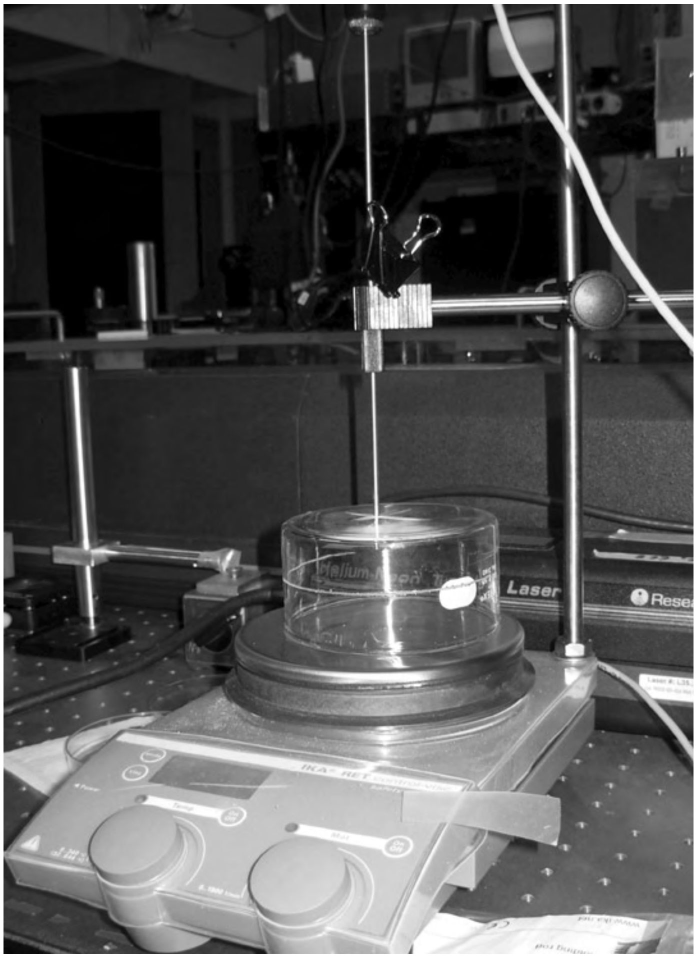

FIGURE 5. Picture of hot plate and probe used to control the temperature of fiber Bragg gratings.

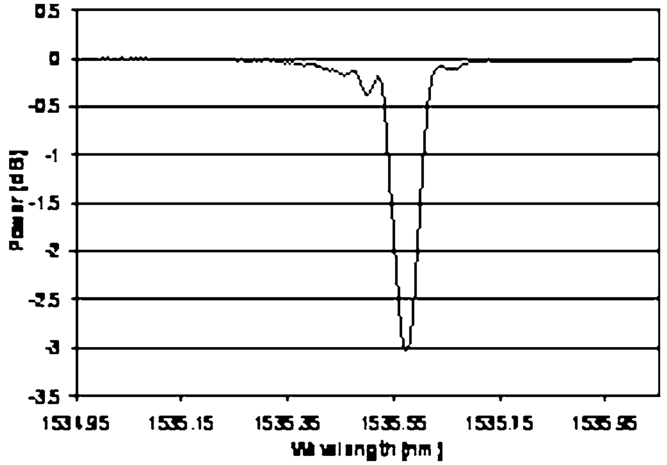

FIGURE 6. An example of a transmittance spectrum. This spectrum is from grating 12.

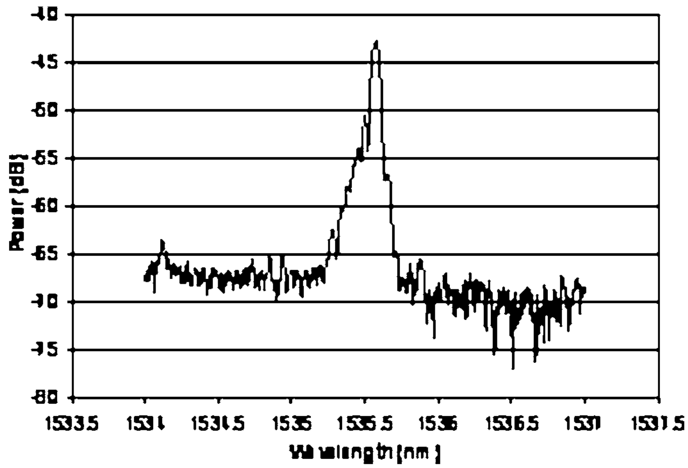

FIGURE 7. Example of a reflectance spectrum. This is the spectrum of grating 12.

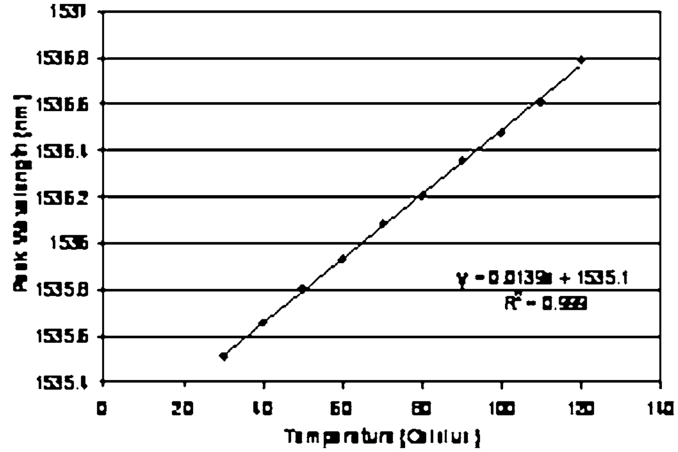

FIGURE 8. Plot showing temperature dependence of grating 12.

Data and Results

As the gratings were fabricated, their transmittance and reflectance spectra were obtained. Figure 6 is an example of a transmittance spectrum. The figure shows the reference level at zero, and the dip. In this example the dip reaches the minimum value of -3.015 dB, which means that 49.9% of the incoming light is transmitted through the fiber and 50.1 % of the light is reflected, at a wavelength of 1535.58 nm.

The reflectance spectrum was also obtained. One example of this graph is on figure 7. The power axis on this graph does not have any absolute meaning regarding the value of the reflectivity.

The table below shows a summary of the fiber Bragg gratings fabricated.

The exposure time and the power of the ultraviolet laser varied throughout the research. For this reason, the gratings were compared in terms of the total energy delivered to the fibers. Looking at the table, it is clear that some optical fibers are more photosensitive than others. Table 2 shows the total energy delivered per change in the transmittance in dB. This value represents the photosensitivity of each optical fiber. The transmittance is being used here instead of reflectance because the transmittance spectrum was the one used to measure the reflectivity.

The optical fiber with the most photosensitivity is the FSBG15, followed by the PSGDF and the 980. The value of energy per change in transmittance varies significantly among the same fiber type due to variations in the stability of the setup.

The temperature dependence test was performed using six fiber Bragg gratings. The Bragg wavelength was recorded for each of the temperature steps, and the result was plotted for each grating on a separate graph. A linear trendline was included on the plots to find the wavelength change as a function of temperature. The figure below is an example of one of these plots.

As the figure shows, an equation was found for the linear trendline, and this is how the temperature sensitivity was obtained. Table 3 shows the results obtained for all the gratings.

The optical fiber PSGF has a larger core diameter than the other two types. This characteristic may lead to a slight difference is temperature sensitivity. More samples need to be tested to determine if this is indeed the case. In this research no distinction was made between the different types of optical fibers.

Discussion

The main challenges encountered in the fabrication of fiber Bragg grating were related to the stability of the setup, the fluctuating power of the ultraviolet laser, and losses due to bad connections. The stability of the setup is crucial for the making strong gratings. The better the alignment of the setup, the more laser energy can be directed to the fiber, and therefore a stronger grating can be made. The efficiency of the setup was reduced when its components were not stable.

Grating Number	*Fiber Type*	*Exposure Time (min)*	*Total Energy Delivered (mJ)*	*Reflectivity (%)*
1	FSBG	3.33	1600	20.2
2	FSBG	2.00	1044	46.6
3	980	33.33	14700	18.5
4	PSGDF	13.33	4400	19.1
5	PSGDF	33.33	15600	21.2
6	PSGDF	46.67	20580	32.0
7	FSBG	0.67	324	21.9
8	FSBG	3.33	1680	49.3
9	FSBG	9.33	5600	97.0
10	980	46.67	24080	14.0
11	PSGDF	28.00	12936	14.6
12	FSBG	6.00	2124	50.1

TABLE 1. Summary of fiber Bragg gratings fabricated.

The Argon laser needs constant maintenance for its power to stay constant. Usually, the power of this laser constantly decreases, making it difficult to make strong gratings. The connections for the optical fiber need to be constantly checked and cleaned. Sometimes they create excessive losses and therefore need to be replaced with new connections.

The different optical fibers used in this research have different photosensitivities. The fiber type FSBG15 has the highest amount of photosensitivity. A possible improvement to the temperature test performed here would be to only consider one type of fiber at a time. Different types of fibers have different thermo-optic coefficients and thermal-expansion coefficients, therefore have different temperature sensitivities. For a more accurate result to be achieved, more samples should be tested. It is suggested that at least 50 samples be tested.

Another improvement would be to develop a better setup for the temperature test. Ideally, the entire grating chain should be in an enclosed and stable compartment.

The result presented here for the temperature sensitivity is slightly higher than published results for the temperature sensitivity of silica fibers. Theoretically, silica fibers have a temperature sensitivity of approximately 13.7 pm/°C.[5]

	FSBG15	*980*	*PSGDF*
	1,629.30	17,033.60	3,426.80
	382.70	27,332.60	15,043.40
	301.70		12,286.60
	570.10		16,437.10
	368.60		
	704.50		
Average	**659.48**	**22,183.10**	**11,798.48**

TABLE 2. Energy delivered per change in transmittance in dB.

Grating Number	*Fiber Type*	*Temperature Sensitivity (pm/°C)*	*Uncertainty (pm/°C)*
7	FSBG15	15.20	± 1.65
8	FSBG15	16.20	± 1.66
9	FSBG15	15.40	± 1.65
10	980HP	16.90	± 1.66
11	PSGF	18.20	± 1.66
12	FSBG15	13.90	± 1.65
Average		**15.97**	**± 1.66**

TABLE 3. Data obtained from temperature test and the uncertainty associated with each set of measurements.

Conclusions

The purpose of this research is to provide fiber Bragg gratings for the research on compact fiber lasers that is being undertaken at the College of Optical Sciences at the University of Arizona, as well as to define their temperature sensitivity. Two of the gratings specified were not made because the setup was not stable enough to allow for their fabrication. The gratings not fabricated are the following: 980 at 50% reflectivity and PSGDF at 50% reflectivity.

In order for fiber Bragg gratings to be used as components of fiber lasers, their temperature sensitivities need to be reduced. The method to be employed to reduce the temperature sensitivity is to balance the thermo-optic coefficient and the thermal-expansion coefficient. In this research, the average temperature sensitivity of the fiber Bragg gratings was 15.97 pm/°C. More research needs to be done to determine precisely how to reduce this value.

References

1. G. W. Yoffe, Peter A. Krug, F. Ouellete, D. A. Thorncraft. “Passively temperature-compensating package for optical gratings.” *Applied Optics* 34.30 (1995): 6859-6861.
2. Hill, Kenneth O.; Meltz, Gerald. “Fiber Bragg Grating Technology Fundamentals and Overview.” *Journal of Lightwave Technology* 15.8 (1997): 1263-1275.
3. Suzuki, Shigeru; Schülzgen, Axel; Sabet, S.; Moloney, J. V.; Peyghambarian, Nasser. “Photosensitivity of Ge-doped phosphate glass to 244 nm irradiation.” *Applied Physics Letters* 89 (2006): 171913-171915.
4. A. Polynkin, P. Polynkin, D. Panasenko, M. Mansuripur, J. Moloney, N. Peyghambarian. “Short-cavity, passively modelocked fibre laser oscillator at 1.5 µm with 550 MHz repetition rate and high average power.” *Electronics Letters* 42.3 (2006).
5. Hyunwook Lee, Zhongxie Jin, Minho Song. “Investigation of fiber Bragg grating temperature sensors for applications in electric power systems.” SPIE 5634 (2005): 579-584.

Acknowledgements

This material is based upon work supported by the STC Program of the National Science Foundation No. DMR 012096.

Special thanks to: Shigeru Suzuki, Dr. Axel Schülzgen and Dr. Nasser Peyghambarian.

Syntheses of Chiral Compounds and Characterization by X-ray Diffraction and Optical Imaging

JOSE B GALLEGOS, Department of Chemistry: New Mexico Highlands University
Werner Kaminsky, Department of Chemistry: University of Washington

Introduction:

Understanding photonic materials on the basis of structural calculations is important for optimizing non-linear optical features in crystals. However, in crystals non-linear optical features are difficult to obtain experimentally since it requires rather large samples, whereas for a calculation of such properties only the atomic arrangement needs to be known and can be simulated or obtained from X-ray diffraction measurements on small specimen. Calculations based on quantum mechanics, which are sufficiently accurate for an isolated molecule, will neglect intermolecular interaction in crystals. Furthermore, classic calculations designed for inorganic crystals over simplify the orbital structure. Nevertheless, the classic model might be modified empirically to be applicable to organic crystals by reevaluating empirical parameters used in these calculations. For this task a series of syntheses was preformed of structurally related substances that must lack a center of symmetry: a necessary condition for being optically non-linear. Here, compounds resulting from aryl iso-thiocyanates (ITC) reacted with enantiopure chiral alcohols, which by design have a symmetry that lack an inversion center, were selected for such studies to allow for structure-non-linear optical property correlations related to photonic applications and an overall understanding of non-linear optical features in the bases of structural calculations of structures. The chirality of the alcohols enforces absence of centricity for the crystal symmetry. Because of the nature of non-linear optical properties, a center of symmetry would otherwise cause any non-linear response of the material to cancel out on the macroscopic samples. Furthermore, aromatic rings within the compound provide a high number of mobile electrons, which is important for potential nonlinear optical applications. Uniquely, ITC feature a –R=S linkage, which builds out selected hydrogen bonds, allowing for a structured molecular packing as well as an enhancement of crystal growth. Additionally, the sulfur within ITC scatters well for X-ray structure analysis and allows the use of anomalous diffraction to determine the hand of the chiral structures. However, not only enantiopure alcohols were used, instead, the reaction mechanism of ITC with various alcohols and aldehydes was investigated in order to achieve a better understanding of the chemistry involved.

Methods:

a) *Synthesis*. All reactions were based on the general procedure shown in scheme 1 (1).

The reaction with 4-chlorophenyl-ITC with α-methyl-benzamine (α-MBA) was preformed at 100^0 C and consisted of a drop wise insertion (4 to 5 drops per minute) of 4-chlorophenyl-ITC into excess α-MBA. The solution was allowed to slowly mix until the mixture was solid. The white mixture was then dissolved in a solvent consisting of 80% EtOH 20% MeOH and left for slow evaporation to grow proper crystals. A similar method was used for 4-bromo-ITC with α-MBA. The reaction was preformed at 60^0 and consisted of a drop wise insertion (4 to 5 drops) of 4-bromophenyl-ITC into excess α-MBA (1.5 mL). The mixture was allowed to slowly mix over night. The white powder material formed was then dissolved in 80% EtOH 20% MeOH and left for slow evaporation to allow the formation of crystals. The detailed procedure to react ITC with, for example, 2-butanol involved mixing and dissolving of the ITC in the alcohol with the aid of vortexing. The reaction was then heated at approximately 110^0 C for one hour and allowed to cool to room temperature. Crystals were then grown by slow evaporation of the solvent.

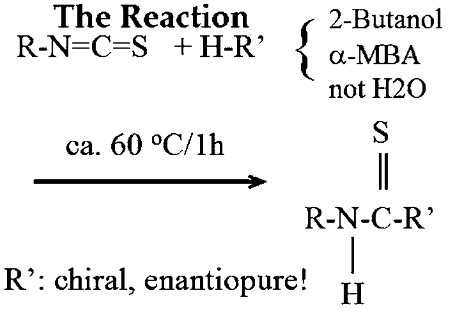

SCHEME 1. Reaction schematics

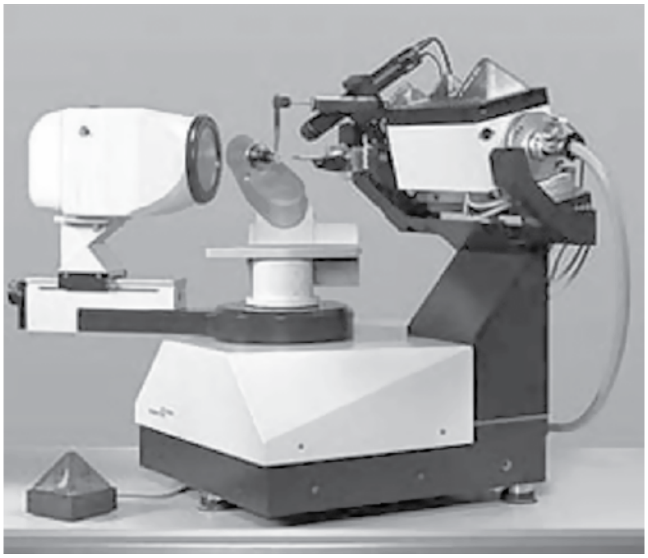

FIGURE 1. Kappa-CCD X-ray diffractometer (FR590)

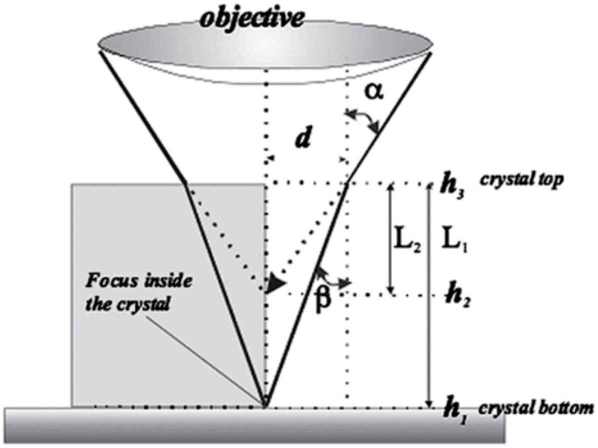

FIGURE 2. Experimental determination of absolute refractive indices using the 3-height method: , where n_{air} is assumed to be one.

$$\frac{n}{n_{air}} = \frac{\sin\alpha}{\sin\beta} \approx \frac{\tan\alpha}{\tan\beta} = \frac{d/L_2}{d/L_1} = \frac{L_1}{L_2} = \frac{h_3 - h_1}{h_3 - h_2}$$

b) *Measurements*. The molecular structures which show the molecular packing were determined by X-ray analysis with a Nonius-Kappa-CCD X-ray diffractometer (FR590) (Figure 1).

Refractive indices, which are required for semi-empirical model calculations to predict optical features, were obtained utilizing the 3-Height method (Figure 2).

Here a crystal is placed on a marked glass slide on a microscope stage and the foci settings for the mark seen next to the crystal and through it as well as the top of the crystal are measured and computed to give the refractive index. Additionally, absorption spectra were taken to study the available spectral regions for non-linear optical applications.

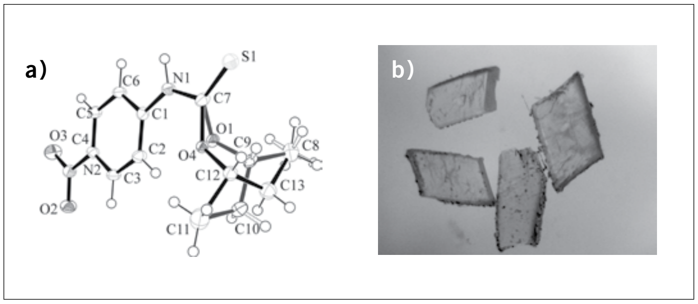

FIGURE 3. a) i-butyl-N-(4-nitrophenyl) thiocarbamate, The racemic mixture of the alcohol is evident in the disorder as well as space group symmetry of the compound. **b)** Crystals of this compound. The size of this photo and successive photos is 8mm across.

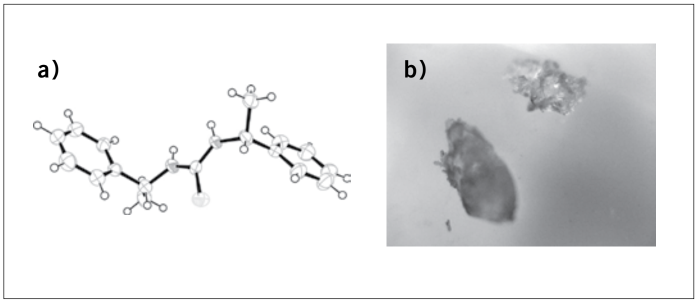

FIGURE 4. a) N-(4-chloro)-N'-[(1S)-1-phenylethyl]thiourea, α-MBA) and **b)** Crystals of the compound

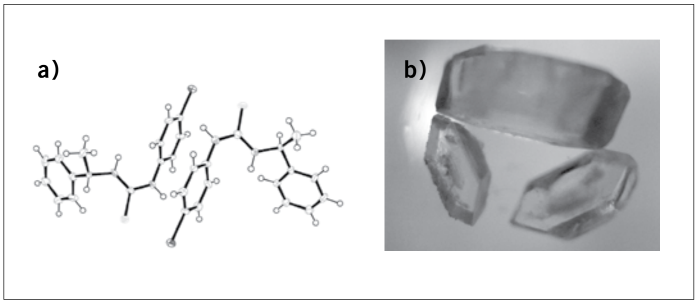

FIGURE 5. a) N-(4-bromo)-N'-[(1S)-1-phenylethyl]thiourea, α-MBA) and **b)** Crystals of the compound

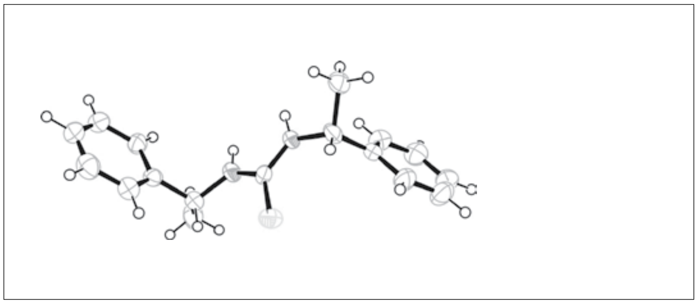

FIGURE 6. bis α-MBA-thiourea.

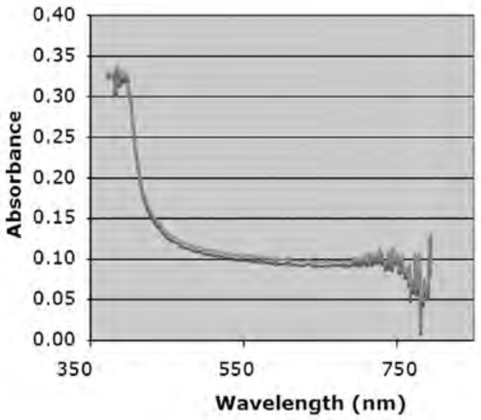

FIGURE 7. Absorption spectrum of compound figure 2

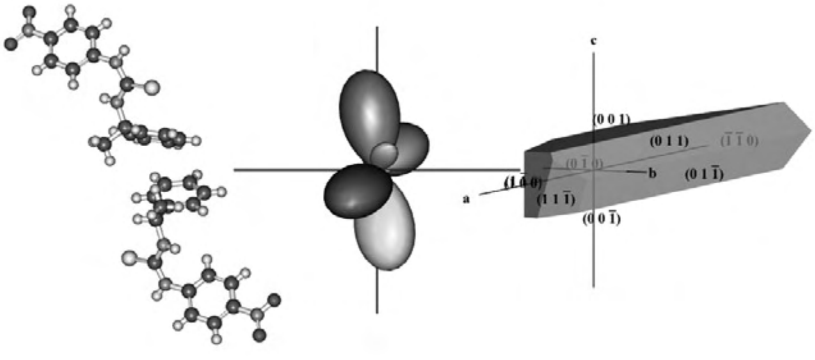

FIGURE 8. Structure plot, representation surface of the electro-optic effect, and morphology of 4-nitro ITC α-MBA.

Results and Discussion

Experiments with varying pH-values and temperatures were performed previously to find the best suitable reaction parameters for reacting ITC with alcohols. Keeping the reaction acidic supported the formation of the desired compounds, but the presence of water was found to prohibit the reaction with alcohol and instead the ITC moieties reacted with them self forming ureas. Re-crystallization of previous compounds consisting of 4-nitrophenyl ITC and other ITC's with R/S-2-butanol (Figure 2) and with α-methyl benzyl amine (α-MBA) was performed to produce better samples for the continuation of tests on the new series of chiral carbamates and ureas.

Two new compounds were synthesized from reacting 4-chlorophenyl ITC (figure 4) or 4-bromophenyl ITC (figure 5), with α-MBA, respectively.

Both new compounds are of space group P 2_1. To avoid a charged crystal, the ITC moieties align antiparallel, thus connecting two molecules in a dipole-induced dimer.

It was attempted to react phenyl ITC with α-MBA using the same procedure as for the other materials, however, X-ray analysis revealed that the α-MBA reacted with itself to form a urea that had been publisehed elsewhere (2).

This compound however is still welcomed as it is also non-centrosymmetric and will be studied further.

Except for the nitro compound no absorption was found in the accessible spectral range (figure 7).

Further studies will include calculations of optical properties. Such studies were carried out on the first material of the series of chiral ureas studied: nitro ITC reacted with α-MBA, which have not been reported so far. This compound was synthesized by others previously (undergraduate students: Dan Daranciang, Bao Chau Ngoc Tran, and Tram-Anh Pham) and tensorial properties were calculated. We measured the refractive indices and birefringence of the crystal face perpendicular to the c-axis of the crystal. In the visible spectral range the values and directions are approximately 1.61(2) along the a-axis and 1.49(2) perpendicular to that in the projection of the crystal face. Turning the crystal around we found that these two are to be extended by a third, bigger value. The calculated refractive indices with similar polarizations as the observed ones are 1.504, 1.573, 1.767.

There are five elements in this structure: H, C, O, S, and N. Each reacts to light in a different way represented by a number: the electronic polarizability volume. The larger the electronic polarizability volume the stronger the atoms interact with light. The calculations which involve dipole-dipole interaction in crystals allow predicting values for different optical properties (3). We calculated the electro-optic effect for the amount of optical rotation of linear polarized light and the amount to which the refractive indices change when a static electric field is applied to the crystal.

Figure 8 shows the structure, representation surface of the calculated electro-optic effect and crystal morphology. The electronic susceptibilities, normalized to the dielectric constant reach 3pm/V, which is large for a crystal. With an assumed dielectric constant of around 10 to 20, the r-value of this compound would be around 30 to 60 pm/V which is in the range of other commercially used crystalline photonic materials

References

1. M. Avalos, R. Babiano, A. Cabanillas, P.Cintas, F. J. Higes, J. L. Jimenez, and J.C. Palacios: Cycloaddition Chemistry of 1,3-Thiazolium-4-olate Systems. Reaction with Nitroalkenes and Interpretation of Results Using PM3 Calculations. *J. Org. Chem.* 1996, 61, 3738-3748
2. P. W J. Bailey, K. J. Grater and S. Parsons: Bis[(S)-(-)-α-methylbenzyl]thiourea. *Acta Cryst.* (1997). C53, 247-248.
3. K.Claborn, B. Kahr, W. Kaminsky: Calculation of optical properties of the tetraphenyl-X family of isomorphous crystals (X=C, Si, Ge, Sn, Pb). Cryst. Eng. Comm. 4 (2002) 252-256.

Acknowledgements:

We are grateful to Prof Bart Kahr for use of lab space for the chemical investigations. We also would like to thank previous undergraduate students who contributed to this research project (Thao Tran, Dan Daranciang, Donald Responte, Crystal Chang, Bao Chau Ngoc Tran, Donald Responte, and Tram-Anh Pham). Finally a special thank to CMDITR (DMR-0120967) and Hooked on Photonics (CHE-0453596) for funding and participation.

JOSE GALLEGOS. After obtaining my B.S. degrees in Chemistry and Geology I plan to pursue graduate school for chemistry and/or geochemistry.

Optimization of Organic Photovoltaics

Based on a poly(3-hexylthiophene) (P3HT) and phenyl-C61-butyric acid methyl ester (PCBM-C60) Heterojunction

ANTHONY GIORDANO, William Potscavage, Seunghyup Yoo, Benoit Domercq and Bernard Kippelen, School of Electrical and Computer Engineering, Center for Organic Photonics and Electronics (COPE). Georgia Institute of Technology

Introduction

Solar cells should be considered an important aspect of power production for the present day and beyond due to their low environmental impact and high energy production. Specifically, when a solar cell is exposed to sunlight, the energy contained within the incident light is converted into electricity without any movement or production of pollution.[1] So far, mass marketed solar cells have been based on the use of crystalline or amorphous silicon in various forms.[2] While the power conversion efficiencies of such silicon based cells have proven to be quite high, the lure and potential for photovoltaic technology using organic materials has become a point of great interest. In particular, organic solar cells have potential to decrease production costs, to be placed on a flexible surface, and to be used in numerous portable applications.

In order to attain these potentials, research regarding organic photovoltaic cells has emphasized the use of polymers and other organic molecules.[3] The use of electron donor/acceptor mixtures of organic compounds allows for the formation of a dispersed or bulk heterojunction.[4] The principle behind an organic heterojunction is the formation of an electron-hole pair or exciton under illumination and its dissociation with the charges going into the highest occupied molecular orbital (HOMO) and the lowest unoccupied molecular orbital (LUMO) of the donor and acceptor, respectively, to produce a current.

As shown in Figure 1 a photon (hν) enters the system and is absorbed. This absorption causes the formation of an exciton which diffuses toward the heterojunction. Under energetically favorable conditions, the exciton undergoes dissociation to produce free charges. The electrons and the holes are collected by the cathode and the anode to produce a current.

In a bulk heterojunction junction, the electron accepting and electron donating layers are essentially blended together with one another. This means that excitons should, on average, have a shorter distance to diffuse to reach the donor/acceptor junction in a bulk heterojunction than a planar heterojunction. Through this blending, the efficiency of exciton dissociation into charges at the donor/acceptor interface greatly increases since there is a greater probability that dissociation will occur before recombination. The important point to remember with bulk heterojunctions is that each material must provide a continuous path from the area of dissociation to the electrical contacts on the outer surfaces of this junction.[4]

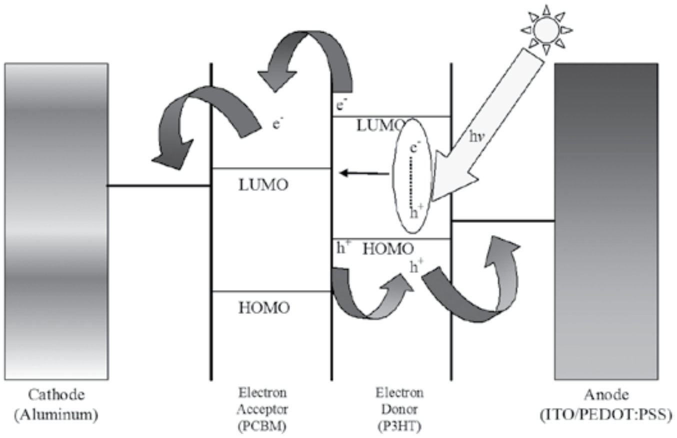

FIGURE 1: Schematic of the P3HT/PCM-C60 heterojunction

At this point in time, efficiencies of heterojunction organic photovoltaics approaching 5% are common place.[5] Such efficiencies were obtained by using poly(3-hexylthiophene) (P3HT) for the electron donor and phenyl-C_{61}-butyric acid methyl ester (PCBM-C_{60}) for the electron acceptor. The structures for P3HT and PCBM-C_{60} can be seen in Figures 2 and 3. Each fabricated device had the following structure: ITO/PEDOT-PSS/P3HT:PCBM-C_{60}/Al where PEDOT is poly(3,4-ethylenedioxythiophene, PSS is poly(styrenesulfonate) and ITO is indium tin oxide.[5] It should be noted that the ITO and PEDOT-PSS layers act as the hole collection electrode and aluminum acts as an electron collector electrode (see Figure 1).

The question remains, however, of whether or not these systems can be further optimized to produce higher levels of power conversion efficiency (the overall power output by the solar cell divided by the power provided by the light incident to the cell)[3,5] Power conversion efficiency (η) can be calculated from the key parameters of a solar cell under illumination power (I_L) of the short-circuit current (I_{sc}) and open-circuit voltage (V_{oc}). The efficiency calculation also uses the maximum power point, which corresponds to a and produces the following relationship[6]

$$\eta = \frac{I_{sc}V_{oc}}{I_L}\frac{V'I'}{I_{sc}V_{oc}} = \frac{V'I'}{I_L}\ . \quad \text{(Equation 1)}$$

Since the fill factor (*FF*) can be defined in terms of the voltage and current required to achieve the maximum power point (and respectively), as well as the I_{sc} and V_{oc}, the following relationship follows from Equation 1

$$\eta = \frac{I_{sc}V_{oc}FF}{I_L}\ . \quad \text{(Equation 2)}$$

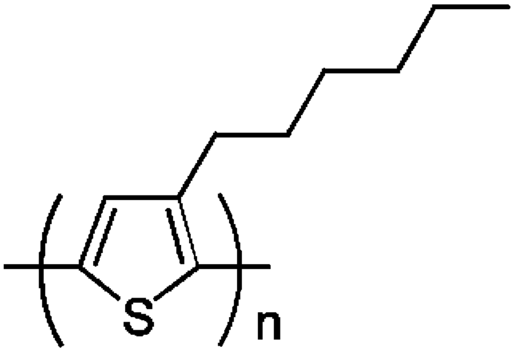

FIGURE 2: Structure of P3HT

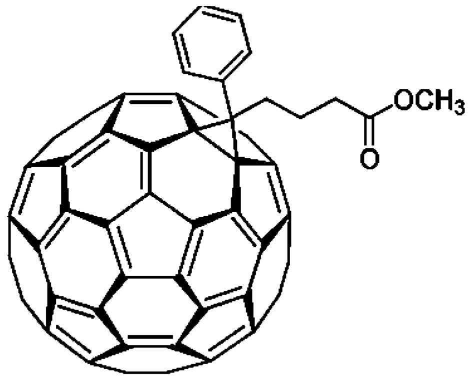

FIGURE 3: Structure of PCBM-C60

The overarching goal of the study is to examine the fabrication techniques for the P3HT:PCBM-C_{60} photovoltaic cells, and determine what conditions are necessary to maximize the efficiencies. Thus, Equation 2 is extremely important since both FF and η are the main parameters under which the completed photovoltaics will be examined. This optimization is necessary to test the viability of commercially available P3HT and compare the results obtained to those found in literature sources. This experimentation required the fabrication of solar cells using different thermal annealing times and temperatures. Similarly, the ratio of P3HT:PCBM-C_{60} was varied in order to determine the optimal ratio of these two compounds.

Experimental Methods

Solar cells were fabricated on ITO-coated glass from Colorado Concept Coatings LLC and cut into 2.46×2.46 cm square pieces. Part of the ITO was masked with Kapton tape for protection during the etching step. Then the substrate was dipped into a magnesium turnings and concentrated hydrochloric acid solution to remove the unmasked part and define the active area. Prior to solar cell fabrication, the etched ITO-coated glass was cleaned using the following series of baths: detergent, deionized water, acetone, and ethanol (the samples were dried with nitrogen between steps). All steps were performed within a sonicator for 30 minutes each, and the final two steps of acetone and ethanol were heated to approximately 35°C. The substrates were dried in a vacuum oven at 85°C overnight.

After cooling, the substrates were oxygen plasma treated for 2 minutes to remove any residual organics and activate the surface. PEDOT-PSS (Baytron P VP AI 4083 by H.C. Stark) was filtered through a 0.45 μm PVDF syringe filter and spin coated on the substrate at 5000 rpm for one minute. Each sample was then soft baked on a hot plate for 10 minutes at 140°C to remove any remaining solvent and subsequently transferred into a nitrogen filled glove box for the spin coating of the organic photoactive layer.

Solutions of P3HT (Rieke Metals) and PCBM-C_{60} were made using chlorobenzene as the solvent at a concentration of 18 mg/mL. The solutions were then mixed at varying ratios and stirred for several days to ensure dissolution. These solutions were passed through a 0.2 μm PTFE syringe filter and spin coated on the ITO/PEDOT-PSS substrates at 700 rpm for one minute. To ensure proper contact between the aluminum and ITO/PEDOT-PSS layers, 4-5 mm of the organic layer was removed from the top of the substrate using chlorobenzene.

Aluminum electrodes of approximately 200 nm in thickness were deposited by physical vapor deposition on top of the P3HT:PCBM-C_{60} through a shadow mask at a base pressure of about 10^{-7} Torr. Annealing was performed inside the glove box on a hotplate. The time and temperature of the annealing were varied.

After samples had cooled to room temperature, measurements were performed in a nitrogen filled glove box to minimize device degradation. A xenon lamp (CVI, ASB-XE-175EX) was used as a broadband light source (350 – 900 nm). This light was passed through filters to closer approximate AM 1.5G light, or the standard solar spectrum. A photodetector was used before each test to determine the irradiance of the light source. Each device was then tested under the illumination as well as under dark conditions.

Results and Discussion

Figure 4 shows the *J-V* curves of three solar cells fabricated using various weight ratios of P3HT:PCBM-C_{60} with all samples annealed at 150°C for 30 minutes. Each graph shows the electrical characteristics of the devices under light and dark conditions. For a P3HT:PCBM-C_{60} ratio of 0.8:1 (Figure 4a), the average values over 5 devices of V_{oc}, J_{sc}, and FF were 0.6 V, 11.9 mA/cm^2, and 0.26 respectively, leading to an average efficiency of 1.85%. In Figure 4b, the ratio is 1:1, which led to a similar average value V_{oc} than the 0.8:1 ratio (over 3 devices) but with a slight increase in the average J_{sc} to 12.3 mA/cm^2 and an increase in the average FF to 0.3. Consequently, the efficiency rose to 2.0%. With a solution of 1:0.8 (Figure 4c) another increase in efficiency is observed. The devices exhibit average values (over 5 devices) for V_{oc}, J_{sc}, and FF of 0.6 V, 13.0 mA/cm^2, and 0.34 respectively. The average efficiency was calculated to be 2.65%, but it is important to note the variation between each device on a single substrate, which is not ideal behavior. The actual shapes of the curv es also differ from normal diode behavior, which resembles an exponential curve. Instead, there are unwanted deviations from normal exponential behavior.

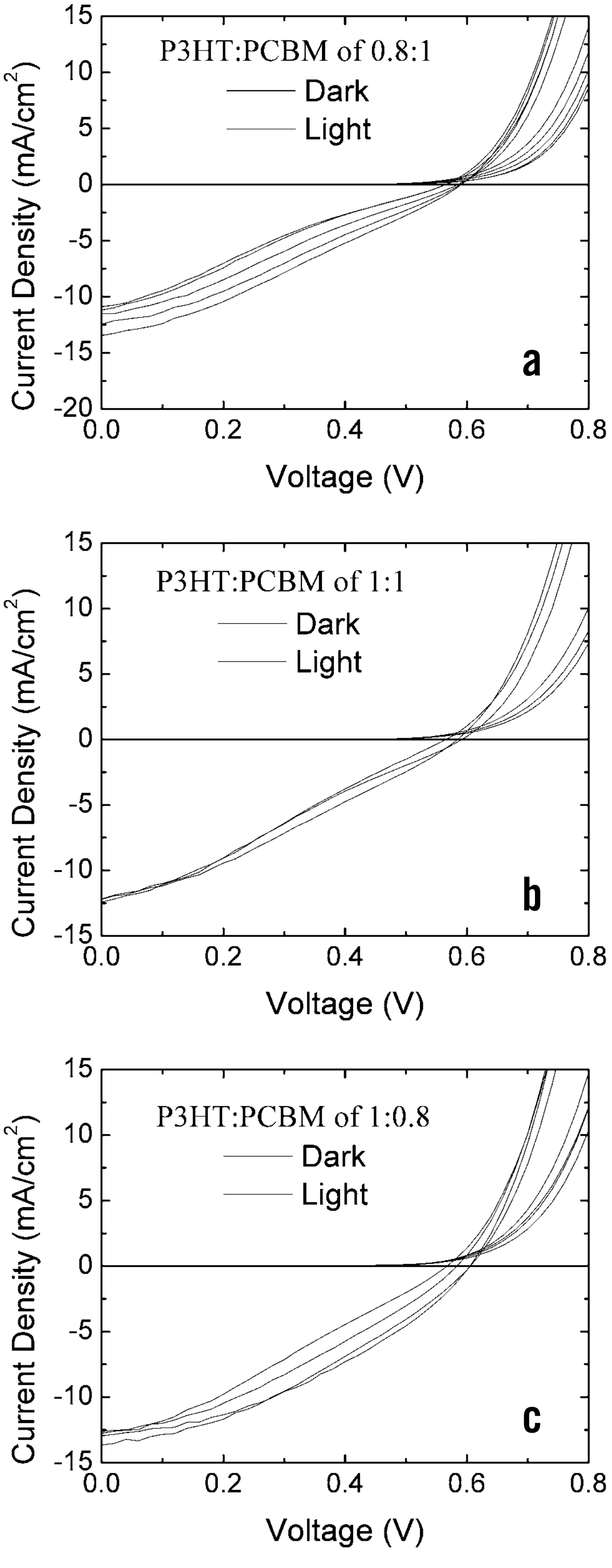

FIGURE 4: Current density (J) as a function of applied voltage (V) for devices made from solutions of P3HT:PCBM-C60 with weight ratios of 0.8:1 (a), 1:1 (b), and 1:0.8 (c). The diode behavior for these samples progressively increases from (a) to (c). The black curve is the electrical characteristic in the dark.

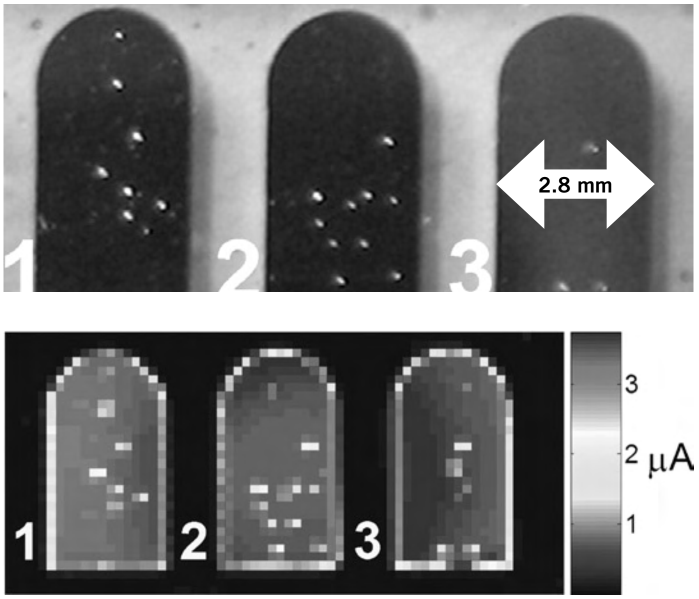

FIGURE 5: A. Surface aggregation of P3HT and PCBM-C60 resulting in visible defects on the aluminum contacts. b. Graph of current obtained through the use of a laser. Note the correspondence between the drop in device current (dead spots) and the defects in the aluminum surface. Numbers are present to show the correspondence between devices.

These experimental conditions were repeated using the same fabrication conditions. The 0.8:1 solution gave an average η of 2.4%, 1:1 exhibited an average η of 1.9%, and the 1:0.8 solution demonstrated average efficiency of 3.0%. Thus, a solution that is 1:1 in terms of P3HT:PCBM-C_{60} is clearly less efficient than a solution of 1:0.8. Yet, further testing would be needed in order to determine the relationship that exists between the 0.8:1 and 1:1 solutions. The data does indicate that the efficiency of the device increases when there is more P3HT than PCBM-C_{60} present in the solution.

Utilizing an annealing process of 150°C for 30 minutes resulted in irregularities on the metal surface. These abnormalities can be seen in Figure 5a and are not present after depositing the aluminum metal. Rather, such defects are similar to those reported in reference 7, which were found to be caused by aggregation of PCBM-C_{60}. During this process, the heat energy transferred to the P3HT and PCBM-C_{60} molecules causes movement, which can then initiate changes in the surface of the aluminum. Such an alteration in the surface structure is a likely factor in the lower than expected efficiencies. Reference 5 was able to attain efficiencies approaching 5% using the same methods, but no irregularities of the surface were reported. These defects were then analyzed through the use of light beam induced current (LBIC) where a laser is shined on the active site of the photovoltaic (Figure 5b). This allowed for the mapping of current across the device, and showed that a one-to-one correspondence exists between the defects and the electrical dead spots of the device. This leads to another possible explanation involving the T_g of the P3HT. The temperature used for annealing might be high enough that the glass transition temperature (T_g) of the P3HT is surpassed, which causes stress on the aluminum layer resulting in the visible defects.

Devices fabricated using solutions of 1:1 and 1:0.8 P3HT:PCBM-C_{60} were annealed before depositing the aluminum metal on the surface of the device and annealed again after deposition of the aluminum was completed. Annealing before depositing the aluminum contacts at 150°C for 30 minutes resulted in average values (over 3 devices) for V_{oc}, J_{sc}, and FF of 0.5 V, 10.8 mA/cm^2, and 0.27, respectively, for a solution of 1:1 and average values for V_{oc}, J_{sc}, and FF of 0.5 V, 9.9 mA/cm^2, 0.26, respectively, for a solution of 1:0.8. Thus, the 1:1 sample produced an average η of 1.4% and for the 1:0.8 sample the average efficiency was 1.2%. Upon further annealing at 125°C for 30 minutes the average efficiencies increased slightly to 1.5 % for the 1:1 solution and to 1.4% for the 0.8:1 solution. This indicates that there may be a need for the morphology of the P3HT/PCBM-C_{60} to be changed after depositing the aluminum metal. Thus, the efficiencies of the first set of devices, coupled with this data, suggests that the morphology changes required to make an efficient device are not limited to only the heterojunction. Rather, all aspects of the completed device need to be annealed simultaneously and not in a piecewise manner. The data also suggests that once the morphology has been significantly changed before addition of the aluminum layer it cannot be readily altered to a state that will increase the efficiency of the device.

Another set of samples was also fabricated where annealing occurred after addition of the aluminum layer at 125°C for 30 minutes. Figure 6 shows the *J-V* curves for these samples.

Figures 6a and 6b are the curves obtained before annealing devices made from 1:1 and 1:0.8 solutions, respectively. At this point the devices have poor diode behavior under light and dark conditions. The average values (over 3 devices) obtained for the unannealed 1:1 sample for V_{oc}, J_{sc}, and FF are 0.6 V, 1.8 mA/cm^2, 0.26, respectively, with an average η of 0.3%. The data collected for the 1:0.8 solution gave average values for V_{oc}, J_{sc}, and FF of 0.6 V, 4.0 mA/cm^2, and 0.29, respectively, leading to an average η of 0.7%. The devices were then annealed at 125°C for 30 minutes. As shown in figures 6c (1:1) and 6d (1:0.8), the behavior of the devices is greatly altered. This time, the average values obtained for the 1:1 samples for V_{oc}, J_{sc}, and FF were 0.5 V, 13.4 mA/cm^2, 0.35, respectively, with an average efficiency of 2.5%.

The 1:0.8 sample has an even greater increase in performance with average values for V_{oc}, J_{sc}, and FF of 0.6 V, 12.4 mA/cm^2, and 0.40, respectively, with an average η of 3.0%. The curves produced for these annealed devices have a much greater tendency toward diode behavior, as the fill factors confirm. The fill factors are examined to determine diode behavior because the fill factor (Equations 1 and 2) essentially measures how well the current density and voltage at the maximum power point fills the short circuit current density and open circuit voltage. It should also be noted that minimal amounts of aggregation were noted on the aluminum surface. Therefore, the data and observations indicate that annealing devices at a lower temperature of 125°C for the same amount of time can produce a boost in overall efficiency and fill factor. Similarly, these results also confirm that having more P3HT in the solution increases overall device performance.

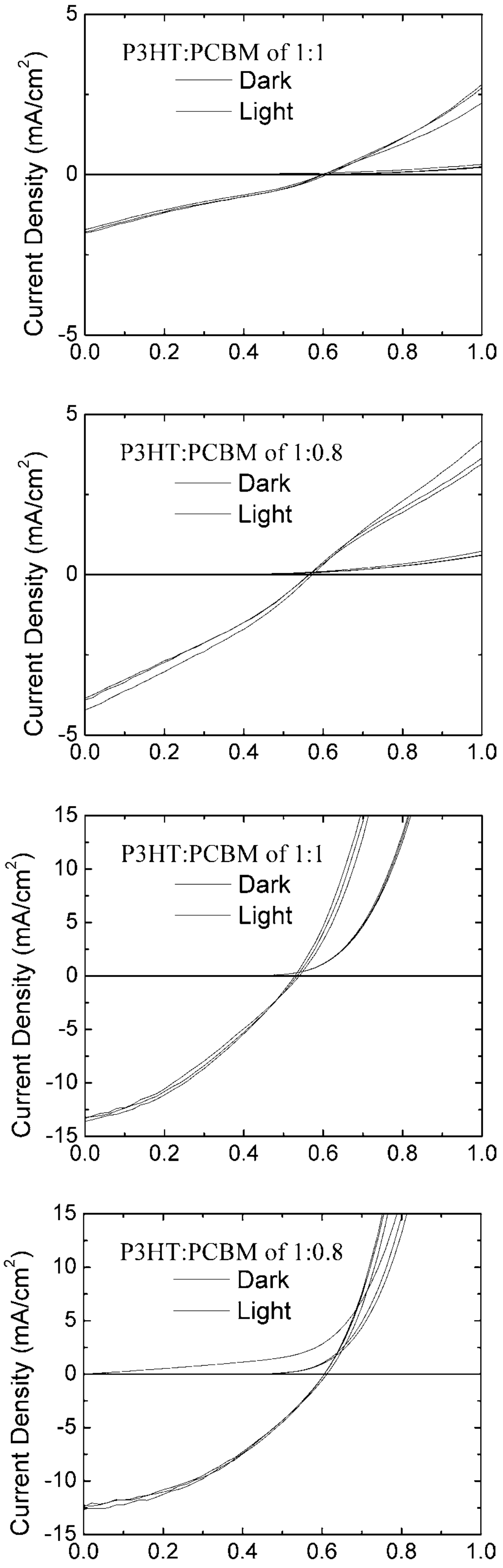

FIGURE 6: Current density (J) as a function of applied voltage (V) for samples fabricated using a 1:1 P3HT:PCBM-C60 solution (a and c) and a 1:0.8 solution (b and d). In a and b the samples were not annealed, but c and d show the curves after the samples had been annealed at 125°C for 30 minutes.

Conclusions

The power conversion efficiency of organic solar cells depends greatly on the ratio of P3HT and PCBM-C_{60} used for the bulk heterojunction as well as the temperature at which the devices are annealed. Such devices have efficiencies of approximately 3% when a 1:0.8 ratio of the two materials is used and the samples are annealed at 125°C. Since literature values have been found to be much higher, this indicates that improvement in the fabrication techniques can still occur.[5] This emphasizes the importance of optimizing chemicals in different laboratories. The efficiency increase from annealing results in alteration of surface morphology, which increases the transport of charge throughout the active area.[5]

The need to economically and consistently produce highly efficient solar cells makes future research in this area extremely necessary. In order to further optimize the process, future testing should be performed to determine the influence annealing time at 125°C has on the samples, and if this is truly the most optimal annealing temperature. Also, other sources of the P3HT should be tested to determine if an increase in device efficiency occurs when chemicals from a different manufacturer are used, or chemicals from a different synthetic batch produced by the same manufacturer are used. This testing is necessary since it is possible that different synthetic routes could result in different regio-regularity of the final product.[8] Future studies should also examine the EQE of the samples produced to determine how fabrication conditions affect absorption and charge generation at different wavelengths of the solar spectrum.

References

1. Green, M. A. *Solar Cells: Operating Principles, Technology and System Applications.* PLT Print Solutions: Kensington, NSW, 1998.
2. Goetzberger, A.; Hebling, C.; and Schock, H. *Mat. Sci. Eng. R.* 2003, 40, 1-46.
3. Spanggaard, H.; Krebs, F. C. *Sol. Energy Mat. Sol. Cells.* 2004, 83, 125-146.
4. Nelson, J. *Cur. Op. Solid State Mat. Sci.* 2002, 6, 87-95.
5. Ma, W.; Yang, C.; Gong, X.; Lee, K.; Heeger, A. J. *Adv. Funct. Mat.* 2005, 15, 1617-1622.
6. Yoo, S.; Domercq, B.; Kippelen, B. *App. Phys. Lett.* 2004, 85, 5427-5429.
7. Chirvase, D.; Parisi, J.; Hummelen, J. C.; Dyakonov, V. *Nanotechnology.* 2004, 15, 1317-1323.
8. Kim, Y.; Cook, S.; Tuladhar, S. M.; Choulis, S. A.; Nelson, J.; Durrant, J. R.; Bradley, D. D. C.; Giles, M; McCulloch, I.; Ha, C.; and Ree, M. *Nat. Mat.* 2006, 5, 197-203.

Acknowledgements

Funds for this research were provided by the Center on Materials and Devices for Information Technology Research (CMDITR), and the NSF Science and Technology Center No. DMR 0120967. Special thanks go to William Potscavage for his excellent advice, help, and patience throughout the experience. I also wish to thank Dr. Benoit Domercq for his aid in the entire REU experience. Thanks to Dr. Bernard Kippelen and his entire group for their support and willingness to work with me during the project.

I am **ANTHONY GIORDANO**, and I currently attend Regis University where I am working toward a double major in Chemistry and Mathematics. I truly enjoy conducting research, and plan on pursuing a Ph.D. in Chemistry after graduation.

Measurement of Small-Scale Fading Distributions in a Realistic 2.4 GHz Channel

ALEXANDER H. HENDERSON, Furman University, Greenville, SC, 29613
Prof. Gregory D. Durgin and Christopher J. Durkin, Georgia Institute of Technology, Atlanta, GA 30332

Introduction

Characterization of wireless signal fading is of growing interest due to the proliferation of cell phones, wireless monitoring equipment, and other wireless devices. While large-scale fading typically describes relative reception over distances many times the wavelength(s) being considered, small-scale fading leads to the most unpredictable dips in transmission strength or even complete loss of signal (a "null") and consequent termination of the connection [1, p.34]. Consequently, information on small-scale fading and how to correct for it proves useful to radio designers.

Small-scale fading refers to the varying strength of wireless signals within a local area due to the constructive and destructive interference of multipath waves resulting from reflection and diffraction off of nearby scattering surfaces [1, p.34]. It is typically assumed that in such a situation, Rayleigh statistics will be the worst possible distribution in terms of points where the signal strength drops below a certain pre-determined threshold [1, pp. 7-8], while a Ricean curve is used to describe a case of one strong line-of-sight element with all other contributions being weaker, which is a good approximation for certain real situations [1, pp. 127-128]. Work by Frolik indicates that certain situations experience "Hyper-Rayleigh" fading, though this occurs only in specific, highly dispersive cases [3].

Rayleigh statistics assumes that there are no specular wave components and a diffuse, nonspecular component. A specular component is an individual electromagnetic wave, here assumed to be of significant strength by itself, while a diffuse component is one which is composed of a number of waves whose individual strengths are small in comparison to the component's total strength. The Ricean model, conversely, assumes that there is a single specular component, which is typically a line-of-sight component, in addition to the diffuse component. Mathematically, the probability density function (pdf) for a Rayleigh distribution is $\frac{r^2}{\sigma^2}\exp(\frac{-r^2}{2\sigma^2})$, where *r* is the magnitude of the received voltage and σ^2 is the variance in the data. A Ricean pdf is $\frac{r^2}{\sigma^2}\exp(\frac{-r^2-V_1^2}{2\sigma^2})I_0(\frac{rV_1}{\sigma^2})$, where *r* and σ^2 are as above, V_1 is the magnitude of the voltage of the specular component, and $I_0(.)$ is a zeroth-order modified Bessel function.

There have been many measurement campaigns to characterize the wireless channel for large-scale fading. Propagation characteristics inside buildings used for various industrial, laboratory, and office purposes have been conducted at various frequencies and under various conditions, such as between floors and inside of offices [5] [6]. Studies have also been performed for various outdoor or between-building environments [2][4]. However, far fewer studies have been performed on small-scale fading.

FIGURE 1A: Receiver apparatus, mounted to a linear positioner.

FIGURE 1B: Transmitter apparatus, as mounted for the line-of-sight measurements.

The purpose of this study is to measure and characterize small-scale fading for a realistic, indoor propagation environment.

Experimental/Computational Method

For this experiment, a custom quarter-wavelength monopole antenna was used in combination with an amplifier and a bandpass filter to form a receiver, while a spectrum analyzer in conjunction with a computer system recorded data. A pure tone signal was generated using two signal generators and a frequency mixer, amplified, and transmitted at a frequency of 2.43 GHz from an omnidirectional antenna located more than ten wavelengths from the receiver. The receiver was mounted on a linear positioner, and measurements were taken at regular intervals as it was moved down the track. Figure 1 shows the different parts of a typical setup.

Measurements were conducted in a lab room on the top floor of the Van Leer building at the Georgia Institute of Technology. The room is approximately 3 ½ meters wide and 7 meters long, and contains a large number of scatterers, distributed around the sides of the room. Of particular note are two large metal cabinets which were on the far side of the room from the transmitter, facing back towards the transmitter.

As a check on the instruments and processing, data was taken on the noise present in the channel when no transmitted signal was present. For the next set of measurements, the transmitter was placed just outside of the room with a clear line-of-sight (LOS) through an open doorway for the entire area over which the measurements were made. Subsequently, data was also taken with the transmitter placed behind the wall adjoining the doorway, and with the transmitter placed over 7 meters down the hallway with several walls and two offices between the transmitter and receiver on the direct LOS path.

Subsequent analysis was performed using MATLAB and commonly known distribution types. Standard parameter finding methods were used to find the variance and mean for a Rayleigh fit to the data. In order to obtain an unbiased Ricean fit, a Maximum Likelihood (ML) estimator put forth by Sijbers et al. was used [7]. Taking a cue from the Ricean fitting method, a ML estimator was devised for use in fitting a Two-Wave-Diffuse-Power (TWDP) curve.

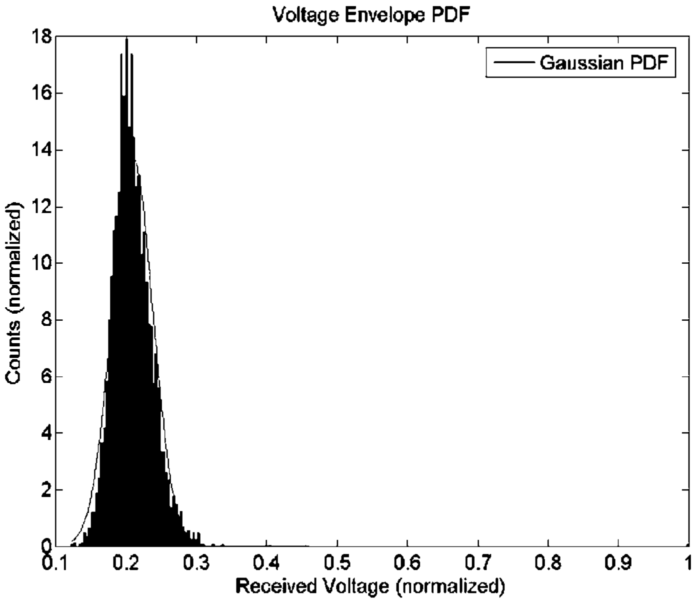

FIGURE 2: Histogram for noise data. Received voltage magnitude is normalized so that the highest value is 1.

Results and Discussion

Data was first taken on the noise in the system: the receiver apparatus was connected, but without any transmitted signal, and data was collected at the same frequency as it would be later in the experiment. This was done in order to ascertain the noise level in the system. In subsequent measurements, any measurement indistinguishable from noise could be discarded based on this data, though in practice the signal turned out always to be strong enough that this was not necessary. Figure 2 shows the histogram of this data with an overlaid Gaussian fit. As expected, this data was Gaussian distributed. The variance in the noise in the system was found to be about 0. 841 µW (-30.8 dBm). There was some 802.11 interference, seen as an outlier point in the graph. The occurrence of this event was felt to be sufficiently low (1 out of more than 2000 uncorrelated measurements) as to not interfere with further measurements.

The data was first normalized such that the highest value was set equal to zero dB, then converted to a linear scale from the original logarithmic form, thus making the subsequently constructed graphs more readable. Subsequently, histograms were constructed from the data, and probability density functions (pdfs) generated in the aforementioned manner. In order to obtain a TWDP fit, numerical techniques were found to be impractical. Consequently, the approximation: $\sum_{i=1}^{M} a_i D(\frac{r}{\sigma^2}; K, \Delta \cos\frac{\pi(i-1)}{2M-1})$, where *r* and σ^2 are as defined previously, $K = \frac{V_1^2 + V_2^2}{2\sigma^2}$, where V_1 and V_2 are the magnitudes of the voltages of the specular components, $\Delta = \frac{2V_1V_2}{V_1^2 + V_2^2}$,

and $$D(x;K,\alpha) = \frac{1}{2}\exp(\alpha K) I_0(x\sqrt{2K(1-\alpha)}) + \frac{1}{2}\exp(-\alpha K) I_0(x\sqrt{2K(1+\alpha)})$$,

where $I_0(.)$ is a zeroth-order modified Bessel function of the first kind, and the a_i are coefficients, formulated by Durgin et al. in [8] was used, to fifth order in *i*. It is worth noting that using ML theory, the log-likelihood function for this formula results in more than one local maximum in V_1, V_2, and σ in the range for all three parameters ≥ 0, requiring one to compare the values at all such points to find the global maximum. In testing this method on the data gathered, at least 2 local maxima in that range always resulted: one with V_1 and V_2 nearly equal, one with V_2 nearly equal to zero. In some tests, a third point appeared, wherein the value for K would be exceptionally small (low signal-to-noise ratio (SNR)). This third point was not considered in later tests, owing to the SNR being obviously higher than that given by this point.

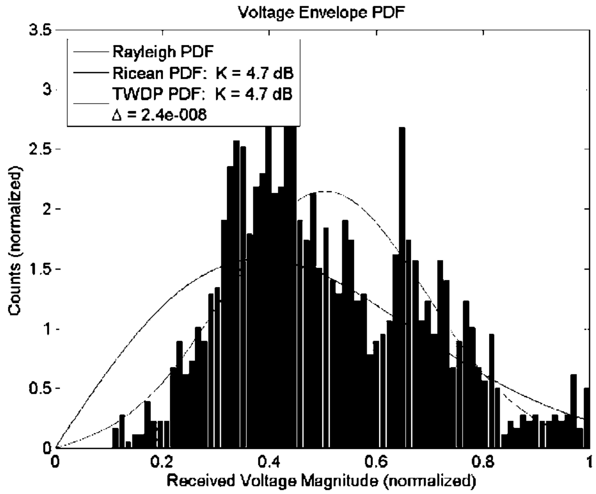

FIGURE 3A: Histogram of received voltage magnitude measured in a local area with overlaid pdf models. The received envelope is normalized such that the highest value is set to 1. Note that the Ricean and TWDP PDFs are not visually distinguishable.

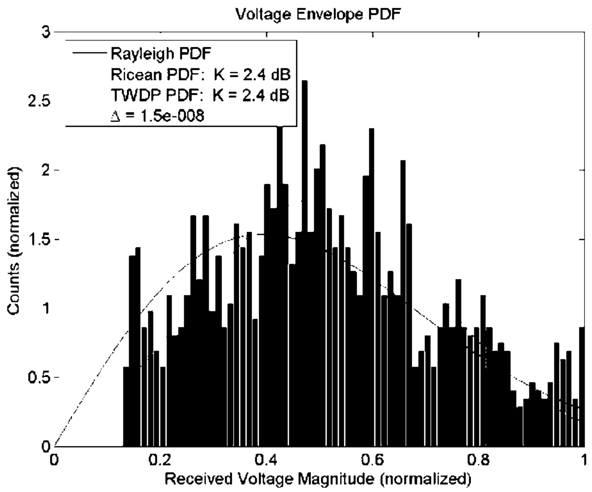

FIGURE 3B: Histogram of received voltage magnitude measured in a local area with overlaid pdf models. The received envelope is normalized such that the highest value is set to 1. Note that the Ricean and TWDP PDFs are not visually distinguishable.

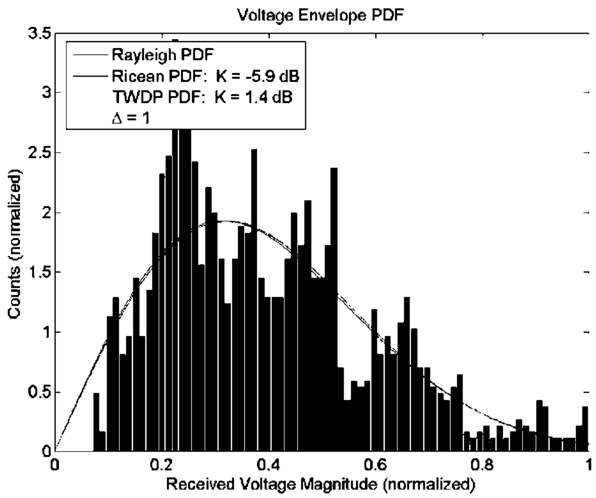

FIGURE 3C: Histogram of received voltage magnitude measured in a local area with overlaid pdf models. The received envelope is normalized such that the highest value is set to 1. Note that the three PDFs are not visually distinguishable.

Figure 3 shows histograms from a few representative data runs, with various probability density functions overlaid. For the data set in 3a, the K-value for the Ricean distribution was found to be 4.7 dB, using the ML estimator mentioned above. While a Ricean distribution was expected since there was a strong line-of-sight component, the fit for this distribution was bad, with a root-mean-squared (rms) error of 0.49 normalized counts, which was still significantly better than the Rayleigh fit, which had an rms error of 0.59 normalized counts, some 20% higher. For comparison, the rms error of the Ricean fit in figure 3b, which is visually Ricean distributed, is 0.38 normalized counts, a good 22% lower. In all, for the four runs where there was an unobstructed line-of-sight between the transmitter and the receiver, two showed the expected Ricean distribution as in figure 3b, one showed a Rayleigh distribution, as in figure 3c, and that shown in figure 3a did not adequately fit any of the standard pdfs. For the trial which showed a Rayleigh distribution, it was hypothesized that part of the transmitter's line-of-sight may have been blocked by the door, and the transmitter was subsequently moved slightly to reduce this possibility, though such obstruction was not clearly ascertainable. For the two measurements taken with a wall between the transmitter and receiver along the line-of-sight, one trial showed a Ricean distribution, leading to suspicion that the wall was letting a significant amount of signal through, and one showed a distribution comparable to that in 3a. While detailed tests on this were not conducted, there appeared to be a loss of from 4 to 11 dB through the wall at this frequency: not enough to eliminate the LOS component for this equipment, merely lowering the measured voltage levels. See table 1 at the end of this section for the values of the rms error for all three fits for all eight trials.

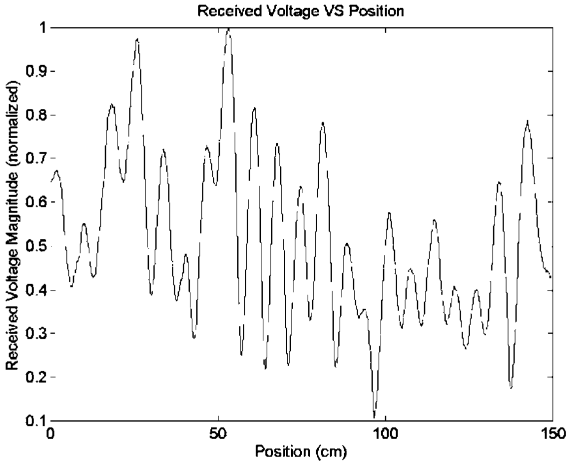

FIGURE 4A: Graph of a small-scale fading received envelope versus position in centimeters, corresponding to 2a. Received voltage is normalized such that the highest value is 1.

Figure 4 shows plots of received voltage (with the same normalization applied as in figure one) versus position for the same data runs as in figure 1. As expected, the distribution is effectively random, without any noticeable decrease in received signal strength as a result of increased distance from the transmitter, except in the case of 4b, where there is a slight decrease between the beginning and the end in terms of peak height. This corresponds to the Ricean-distributed sets, but this was not a consistent trend among the other such sets, which showed the expected random variance.

For the measurements taken with the transmitter located down a hallway with any line-of-sight component reduced to a non-specular component, neither of the two data runs showed a Rayleigh distribution, as was expected, and in fact, neither fit any of the tested pdfs very well, with the closest in each case being a Rayleigh distribution, with rms error of 0.51 in one case and 0.64 in the other, with the TWDP and Ricean pdfs being clearly distinguishable

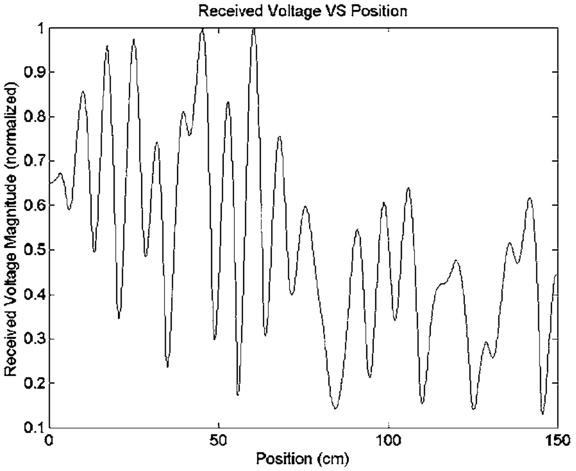

FIGURE 4B: Graph of a small-scale fading received envelope versus position in centimeters, corresponding to 2b. Received voltage is normalized such that the highest value is 1.

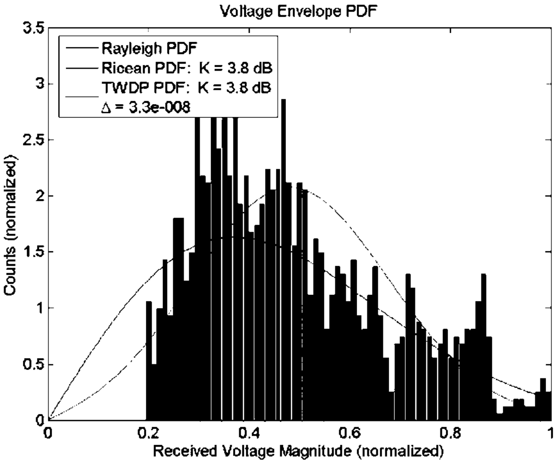

FIGURE 5A: Histogram of received voltage magnitude measured in a local area with overlaid pdf models. The received envelope is normalized such that the highest value is set to 1. Note that the Ricean and TWDP pdfs are not visually distinguishable.

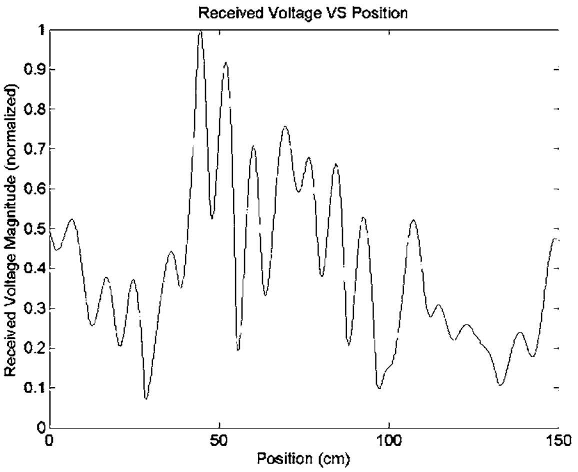

FIGURE 4C: Graph of a small-scale fading received envelope versus position in centimeters, corresponding to 2c. Received voltage is normalized such that the highest value is 1.

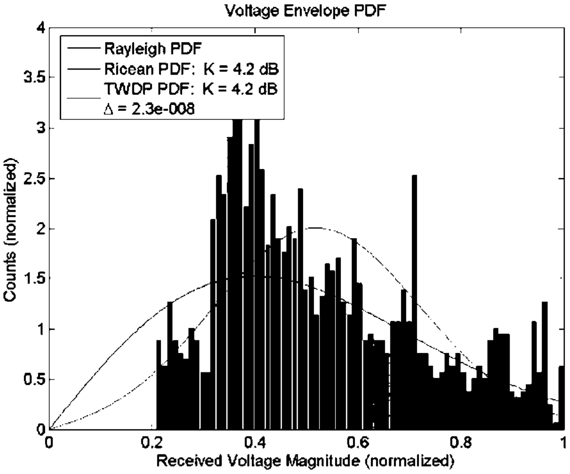

FIGURE 5B: Histogram of received voltage magnitude measured in a local area with overlaid pdf models. The received envelope is normalized such that the highest value is set to 1. Note that the Ricean and TWDP pdfs are not visually distinguishable.

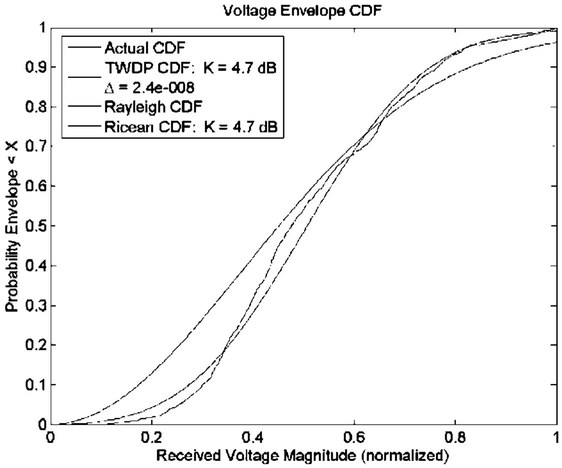

FIGURE 6A: Cdf for the data with cdfs of other fits overlaid, corresponding to the pdfs of figure 3a. The received envelope is normalized such that the highest value is set to 1. Note that the Ricean and TWDP pdfs are not visually distinguishable.

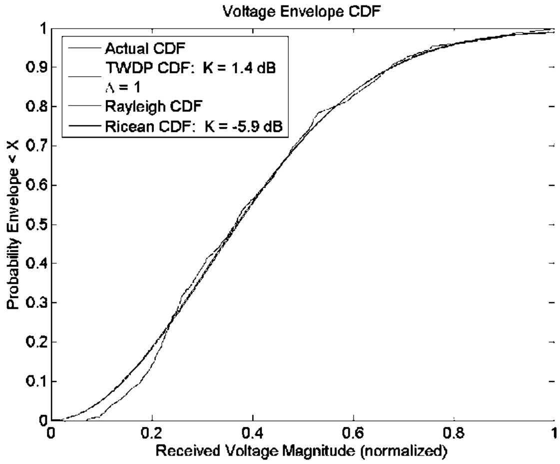

FIGURE 6B: Cdf for the data with cdfs of other fits overlaid, corresponding to the pdfs of figure 3c. The received envelope is normalized such that the highest value is set to 1. Note that the Ricean and TWDP pdfs are not visually distinguishable.

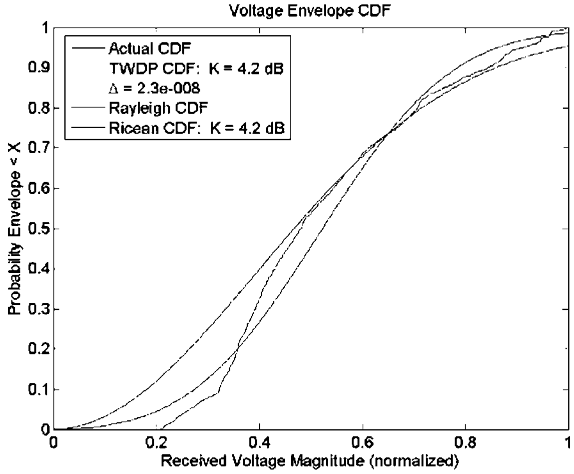

FIGURE 6C: Cdf for the data with cdfs of other fits overlaid, corresponding to the pdfs of figure 5b. The received envelope is normalized such that the highest value is set to 1. Note that the Ricean and TWDP cdfs are not visually distinguishable.

Trial #	Type	Rayleigh rms error	Ricean rms error	TWDP rms error
1	LOS	0.592	0.488	0.488
2	Through wall	0.461	0.355	0.355
3	Through wall	0.568	0.538	0.538
4	LOS	0.401	0.378	0.378
5	LOS	0.433	0.437	0.436
6	LOS	0.551	0.500	0.500
7	Down hall	0.506	0.554	0.554
8	Down hall	0.644	0.670	0.670

TABLE 1: Table showing the rms error for the fits of various pdfs for the different measurement trials. Note that rms error has units of normalized counts.

from the Rayleigh pdf in both cases. The histograms and overlaid pdfs for these graphs are seen in figure 5. It should be noted that due to the fact that the hallway in question was in use at the time of measurements, the channel was necessarily time-varying during the taking of this last group of measurements.

Cumulative distribution functions (cdfs) were also constructed using a Riemann summation, and in these how well a particular pdf fits is often clearer. A few of these are given in figure 6, corresponding to 3a, 3c, and 5b.

For all data runs, the TWDP fit was visually indistinguishable from the Ricean fit: Indeed, the value for Δ was always negligibly close to either zero or one: one in the case where the graph was most nearly Rayleigh distributed and zero otherwise. In addition, when the value for Δ was close to 0, the precise value obtained was sensitive to changes in the initial test points used for parameter estimation, though within the same order of magnitude. Furthermore, while many of the data sets failed to fit any of the traditionally used PDFs, in all cases less time was spent in the region of low signal strength than in the Rayleigh case.

Conclusions

Rayleigh or Ricean distributions may not always be adequate in describing small-scale fading for indoor propagation environments. When designing an indoor network, particularly if the transmitter and receiver(s) are located in an open area, one should be wary of this possibility. Particularly, it is highly recommended that any fading model which has fewer undesirable drops in signal strength than a Rayleigh model be used with extreme caution, particularly in the most common circumstances where the channel is time-varying, since it is a distinct possibility that the actual distribution will not fit these models particularly well, but the data shows that it is very unlikely that the actual distribution will have *more* such drops than it would under a Rayleigh model.

Furthermore, while TWDP fading may describe the most fading scenarios mathematically, in that it reduces to all other common distributions in different limiting cases [8], these tests show that an indoor fading environment can be described just as accurately by a Ricean distribution in most cases.

Also, the transparency of interior building walls may be high enough at around 2.4 GHz to allow a significant signal to pass through a single wall, which can be factored into making a wireless network serviceable with fewer terminals in an area with enclosed rooms. However, it should be noted that the results obtained in this respect were rather preliminary, and so further investigation is required.

Furthermore, the use of a linear positioner has, in this basic experiment, been shown to provide a means of mapping small-scale fading phenomena in the wireless channel to a fairly high level of precision in the GHz range. Further investigation in this direction may result in more detailed characterization of small-scale scattering and fading phenomena.

References

1. G. D. Durgin, *Space-Time Wireless Channels*. Upper Saddle River, NJ: Prentice Hall, 2003.
2. A. Fanimokun and J. Folik, "Effects of Natural Propagation Environments on the Wireless Sensor Network Coverage Area," *Proceedings of the 35th Southeastern Symposium on System Theory, 2003*, 16-18 March 2003.
3. J. Frolik, "A Case For Hyper-Rayleigh Fading Channels," *IEEE Transactions on Wireless Communications,* Vol. 6, no. 4, pp. 1235-1239, April 2007.
4. K. P. McCarthy and U. Wellens, "Measurements of 900 MHz Propagation for Microcellular Communications Systems Design," *8th European Conference on Electrotechnics, 1988. Conference Proceedings on Area Communication*, EUROCON 88, Stockholm, Sweden, 13-17 June 1988.
5. R. R. Murray, H. W. Arnold, and D. C. Cox, "815 MHz Radio Attenuation Measured Within A Commercial Building," *IEEE Transactions on Antennas and Propagation,* vol. 37, issue 10, pp. 1335-1339, Oct. 1989.
6. P. Nobles and F. Halsall, "Indoor Propagation at 17GHz and 60GHz – Measurements and Modeling," *IEE National Conference on Antennas and Propagation, 1999,* York, UK, 31 March-1 April 1999.
7. J. Sijbers, A. J. Den Dekker, D. Van Dyck, and E. Raman, "Estimation of Signal and Noise from Rician Distributed Data," *Proceedings of the International Conference on Signal Processing and Communications,* pp. 140-142, Gran Canaria, Canary Islands, Spain, 11-14 February 1998.
8. Gregory D. Durgin, Theodore S. Rappaport, and David A. de Wolf, "New Analytical Models and Probability Density Functions for Fading in Wireless Communication," *IEEE Transactions on Communications*, Vol. 50, No. 6, pp. 1005- 1015, June 2002.

Acknowledgments

This work was supported by the STC Program of the National Science Foundation No. DMR 0120967, and CHE 0453596.

ALEXANDER H. HENDERSON was born in Aiken, South Carolina on June 19, 1986. A current undergraduate at Furman University, Greenville, SC, he anticipates graduating in 2008 with a B. S. in Physics and Mathematics. After graduation, he intends to pursue a Ph.D. in Physics.

A member of the Society of Physics Students and Sigma Pi Sigma (a physics honors society), Mr. Henderson has previously done undergraduate research in the field of gravitation under Dr. William Baker at Furman University.

Electrical Stability of Carbon Nanotube Thin Films for Transparent Flexible Electrodes

RISHABH JAIN, University of Pennsylvania
Samuel Graham and Roderick Jackson, The George W. Woodruff School of Mechanical Engineering
Georgia Institute of Technology

Introduction

Single wall carbon nanotubes (SWNTs) are an interesting class of materials that can be developed for application in flexible electronic devices as the electrode (Figure 1). Present devices use Indium Tin Oxide (ITO) as the transparent electrode. While ITO can be manufactured with high levels of transparency in the visible range and good conductivity, it has variable electrical properties and the mechanical properties are not ideal. Additionally the cost of ITO has become an issue with the price of Indium expected to increase ten fold in the next 5 – 10 years. SWNT film electrodes provide a potential solution to these problems due to their reliance on a random percolation network to provide conductive pathways (Figure 2). Thin film electrodes composed of SWNTs provide conductivity values comparable to ITO deposited on polymer substrates. Typical films used in this study are about 80% transparent (Figure 3 and 4) and have sheet resistances on the order of 200 Ω/□ , values comparable to the best SWNTs currently published in literature.

When developing the SWNT films, it is necessary to chemically dope the films because only one third of the nanotubes are metallic, the rest are semi conducting. The metal-semiconductor contacts between nanotubes in the films introduce additional charge transport barriers which are lowered through doping. While doping of CNTs is seen as a necessary step, an understanding of the stability of the chemical doping is required for these films to be used in devices.

Organic devices can be either solution processed or vacuum processed. It is therefore important to test potential effects on stability in either case. In this report we will discuss the effects on stability of the films when exposed to various solvents that the devices will commonly be exposed to. Additionally, we will examine the effects of a vacuum environment on the stability.

Methods

In order to produce the films, a nanotube dispersion (P3 type, Carbon Solutions Inc.) in 0.5 wt% SDS solution is prepared. The nanotubes are functionalized by the company with carboxylic acid side groups through refluxing in nitric acid[7]. A fine dispersion of these nanotubes is achieved via bath sonication in the SDS solution. The solution is then centrifuged at 14,000 g for 60 minutes in order to separate single nanotubes from undesired bundles. The dispersion is carefully decanted and then vacuum filtered through a 0.1 µm GE filter. This process provides a thin film of SWNTs on the filter membrane. The film can then be transferred onto either glass or flexible substrate. In this study we are concerned with the properties of the SWNTs during use in flexible electronics. The films are therefore transferred to PET via dissolution of the filter in consecutive acetone baths.

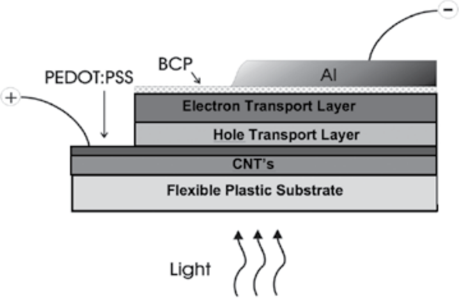

FIGURE 1. A typical setup for an organic photo voltaic device with carbon nanotubes (CNTs) as the electrode.

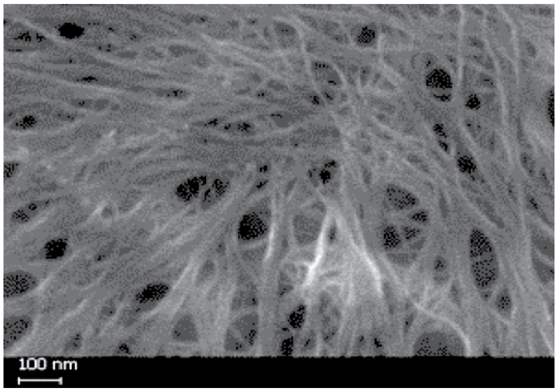

FIGURE 2. SEM image of carbon nanotube film showing random network structure

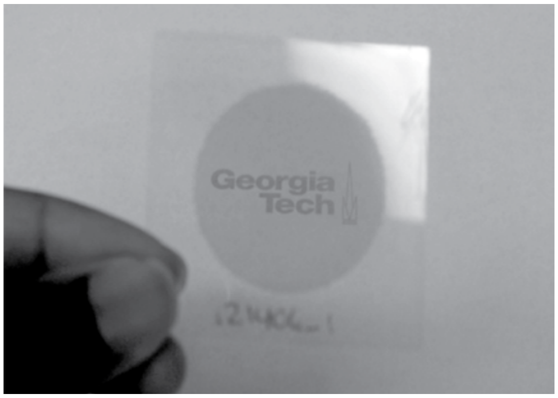

FIGURE 3. Digital photograph of SWNT film showing transparent nature of film

Chemical doping is carried out by dipping the films in a bath of thionyl chloride ($SOCl_2$, 97% reagent grade). This causes the carboxylic acid functional groups to get replaced by the acyl chloride group, which is more electronegative than the carboxylic acid group[9]. Once the film is removed from the dopant, it is dried with an air flow and then placed in a vacuum oven at 90°C for 3 hours. The film is put in the oven in order to get rid of haziness that appears on the film after the doping process. The electrical properties of the film are not affected by the heat. The heating process also ensures that doping does not cause a change in transmission.

Once the film is prepared, tests for stability are carried out with exposure to de-ionized water, methanol, and chloroform. The stability of a film not exposed to any solvent was also observed as a baseline for comparison. The solvents were chosen as they are commonly used in processing of devices. The film is exposed to one of these chemicals by dipping it in a bath of the respective chemical for 5 minutes. The film is then taken out of the chemical and dried in a gentle air flow and then stored either in air or a dry box. Resistance measurements were then taken at regular intervals of time up to 3 weeks so as to observe the effects of the solvent on the stability once removed from the same. Resistance was measured through 2 point measurements taken across the diameter of the film at equal distances each time using an Agilent 6 ½" digital multimeter. Changes in the 2 point measurement correspond directly to changes in the sheet resistance via a linear correlation. Sheet resistance measurements of representative films were taken using the transmission line method. Transmission of representative films was measured at 550 nm using a UV-Vis spectrophotometer.

Results

Films were typically 400 Ω/□ before chemical doping in $SOCl_2$ and reduced by a factor of two to obtain the 200 Ω/□ value. These values correspond to approximately 1.6 KΩ and 800 Ω in the 2 point measurements at a 1 3/8" separation of the multimeter probes. As a primary baseline, the stability of an undoped film kept in a dry box was tested. Films that were not doped essentially stayed the same resistance over the course of 3 weeks. It was also noticed that there was no difference between the films that were in the dry box as opposed to those in air. The undoped films were also exposed to the various chemicals in order to test their effect on the actual nanotubes. There was no change in resistance after exposure or over the course of three weeks, implying that the nanotubes themselves are stable and do not react with these chemicals.

Films were then doped in the $SOCl_2$ for 30 minutes, 3 hours and 14 hours. The stability of doped films kept in both air and in a dry box was tested first. There was no salient difference between the two methods of storage. However, it is important to note that the dry box did not provide a completely moisture free environment as films were exposed to air while measurements were taken. Also, there was no difference in stability based on the amount of time a film was doped for. Most importantly, there was an increase in resistance over time for all of the films with resistances going up between 30% and 50% in 3 weeks (Figure 5). It can be deduced that the increase in resistance is due to instability of the acyl chloride group formed during doping because the undoped film stayed mostly stable with only a slight increase toward the end of a week.

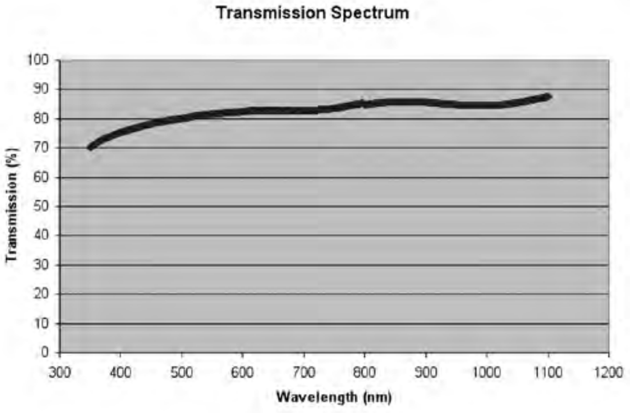

FIGURE 4. Transmission spectrum of the SWNT thin film showing an 81% transmission at 550 nm.

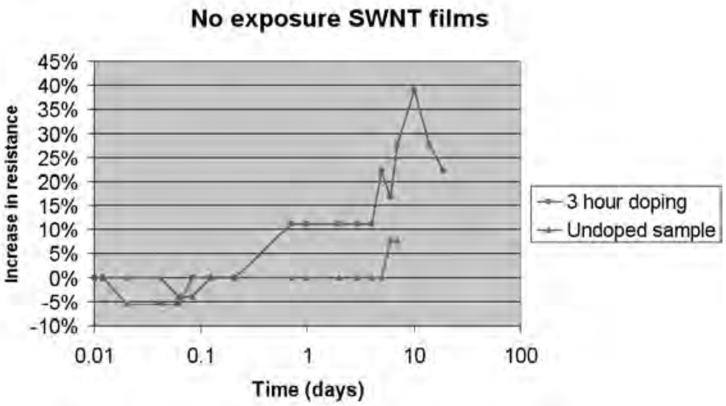

FIGURE 5. The 2 point resistances of films not exposed to any chemical, one doped for three hours and one undoped. The films were stored in air.

Doped films immersed in de-ionized water for 5 minutes tended to instantly increase the post doping resistance of the film by around 40% (Figure 6). The increase in resistance is due to the reaction of water with the acyl chloride groups. The water reacts with these side groups to give back the carboxylic acid side groups, thereby increasing the resistance of the film. It seems that after the initial increase in resistance, the stability follows the same trend as that of a film not immersed in water. Further, longer doping times and keeping film in dry box did not seem to have any salient effects on the stability of the films. With the undoped film being stable under exposure to water, this implies instability of the thionyl chloride doping procedure in itself.

Doped films immersed in chloroform for 5 minutes also increased the post doping resistance of the film by around 40% (Figure 7). After the initial increase, there is a steady increase in the resistance over time which is similar in trend to that of either no exposure or exposure to water. Further, there is no apparent effect on stability of either longer doping times or storage of film in dry box. When examined theoretically, the chloroform should not in fact increase the resistance of the film because a reaction between the carboxylic group and chloroform does not occur at room temperature. Experiments by Parekh et al. do indeed show stability of the film under exposure to the solvent[9]. The reason the film increased in resistance during these tests is that the chloroform was not pure. The solvent probably had traces of water and other reactive chemicals in it. This test therefore shows the sensitivity of the film to reactive solvents and illustrates the need to ensure purity of the solvent during device production.

Films that were immersed in methanol after doping increased the post doping resistance by around 30% (Figure 8). Again, doping time and storage method did not affect the stability of the film. What was of particular interest in this case was that after the film was dried in air and let to sit in either air or the dry box the resistance went down slightly and stayed around that value for the rest of the testing period of three weeks. This was due to the formation of the methyl ester side group from the reaction of the carboxylic acid group with the methanol. The methyl ester group is apparently more stable than the acyl chloride group though it does not give as low resistance values. At the same time, after the course of 3 weeks, the methyl ester functionalized nanotubes are actually more conductive than the doped films that were not exposed to a solvent.

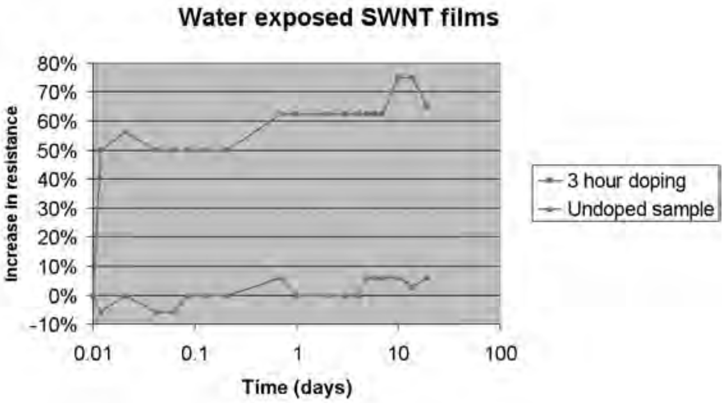

FIGURE 6. The 2 point resistances of films that were exposed to de-ionized water, one doped for three hours and the other undoped. The films were stored in air. The initial increase in resistance of the doped sample depicts the increase in resistance immediately after exposure to water.

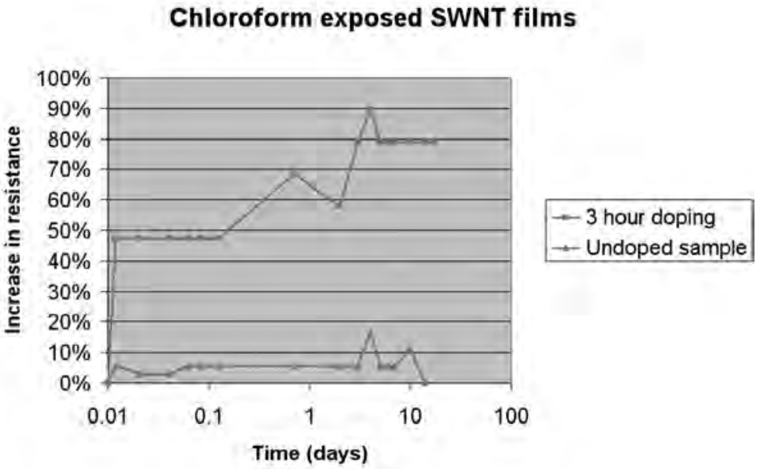

FIGURE 7. The 2 point resistances of films exposed to chloroform, one doped for 3 hours and one undoped. The films were stored in air. The initial increase in resistance of the doped sample depicts the resistance before and after exposure to chloroform.

The effect of introducing the films in a vacuum was studied by pumping the films down to a 10^{-8} torre vacuum in an E-Beam evaporator. The chamber was completely closed and opaque. Hence, in order to ensure that light did not have an effect on the conductivity of the film two controls were taken, one with films kept in air, exposed to light and the other with films kept in air enclosed in an opaque box. There was no difference in the trend for increase in resistance among any of the three scenarios (Figure 9). This implies that neither the vacuum nor a lack of light make a difference to the stability of the chemical doping. Additionally, the tests were carried out with the different doping times of 30 minutes, 3 hours and 14 hours. Here again the doping time did not affect the stability of the films.

Conclusions

We were able to produce transparent, conductive carbon nanotube thin films with transparencies equivalent to ITO, albeit higher sheet resistance values (approx. 200 Ω/□. as opposed to about 70-100 Ω/□ on PET). The films that were produced increased significantly in resistance when exposed to solvents commonly used in processing of devices and increased in resistance with time when stored in air. Only the methyl ester side group formed via exposure of doped films to methanol is stable with time. Additionally, it was noticed that doping time does not play a significant role in film stability. Also, films stored in either air or a dry box behave in the same manner with respect to electrical stability. Finally, neither the absence of light nor a vacuum environment affects the stability of the films in any manner.

This study raises the question of trying to find an alternative doping method. Some studies have already been published where other functional groups are used as the electron withdrawing source. Currently thionyl chloride is the most common chemical used to dope the films, hence it is necessary to fully understand the mechanism by which the chemical dopes the films so that a method to prevent the degradation of electrical properties can be developed. While other investigations of SWNT films are yet to be carried out, the material is a promising replacement for ITO in the near future.

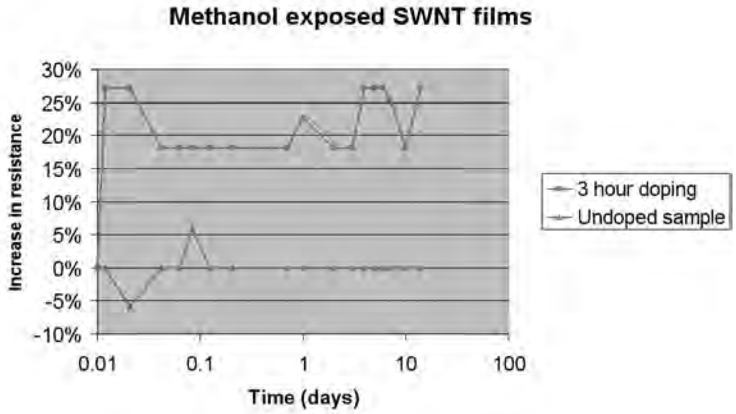

FIGURE 8. The 2 point resistances of films exposed to methanol, one doped for 3 hours and one undoped. The films were stored in air. The initial increase in resistance of the doped sample depicts the resistance before and after exposure to methanol.

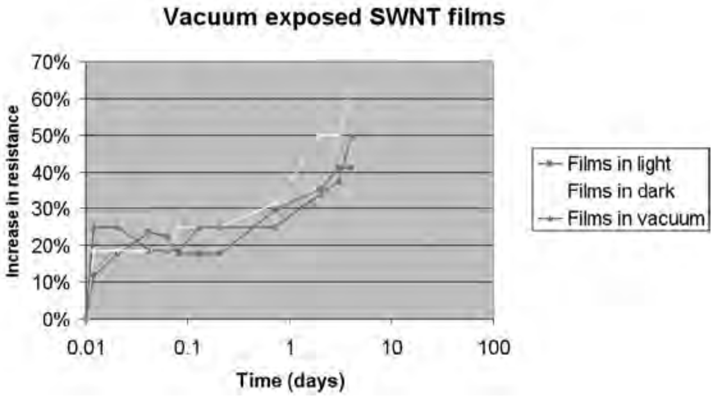

FIGURE 9. The 2 point resistances of films doped for three hours, one kept in light, one kept in dark and one in vacuum at 10^{-8} torre. The films were then stored in air. The initial increase in resistance of the doped sample depicts the resistance before and after exposure to methanol.

References

1. Gruner, G. *J. Mater. Chem.*, 2006, 16, 3533-3539
2. Sigma-Aldrich Company http://www.sigmaaldrich.com/catalog/search/ProductDetail/ALDRICH/636924
3. Peter Harrop, “Poor Adoption of ITO Replacements – Why?” IDTechEx, Printed Electronics World, 9 July 2007.
4. Gruner, G.; Hu, L.; Hecht, S. *Nano Lett.,* 2004, Vol. 4, No. 12
5. L. Hu, D.S. Hecht, and G. Gruner, Nano Lett. 4, 2513 (2004).
6. H. E. Unalan, G. Fanchini, A. Kanwal, A. Du Pasquier, and M. Chhowalla, Nano Lett. 6, 677 (2006).
7. See website : www.carbonsolution.com
8. Z. Wu, Z. Chen, X. Du, J. M. Logan, J. Sippel, M. Nikolou, K. Kamaras, J. R. Reynolds, D. B. Tanner, A. F. Hebard, and A. G. Rinzler, Science 305, 1273 _2004_.
9. Parekh B.B.; Fanchini G.; Eda G.; Chhowalla M. *Appl. Phys. Lett,.* 2007, 90, 12193
10. Shabbir A Basha,“Study of Indium Tin Oxide (ITO) for Novel Optoelectronic Devices,” Ph. D. thesis, King’s College London, University of London, London, U.K. 1997.

Acknowledgements

A special thanks to the following people:

— Dr. Samuel Graham, Roderick Jackson, Thomas Beechem and Robert Cross, the George W. Woodruff school of Mechanical engineering at the Georgia Institute of Technology,

— Andres Haldi and Kippelen group, School of Electrical and Computer Engineering at the Georgia Institute of Technology

— Dr. Simon Jones, Dr. Steve Barlow and Dr. Seth Marder, Marder group, School of Chemistry and Biochemistry at the Georgia Institute of Technology

This work is based upon the support provided by the STC Program of the National Science Foundation No. DMR 0120967, and CHE 0453596.

RISHABH JAIN is currently an undergraduate in the Fisher Program in Management and Technology at the University of Pennsylvania. He is pursuing a BSE in Materials Science and Engineering and a BSc in Economics with a concentration in Finance. He plans to attend graduate school in Materials Science and Engineering to pursue a PhD.

Quasi-living Synthesis of Semiconducting Polymers

NOËL M. LEWIS, University of Dallas
Christine K. Luscombe, University of Washington

Introduction

Scientists have taken an interest to organic semiconducting polymers (OSPs) and their applications ever since their discovery in the late 1970s. In more recent years, conducting polythiophenes have shown promising prospects for use in economical all-polymer transistors, nanooptical and nanoelectronic materials, and highly conductive plastics.[1] However, scientists oftentimes have little control over the production of OSPs due to the complex mechanism of formation. OSPs are usually made by polycondensation reactions which typically eliminate small molecules during synthesis. Furthermore, the step-wise nature of the reaction contributes to the slow rate of attaining a high molecular weight. Because of both the elimination and the step-wise mechanism, homogeneous polymers formed by polycondensation reactions tend to be difficult to attain. If OSPs could be synthesized in a quasi-living manner, then the reactive site could be kept intact. Additionally, there would be improved control over the morphology and property of the polymer thin films, which would help to improve the performance of electronic devices. Starting with fluorene, we have been working to improve the process of synthesizing OSPs in a controlled manner. Because changes in molecular structure inevitably affect the visible and functional properties of the material, a controlled chain-growth polymerization would allow for the opportunity to influence the creation of new materials.

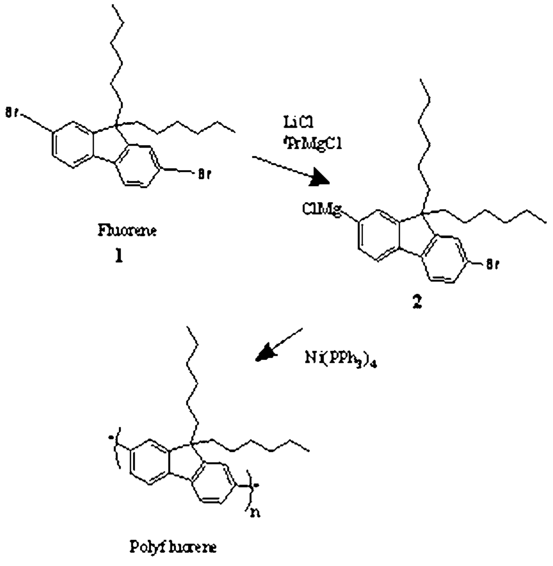

SCHEME 1. Synthesis of polyfluorene using a Kumada coupling procedure.

A recent study successfully synthesized poly(p-phenylene) by a chain-growth reaction.[2] As indicated by Scheme 1, the same procedure was used in an attempt to synthesize polyfluorene. The reaction was carried out in a three-necked round bottomed flask with one end connected to a stream of N_2 to avoid oxidation.

To test the reactivity of the monomer, a Kumada coupling reaction was performed as shown by Scheme 2.

In hopes that a derivative of **1** would prove more reactive, 9,9-dihexyl-2,7-diiodo-fluorene was synthesized as shown in Scheme 3.

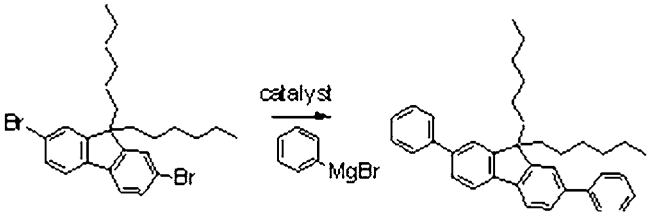

SCHEME 2. Kumada coupling reaction.

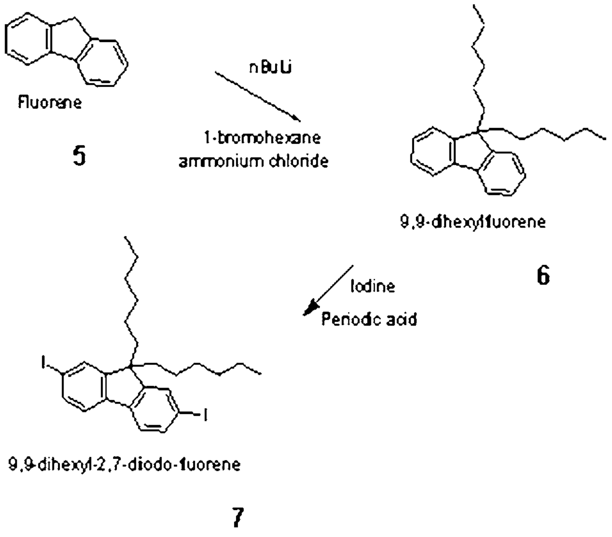

SCHEME 3. Synthesis of 9,9-dihexyl-2,7-diiodo-fluorene.

Experimental

Polymerization of polyfluorene (3).[2] LiCl (42 mg, 1 mmol) was placed in the flask and heated with a heat gun while in the N_2 atmosphere. Fluorene (0.49 g, 1 mmol) dissolved in THF (5 mL) was added via syringe. Isopropylmagnesium chloride (0.5 mL, 2M in THF) was then added, also via syringe. The mixture was stirred on an ice bath for 1 h and continued stirring at room temperature overnight. Once the Grignard-like reagent (**2**) was formed, $Ni(PPh_3)_4$ plus THF (5 mL) was added to the mixture and stirred overnight at room temperature. HCl (1 mL, 14 M) was added to quench the reaction. The product was dissolved in chloroform and then precipitated with methanol. The solvent was removed under reduced pressure.

Kumada coupling reaction to form (4). Fluorene (**1**) (0.1 g, 0.20 mmol), catalyst (10 mol %), and THF (3 mL) was placed in a three-necked round bottomed flask which was put under N_2. Phenyl-magnesium bromide (0.44 mL, 1 M) was added via syringe and the mixture was refluxed overnight at 70 °C. The catalysts used were $NidppCl_2$, $Ni(PPh_3)_4$, and $Pd(PPh_3)_4$.

Synthesis of 9,9-dihexylfluorene (6).[3] Bu^nLi (6.4 mL, 2.5 M) was added to a solution of **5** (1.07 g) in THF (53 mL) at -78 °C over a period of 5 min. The solution was then stirred for 1 h at -60 °C. 1-bromohexane (3.17 g, 19.2 mmol) in THF (11 mL) was added dropwise, and the solution was stirred for 20 min. at -60 °C. Ammonium chloride (5.3 g) in H_2O (32 mL) was added and the organic layer was removed and dried with anhydrous $MgSO_{4.}$ The remaining solvent was removed under reduced pressure, and the product was purified by column chromatography using hexane as the eluent.

Synthesis of 9,9-dihexyl-2,7-diiodofluor-ene (7). Compound **6** (2 g, 5.98 mmol) was placed in a round-bottomed flask. 10 mL of solvent consisting of CH_3COOH: H_2O: H_2SO_4 (100:20:3) was added and heated to 65°C. Periodic acid (0.46 g, 2 mmol) and iodine (1.02 g, 4 mmol) were added and the mixture was stirred for 4 h. The mixture was then cooled to room temperature and H_2O (150 mL) was added. The organic layer was extracted with ether and washed with H_2O, 2M aqueous sodium bicarbonate, 5% aqueous $Na_2S_2O_3$, and saturated NaCl solution. Any remaining solvent was then removed under reduced pressure. The resulting 9,9-dihexyl-2,7-diiodofluorene was recrystalized from ethanol.

Results and Discussion

The product from the first attempt at synthesizing polyfluorene was unsuccessful. The product underwent analysis by GPC, but the results did not indicate the presence of a polymer. The outcome suggests that the extent of reaction was not high enough to lend a significant degree of polymerization.

Products from the Kumada coupling reactions were analyzed by GC/MS. The $Ni(PPh_3)_4$ catalyst gave a small amount of double substitution as indicated by the peak at 34.7 min. with a MW of 486 **(fig. 1)**. The $NidppCl_2$ catalyst showed significantly more double substitution with the compound of MW 486 having a retention time of 34.76 min **(fig. 2)**. The results for the $Pd(PPh_3)_4$ catalyst only showed starting material of MW 492 with a retention time of 22.995 min. The results from the GC/MS suggest that the $NidpppCl_2$ catalyst was most successful at allowing fluorene to undergo a Kumada coupling reaction.

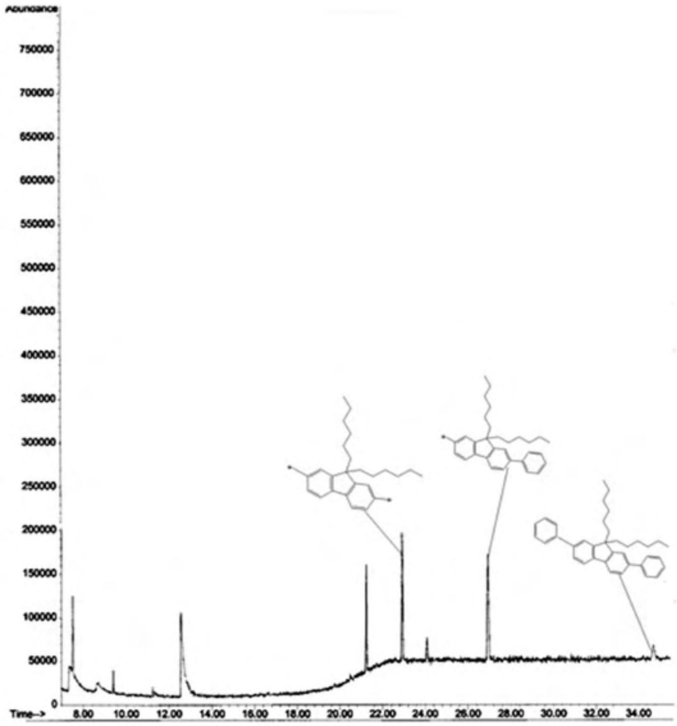

FIGURE 1. GC of product from Kumada reaction using $Ni(PPh_3)_{4.}$

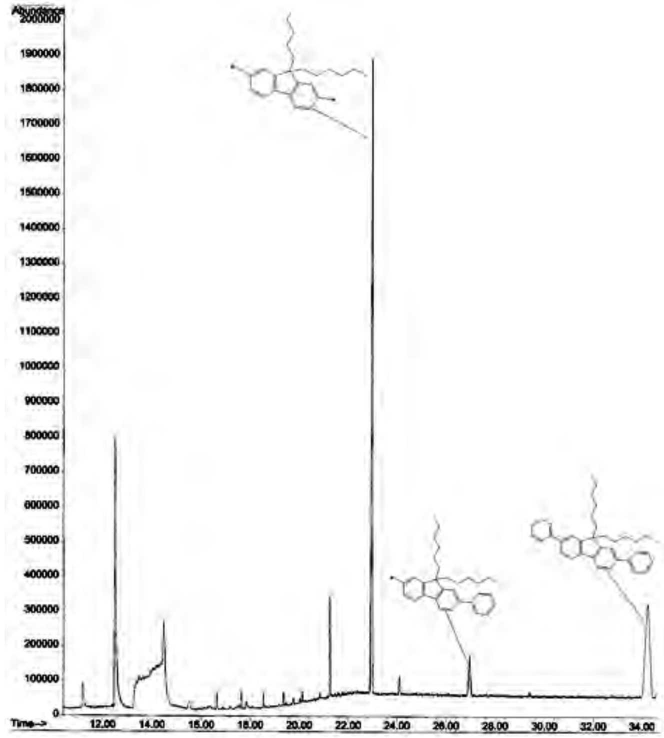

FIGURE 2. GC of product from Kumada reaction using $NidpppCl_{2.}$

When **7** was reacted with NidpppCl$_2$ as the catalyst, the resulting product had no starting material (**fig. 3**). The double substitution was indicated by a peak at 34.3 min. with a MW of 486. The success of the reaction implies that polymerization is possible with 9,9-dihexyl-2,7-diiodofluorene.

Conclusions

Fluorene and its derivative show the ability to react in a Kumada reaction which implies that it has the potential to react in a quasi-living manner. If this ability could be extended to a polymerization, the morphology and property of a polymer thin film could be controlled. Increased control over the molecular structure would allow for the creation of new materials as well as the advancement of polymer use in electronic devices.

References

1. R.D.McCullough "The Chemistry of Conducting Polythiophenes" *Adv. Mater.* 1998, 10, 93.
2. R. Miyakoshi, K. Shimono, A. Yokoyama, T. Yokozawa, "Catalyst-Transfer Polycondensation for the Synthesis of Poly(p-phen-ylene) with Controlled Molecular Weight and Low Polydispersity" *J. Am. Chem. Soc.*, 2006, 128(50), 16012-6013.
3. Barbara Tsuie, Jerry L. Reddinger, Gregory A. Sotzing, Jadwiga Soloducho, Alan R. Katritzky, John R. Reynolds, "Electroactive and Luminescent Polymers: New Fluorene-heterocycle-based Hybrids" *J. Mater. Chem.,* 1999, 9, 2189-2200.

Acknowledgments

Funds for this research were provided by the Center on Materials and Devices for Information Technology Research (CMDITR), and the NSF Science and Technology Center No. DMR 0120967. The author thanks Christine K. Luscombe for overseeing her project, Anh Ho for his help in lab, all those at the University of Washington who made the CMDITR-STC REU program possible.

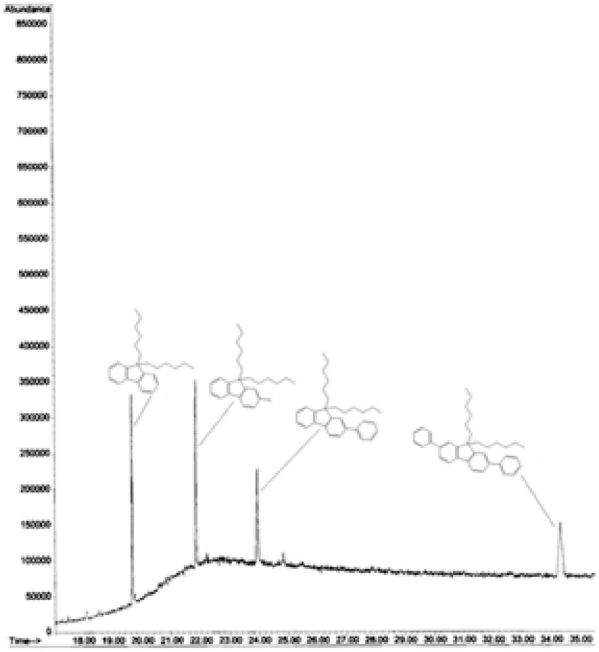

FIGURE 3. GC of product from Kumada reaction using NidpppCl$_2$ and 7.

NOËL M. LEWIS Noël is a Junior at the University of Dallas where she is receiving her B.S. in Chemistry. She plans to continue in a science-related field after graduation.

Synthesis and Characterization of Oligoacenes for Organic Electronics and Optoelectronics

LINDSAY LUCAS, Wagner College
Eilaf Ahmed, Alejandro L. Briseno, Samson A. Jenekhe, University of Washington

Introduction

In recent years, interest in the development of organic semiconductors for application in thin film organic field-effect transistors (OFETs) has risen steadily due to the promise of a less expensive, flexible, and higher performance alternative to inorganic semiconductors.[1] Although charge carrier mobility values in thin film transistors are now comparable to amorphous silicon, they suffer from air stability. For example, the high-performance benchmark semiconductor pentacene is highly susceptible to degradation in air and must be vacuumed sublimed.[2] This issue is one of several challenges facing researchers in the field of organic electronics.

Currently, two different types of organic semiconductors are being investigated: n-channel transistor materials, organic semiconductors that exhibit electron transport and p-channel transistor materials, organic semiconductors that exhibit hole transport. P-channel materials boast higher charge mobility values than n-channel materials, but research on both materials is still underway.[3]

Scientists have been actively pursuing the field of organic electronics since the 1980s in efforts to produce methods that improve charge carrier mobility and stability in organic semiconductors. One widely studied method is the addition of substituents on conjugated oligoacenes, such as pentacene and tetracene. One of the major advantages of organic semiconductors is synthetic flexibility. For example, halogenation of oligoacenes can convert the otherwise p-channel materials to n-channel materials.[4] In earlier research, nitrogen and sulfur, when used as bulky substituents in oligoacenes, demonstrated the capacity to increase stability without disrupting intermolecular forces inherent to large aromatic molecules.[5,6,7] Stability in an organic semiconductor is a property that may help achieve higher charge mobility values than previously reported.[6] This addition of substituents has also allowed many oligoacenes to ϖ-stack, further increasing the charge mobilities of oligoacene semiconductors in thin film field-effect transistors.[2] In this study, oligoacene-based 1,2,3,4-tetrachloro-benzo(b)phenazine (1), 5,12-dihydro-quinoxalino[2,3-*b*]phenazine (2), and dithia–cyclopenta[fg]napthacene (3) and napthaceno[5,6-c,d]-1,2 dithiole (tetracyanoquinodi-methane) (4) were synthesized as candidates for high-charge mobility organic semiconductors.

Results and Discussion

1,2,3,4-Tetrachloro-benzo(b)phenazine (Scheme 1) was synthesized by a condensation reaction of 2,3-diaminonapthalene and tetrachloro-1,2-benzoquinone in chloroform under nitrogen. Column flash chromatography was used to purify the compound and the product was characterized by Gas Chromatography-Mass Spectrometry (GC-MS) and Proton Nuclear Magnetic Resonance (1H NMR). Ultraviolet- Visible Spectrophotometry /Photoluminescence (UV/PL) displayed an absorption maximum at 522 nm and an emission maximum at 607 nm with orange emission (Figure 1).

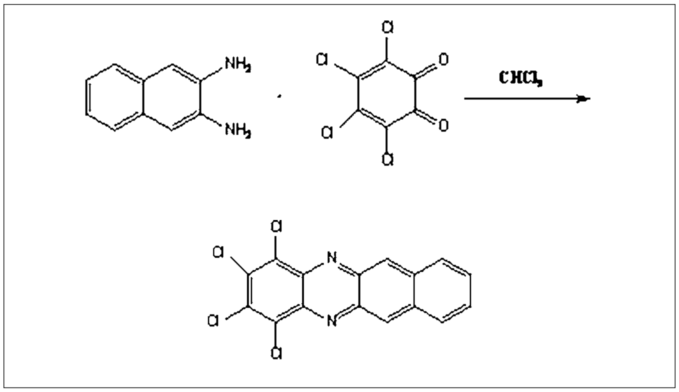

SCHEME 1. Synthesis of 1,2,3,4-Tetrachloro-benzo(b)phenazine.

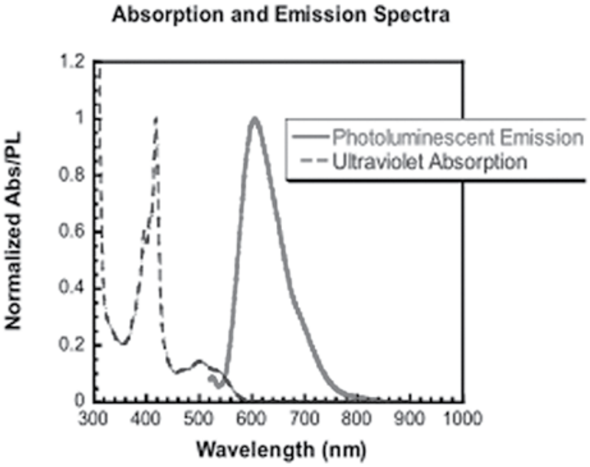

FIGURE 1. The UV/PL for 1,2,3,4-tetrachloro-benzo(b)phenazine displayed an absorption maximum at 522 nm and an emission maximum at 607 nm which corresponded to the orange fluorescence the product emitted

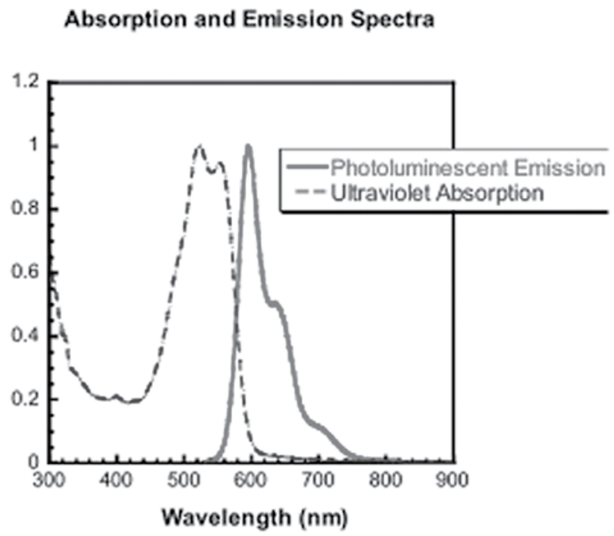

FIGURE 2. The UV/PL for 5,12-dihydroquinoxalino[2,3-*b*]phenazine displayed an absorption maximum at 420 nm and an emission maximum at 595 nm which corresponded to the orange fluorescence the product emitted.

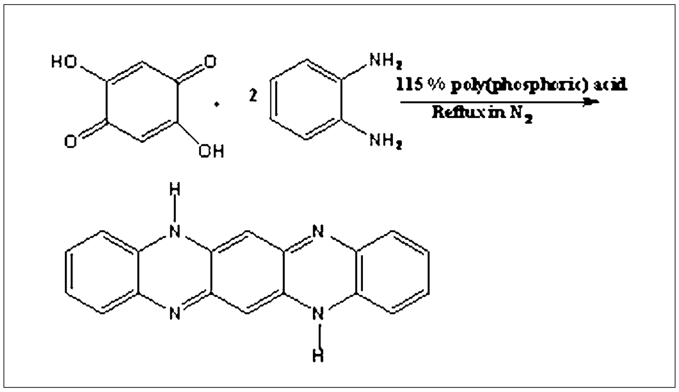

SCHEME 2. Synthesis of 5,12-dihydroquinoxalino[2,3-b]phenazine.

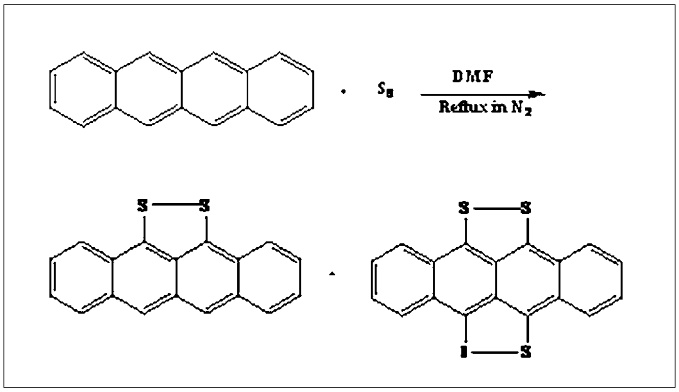

SCHEME 3. Synthesis of dithiatetracene (DTT) and tetrathiatetracene (TTT).

Due to its chloro- and nitro-substituents, this molecule is a potential candidate for an effective organic semiconductor. OFETs will be fabricated to determine the functionality of this molecule as a p-channel or an n-channel organic semiconductor.

5,12-Dihydroquinoxalino[2,3-*b*]phenazine (Scheme 2) had previously been synthesized but has never been fully explored as an organic semiconductor in OFETs.8 O-Phenylenediamine dihydrochloride and 2,5-dihydroxy-p-benzoquinone were used as reactants with 115 % poly(phosphoric) acid in nitrogen reflux. The reaction mixture was then washed with water and then acetone in a soxhlet and finally dried in vacuo at room temperature. The resulting product was characterized by GC-MS and its solubility and appearance in methanesulfonic acid and pyridine were compared with previous literature. UV/PL displayed an absorption maximum at 420 nm and an emission maximum at 595 nm corresponding to its orange emission (Figure (2)). The ability to ϖ-stack and its greater stability in air due to its nitrogen substituents make this molecule a candidate for use in OFETs. From its molecular structure, it appears that it has potential as a p-type semiconductor.8 OFETs will thus be fabricated to test the intrinsic charge transport properties.

Dithiatetracene (DTT) and tetrathiatetracene (TTT) (Scheme 3) were synthesized, according to literature methods[9,10,] in a substitution reaction using tetracene and excess sulfur in dimethylformamide. Although these two products have yet to be separated, their GC- MS characterization showed a lack of impurities in the product compound. Because of the sulfur substituents, these molecules should potentially display air stability and may demonstrate the ability to ϖ-stack as well.[9] After separation, these two molecules will be measured for their ability to function as semiconductors in OFETs.

Conclusions

In this study, novel molecule **1** and compounds **2**, **3**, and **4** were synthesized. **1** and **2** were obtained by condensation and **3** and **4** by a substitution reaction. These molecules were characterized by GC-MS and ^{1}H NMR and their optical properties were explored by UV/PL. Furthermore, an effort is currently underway to explore **1**, **2**, **3**, and **4** as semiconductors in field effect transistors.

Acknowledgments

The author gratefully acknowledges Eilaf Ahmed, Chemistry Department, University of Washington, for her constant support and mentorship, Alex Briseno, Chemistry Department, University of Washington, for his patience and time, Professor Samson A. Jenekhe, Chemistry and Chemical Engineering Departments, University of Washington, for the opportunity to become a part of his research group, Dr. Sara Selfe for her academic and intellectual discussions, and Jaclyn Yetter for her hard work and organization. This research was supported by NSF STC-MDITR and NSF (CTS-0437912).

References

1. Murphy, A.; Frechet, J. M. J. *Chem. Rev.* 2007, 107, 1066-1096.
2. Zaumseil, J.; Sirringhaus, H. *Chem. Rev.* 2007, 107, 1296-1323.
3. Newman, C.; Frisbie, C.; da Silva Filho, D.; Bredas, J. L.; Ewbank, P.; Mann, K. *Chem. Mater.* 2004, 16, 4436-4451.
4. Sakamoto, Y.; Suzuki, T.; Kobayashi, M.; Gao, Y.; Fukai, Y.; Inoue, Y.; Sato, F.; Tokito, S. J. *Am. Chem. Soc.* 2004, 126, 8138-8140.
5. Ma, J.; Sun, Y.; Liu, Y.; Chen, S.; Sun, X.; Qui, W.; Yu, G.; Cui, G.; Hu, W.; Zhu, D., J. *Mater. Chem.* 2005, 15, 4894-4898.
6. Bendikov, M.; Wudl, F.; Perepichka, D. *Chem. Rev.* 2004, 104(11), A-BC.
7. Anthony, J. *Chem. Rev.* 2006, 106, 123
8. Jenekhe, S. A. *Macromolecules*. 1991, 24, 1
9. Goodings, E.P.; Mitchard, D.A.; Owen, G. J. *Chem. Soc.* 1971, 1, 1310-1314.
10. Nigrey, P.; Garlto, A. J. *Chem. and Eng. Data.* 1978, 23, 2.

LINDSAY LUCAS is planning on attending the University of Washington or the University of Colorado-Boulder to earn a Ph.D. in Physical Chemistry or Chemical Engineering.

Synthesis of Organic Semiconductor with Compatible Solubility with Ion-Pair Monomers

KYLE E. LYNCH-KLARUP, Grinnell College
Meghana Rawal, Dr. Glenn P. Bartholomew, University of Washington

Introduction

Organic semiconductors are quickly gaining interest in the academic, commercial, and governmental sectors because of their advantages over their inorganic counterparts. Because they are quicker, easier, and cheaper to manufacture than the silicon based variety, organic semiconductors are rapidly developing into a major industry. One forecast predicts that by 2025 the industry will be worth $250 billion[1].

One device of considerable interest for low-cost, short-term, or point-of sale applications is the self-assembling, light-emitting electrochemical cell (LEC), which may be manufactured entirely with a roll-to-roll process2. Such LECs use a solution of an emissive polymer (the semiconductor) and a salt which work together to form a *p-i-n* junction when an electrical current runs through the device. The polymer and the salt are not naturally phase soluble, so a third molecule, such as poly(ethane oxide) (PEO) must be used to keep them in phase within solution. The necessity for the PEO is unavoidable as long as the emissive polymer and salts phase separate in solution.

If the emissive polymer could be made to be soluble with the salt, the improved compatibility would make the transition of electrons along the polymer more straightforward and efficient. The ions from the salt would move closer to the electrons and holes in the *n* and p respective portions of the polymer, allowing a larger number of electrons to be freed to move through the i portion of the LEC. This would lead to greater efficiency of the device and simplified manufacturing of LECs without PEO.

To remove the PEO from the device, emissive polymer would have to mimic the effects PEO has on the polymer and salt while retaining its abilities as a semiconductor. Previous work done by Meghana Rawal of the Bartholomew group successfully synthesized poly{1-methoxy-4-[2-[2-(2-methoxyethoxy) ethoxy]ethoxy]-5-methyl-2 vinylbenzene} (polymer 1). This is a poly(*p*-phenylene vinylene), PPV, strand with an oligo-ether chain directly attached to every benzene ring on its backbone. (see fig. 1)

Testing showed that though the polymer successfully remained a semiconductor, it was insoluble in all attempted solvents. Possible explanations for its insolubility are its high molecular weight and the oligo-ether chains interweaving, creating tangles of multiple strands of polymer, thus rendering it insoluble.

In an attempt to make polymer 1 soluble, variations are being synthesized and tested with the purpose of correcting one or both of the proposed reasons for the original polymers insolubility. The first variation poly{1,4-[2-[2-(2-methoxyethoxy) ethoxy]ethoxy]-5-methyl-2-vinylbenzene} (polymer 2) replaces the methoxy group with another oligo-ether chain, to see if the added solubility traits of two oligo-ether chains can overcome the believed resistance from the high molecular weight. (see fig. 2)

The second variation (polymer 3) places a carboxylic acid group in between the oligo-ether chains and the benzene ring in the hopes of making the molecule even more soluble than polymer 2. Another variation in polymer 3 is interspersing the esterified benzene molecules with unsubstituted benzene rings to spread the oligo-ether chains out and reduce the chance of them entangling and/or clumping. (see fig. 3)

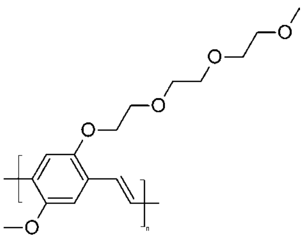

(1)

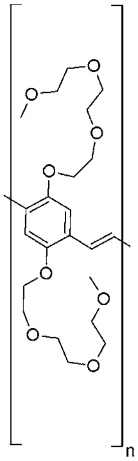

(2)

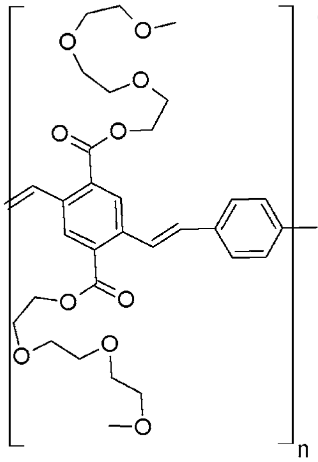

(3)

FIGURE 1. Previously created insoluble polymer with an oligo-ether attachment on the backbone.

FIGURE 2. Proposed modification of polymer 1 that would go into solution because of two oligo-ether chains.

FIGURE 3. Another proposed modification to polymer 1. It would include two carboxylic acid groups, two oligo-ether chains, and alternating unsubstituted benzene rings.

Results and Discussion

To create polymer 2, methyltriglycol (MTG) was brominated under argon at 0˚C and then attached to hydroquinone at positions 1 and 4 in DMF under argon. Chloromethane was then attached at position 2 and 5 under normal atmospheric conditions at 56˚C. Finally, the molecule was polymerized with itself in the presence of KOtBu and p-dioxane. (see scheme 1)

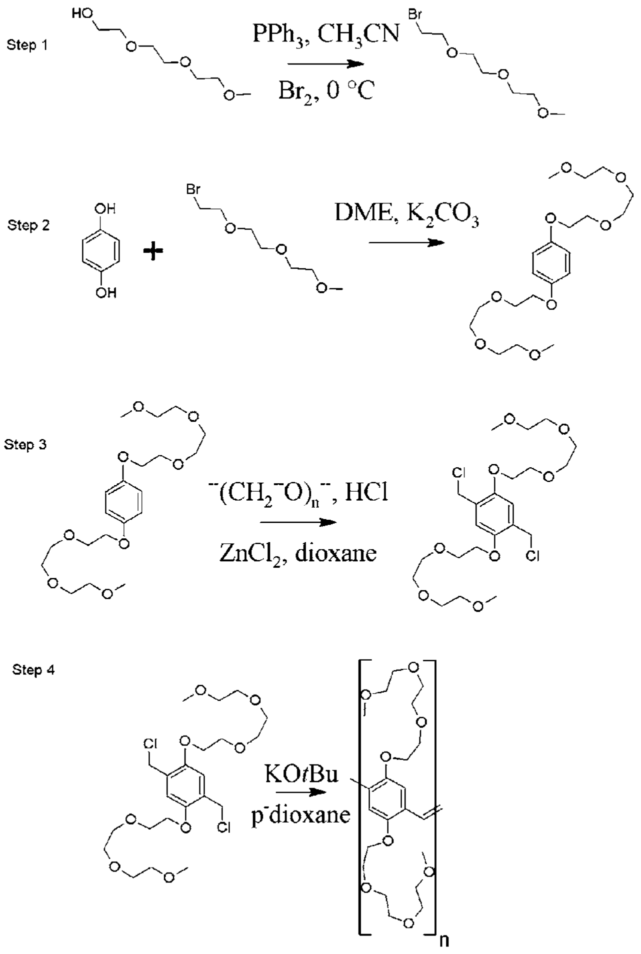

SCHEME 1. Synthesis of Polymer 2.

The polymer was slightly soluble in dimethylformamide (DMF) and cholobenzene, but did not produce a thick enough solution for spin-coating. However, the polymer did go into 1,2-dichloroethane.

Polymer 3 was made in two parts that were then polymerized together in the final step. Part 1 consisted of the unsubstituted benzene ring. To create this, a benzene ring with chloromethane groups at positions 1 and 4 was refluxed in DMF with PPh_3 to create [1,4-phenylenebis (methylene)] diphosphonium dichloride. NaOH, $H_2$0, and formalin were then reacted with this product at normal atmospheric conditions to produce divenylbenzene. (see scheme 2)

Part 2 was started with 1,4-dimethyl, 2,5-dibromo benzene, which was then reacted with $KMn0_4$ in pyridine and $H_2$0 at 99˚C to create 2,5-dibromoterephthalic acid. The product was than refluxed with MTG to make 1,4-[2-(methoxymethoxy) ethoxy]propyl 2,5-dibromobenzoate. (see scheme 3)

The two intermediate steps still need to be polymerized together and tested for solubility. (see scheme 4)

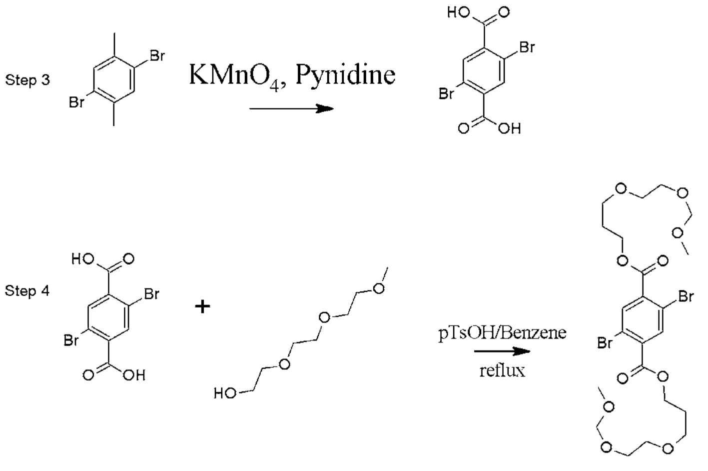

SCHEME 2. Synthesis of Part 1 of Polymer 3

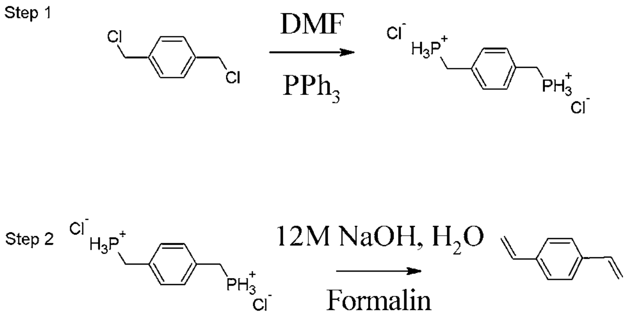

SCHEME 3. Synthesis of Part 2 of Polymer 3

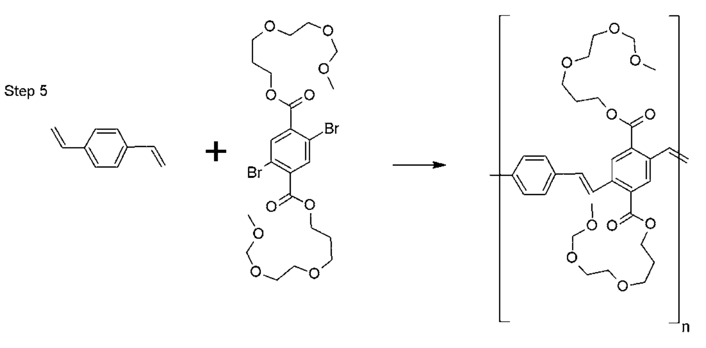

SCHEME 4. Combination of Parts 1 and 2 of Polymer 3

Conclusions

Polymer 2's only slight solubility in DMF and cholobenzene at first suggested that oligo-ether chains alone were not enough to overcome the intrinsic insolubility of MTG-PPV polymers. However, its solubility in 1,2-dichloroethane shows promise that it may work in devices. Additional tests are planned to optimize the polymer and place it into a device.

Polymer 3 has potential because of its unique variations. Unfortunately, polymerization has not been achieved yet. If soluble, the polymer will undergo further testing in an LEC.

Organic semi-conductors surpass silicon based semi-conductors in both cost of manufacturing and ease of processability. But, they have a long way to go to reach the inorganic versions effectiveness, needing to achieve both a level of stability and a level of efficiency hereto unfound. By making the emissive polymer soluble with the ion-pair monomers, the ions should lie closer to the polymer in its *p-i-n* state, giving it greater efficiency. Achieving this moves organic semiconductors one step further to being a marketable product.

References

1. P. Harrop, R. Das, *Organic Electronics Forecasts, Players, and Opportunities,* Far Field House, Cambridge, UK 2006.
2. J. M. Leger, D. B. Rodovsky, G. P. Bartholomew, *Adv. Mats.* 2006, 18, 3130.

Acknowledgements

Dr. Glenn Bartholomew, Professor of Chemistry at the University of Washington

The Bartholomew research group

Funding provided by the National Science Foundation through the Center on Materials and Devices for Information Technology Research (CMDITR) grant number DMR-0120967 and Hooked on Photonics grant number CHE-0453596

KYLE LYNCH-KLARUP has completed his freshman year at Grinnell College and is a proposed physics/religious studies double major. He currently plans on continuing his academic learning and completing a Ph.D. in physics.

Effects of Octadecanethiol on CdSe Quantum Dot Photoluminescence

MEGAN E. LYDON, California Polytechnic University, San Luis Obispo
Andrea M. Munro, David Ginger, University of Washington

Quantum dots are semiconductor nanocrystals with high photoluminescence efficiencies and narrow, size-tunable photoluminescence. They are promising candidates for use in applications such as light-emitting diodes, solar cells, and biological markers. Due to their small size, quantum dots have a high surface-to-volume ratio, and their properties are sensitive to their surface chemistry. Understanding how specific ligands bind to quantum dots surfaces is important to tailor the properties of quantum dots for individual applications. We study ligand binding to CdSe quantum dots by measuring changes in the photoluminescence intensity and lifetime of the quantum dots as a function of octadecanethiol concentration in solution. We will fit the thiol titration data to a model by Tachiya[1], in order to determine the thiol adsorption binding constant and the average number of binding sites per quantum dot.

Introduction

Quantum dots are small crystals with as many as half of their atoms on their surface, causing their surface chemistry to be very important. We study the effects of binding 1-octadecanethiol (ODT) to CdSe quantum dots. Previous studies on the effects of ligands on CdSe quantum dot photoluminescence indicate that thiol quenching is not well described with a simple Langmuir isotherm[2]. In order to better model thiol binding, we have collected titration data in order to test a quenching model developed by Tachiya[1].

$$K_a = \frac{k_+}{k_-} \quad (1)$$

The Tachiya model was designed to describe the quenching of fluorophores within micelles as a function of quencher concentration for quenchers that enter and exit the micelles with rates of k_+ and k_-, respectively. The total quencher concentration for the system is [Q], with a micelle concentration of [M]. The model takes into account the maximum number of quenchers per micelle, m, the photoluminescence decay rate of the fluorophore in absence of the quencher, k_0, and the quenching rate of the quencher, k_q. To adapt this model for quantum dots, we substitute the quantum dot concentration for [M], the total ODT for [Q], and we calculate the thiol binding constant K_a as the ratio of k_+ and k_-:

In the Tachiya model, (in the limit where k_q is much larger than k_+ and k_-) the average number of ligands bound to each quantum dot[3] is:

$$\bar{n} = \frac{[Q]}{2m} + \frac{m}{2} + \frac{m}{2 \cdot K_a \cdot [M]} - \frac{\sqrt{\left(\frac{[Q]}{[M]} + m + \frac{m}{K_a \cdot [M]}\right)^2 - \frac{4 \cdot m \cdot [Q]}{[M]}}}{2} \quad (2)$$

and the normalized solution photoluminescence (F) as a function of thiol concentration is:

$$\sum_{n=o}^{m} m! \frac{\left(\frac{\bar{n}}{m}\right)^n \left(1 - \frac{\bar{n}}{m}\right)^{(m-n)}}{n!(m-n)!\left(1 + \frac{n \cdot k_q}{k_0}\right)} \quad (3)$$

[M] and [Q] are known for each solution, k_0 and k_q are determined from solution lifetime experiments, and m and K_a are fitting parameters.

Experimental

CdSe quantum dots are synthesized using the method developed by Peng, *et al.*4 The quantum dots used in our experiments were made by combining 0.77 g CdO, 0.68 g oleic acid, and 2 g (95%) octadecene and heating to 220 ºC. Upon formation of Cd-oleate3, the solution turns clear and is removed from the heat. When the solution cools to room temperature, 0.5 g of (90%) trioctylphosphine oxide and 1.5 g of (97%) octadecylamine are added and the solution is then reheated to 280 ºC. At this temperature, 3 g of a Se-tributylphosphine (Se-TBP) solution (1.4 g Se, 3.84 g TBP, and 12.33 g octadecene, previously prepared and stored in a glovebox) is rapidly injected into the Cd-oleate solution. The crystals nucleate and then growth continues until the desired size is reached. At intervals throughout the growth period, aliquots of dots are removed to monitor the growth of the crystals by UV-Vis absorbance. The reaction is terminated by removing the heat. The quantum dots are then extracted twice with hexanes and methanol and centrifuged to separate methanol from the remaining quantum dot solution and any remaining methanol is removed. All solutions are stored in the dark.

The thiol titration experiments are conducted in toluene since impurities in H3Cl3 have been shown to affect quantum dot photoluminescence[2]. The CdSe quantum dot concentration is determined with the extinction coefficient for CdSe quantum dots[5]. The ODT concentration ranged from 1×10^{-2} to 1×10^{-9} M. All solutions were stored in amber vials in the dark.

Quantum dot absorbance was measured with an Agilent 8453 UV-Vis spectrometer. Photoluminescence was measured using a Horiba Jobin Yvon Spex Fluorolog-3 with an excitation wavelength of 405 nm. The data was corrected by baseline subtraction, the integrated photoluminescence is reported. Lifetime measurements were performed by time-correlated single-photon counting with a PicoHarp 300 using an excitation wavelength of 405 nm with a 5 MHz repetition rate. A 405 nm long pass filter was placed between the sample and a PDM 50 ct avalanche photodiode (APD).

Data & Results

Our experiments were completed using quantum dots with a first absorbance peak of 533 nm which corresponds to a quantum dot diameter of 2.8 nm. The data in figure 1 confirms the quenching model previously reported by Munro *et al.*[2] and shows that for a 400 nM quantum dot solution quenching occurs between total ODT concentrations of 10^{-6} M and 10^{-4} M.

The effects of ODT quenching on CdSe quantum dot lifetimes is shown in figure 2. The same solutions were used in figures 1 & 2. There is a decrease in the total number of photons observed in time, as well as an increase in the steepness of the decay curve. The lifetimes were fit with a stretched exponential:

$$f(t) = A_0 e^{\left(-\left(\frac{t}{\tau}\right)^{\beta}\right)} + C \quad \textbf{(4)}$$

using an Igor Pro v. 5.0 curve fitting. Where A_0 is the normalization constant, C is a constant, τ is the effective lifetime of the quantum dots in solution, and β is the stretched exponential factor. The values of β and τ are listed in table 1. Using these τ values we are able to approximate the magnitude of the k_0 and k_q values with the relationship:

$$k_{total} = \frac{1}{\tau} \quad \textbf{(5)}$$

[ODT]	τ	β
0.00E+00	8.9	0.61
2.22E-07	10.8	0.67
2.45E-06	10.2	0.61
7.34E-06	5.9	0.48
2.69E-05	2.5	0.38
8.07E-05	2.0	0.36
8.88E-04	3.4	0.41

TABLE 1. β and τ values for stretched exponential lifetime decay fits at different total ODT concentrations.

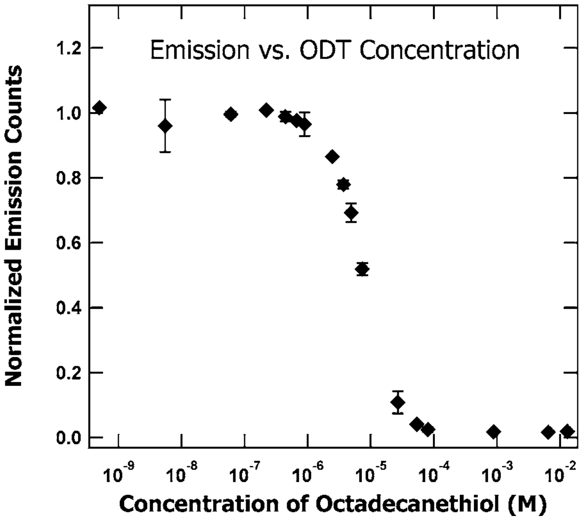

FIGURE 1. Normalized fluorescence emission counts plotted *versus* the concentration of octadecanethiol in solution.

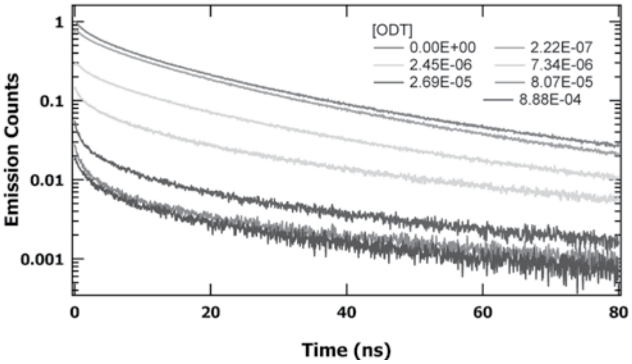

FIGURE 2. Quantum dot photon emission counts *versus* time for varying octadecanethiol concentration.

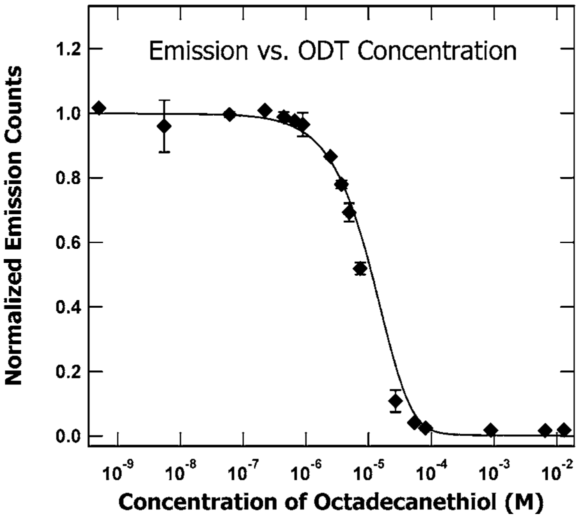

FIGURE 3. The photoluminescence as a function of total ODT concentration from figure 1 fitted with the Tachiya model. [M] = 3.81x10-7 M, k0 = 1x107 s-1 and kq = 1x109 s-1.

Figure 3 shows the photoluminescence titration curve from Figure 1 fit with the Tachiya model[1], holding [M], k_0, and k_q constant. We find that the Tachiya model fits the data allowing us to extract the number of quenchers per micelle and the binding constant. The fitting parameters appear reasonable since the quantum dot concentration is constant and the decay rates are determined from lifetime data with lifetimes of 1-100 nanoseconds. The binding constant shows that the rate of binding is much larger than the rate of dissociation and that there are about 6 thiol ligands on average attached to the quantum dot.

Conclusion

We have successfully measured precise titration curves and fit 400 nM concentration quantum dot data to the Tachiya model. Thiol binding increases the number of non-radiative decay pathways for an excited quantum dot. We can use the Tachiya model to understand the quenching mechanism by determining the number of binding sites per quantum dot (the maximum number of ligands bound) and the thiol – CdSe binding constant. We show that the Tachiya model fits our data with reasonable parameters. In the future, we plan to repeat these experiments with quantum dots that exhibit single exponential lifetime decay in the absence of ODT, in order to find k_0 and k_q. We also plan to repeat the experiment at different quantum dot concentrations, which will allow us to determine whether the model describes ODT quenching when the quantum dot concentration changes.

References

1. Tachiya, M. “Kinetics of Quenching of Luminescent Probes in Micellar Systems. II” *J. Chem. Phys.* 1982, *Vol 76, No 1, 340-348.*
2. Munro, A. M.; Jen-La Plante, I.; Ng, M. S.; Ginger, D. S. “Quantitative Study of the Effects of Surface Ligand Concentration on CdSe Nanocrystal Photoluminescence” *J. Phys. Chem. C* 2007, *Vol 111, 6220-6227.*
3. Tachiya, M. Private Communication.
4. Li, J. J.; Wang, A.; Guo, W.; Keay, J. C.; Mishima, T. D.; Johnson, M. B.; Peng, X. “Large-Scale Synthesis of Nearly Monodisperse CdSe/CdS Core/Shell Nanocrystals Using Air Stable Reagents via Successive Ion Layer Adsorption and Reaction” *J. Am. Chem. Soc.* 2003, *Vol 125, 12567-12575.*
5. Yu, W.W.; Qu, L.; Guo, W.; Peng, X. “Experimental Determination of the extinction Coefficient of CdTe, CdSe, and CdS Nanocrystals” *Chem. Mater.* 2003, V*ol 15, 2854-2860.*
6. Fisher, B. R., Eisler, H.J., Stott, N. E.; Bawendi, M. G. “Emission Intensity Dependence and Single-Exponential Behavior in Single Colloidal Quantum Dot Fluorescence Lifetimes” *J. Phys. Chem.* B. 2004, V*ol 108, 143-148.*

Acknowledgements

We would like to acknowledge the Ginger research group, Jaclyn Yetter and Sara Selfe for their assistance with this project, poster, and written work as well as the University of Washington for their facilities and support. We thank the Center for Materials and Devices for Information Technology Research (CMDITR) and the NSF Science and Technology Center No. DMR 0120967 for their financial contributions and provisions for the “Hooked on Photonics REU program” (CHE-0453596).

MEGAN E. LYDON The author really enjoyed her research project this summer at the University of Washington and looks forward to a career in research either through a doctoral candidacy or immediate immersion into the workforce upon graduation next year.

Alternative Methods for Collecting and Analyzing Data from Surface Plasmon Resonance Technology

JOSEPH P. MCCLURE, Norfolk State University
Brian Ferguson, Denise Wilson, University of Washington

Introduction

During the recent decades there have been a great number of uses found for Surface Plasmon Resonance (SPR) technology, with the most interest being focused on biological sensors and chemical detection. SPR works on a few different fundamental principles in Physics, particularly in the fields of Optics, Quantum Mechanics, and Solid State Physics. We use Snell's Law and Fresnel's Equations from Optics, to help us calculate the optical properties of a material, such as refractive index (RI).

We have the fundamental principles from Quantum Mechanics and Solid State Physics to help us describe how light interacts with matter and how atoms interact with other atoms, giving us the ability to engineer systems to monitor these interactions. When put together in a system, we get the following device that uses a polychromatic light, a Light Emitting Diode (LED), which illuminates a thin-filmed metal, gold in this experiment, deposited on a waveguide, fiber optic cable. At this interface some of the energy is transferred to the plasmons. Plasmons are oscillations of the electrons in the valence band in a crystal structure of a metallic solid. There is a wide range of wavelengths from the LED, allowing a spectrometer to show at what wavelength resonance occurs or the most energy is transferred. The wavelength at which this occurs is influenced by the environment, allowing the use of this technology for the applications mentioned earlier.

Both applications of this technology could provide great insight into providing the correct post devastation relief, following a hurricane, tsunami, or flooding. The major concern is the large amounts of food and water contamination that follows these events. This technology provides a way of detecting and monitoring such things, but due to the delicacy and expense of the equipment, it is not practical. This research will introduce innovative spectrometer designs and techniques for the collection and analysis of data from different system setups. The main focus is to remove the expensive optical arrangement and provide an equivalent electronic circuit, at a much lower cost and smaller size. These changes will provide the reliability and accuracy of the equipment used today, but will allow for greater mobility to the user, and will be of great use in many different environments.

Snell's Law

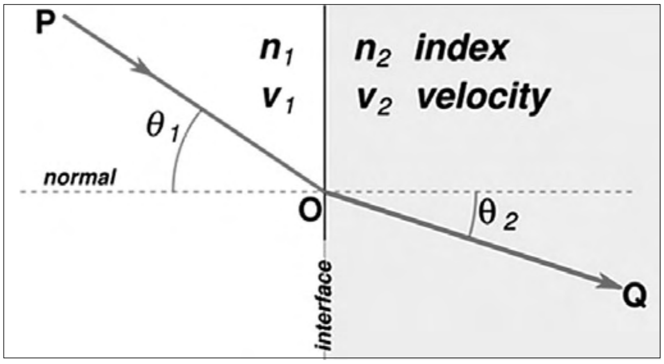

FIGURE 1. Demonstration of Snell's Law.

$n1 \sin \theta 1 = n2 \sin \theta 2.$

$$n = \frac{\text{speed of light(vacuum)}}{\text{speed of light(medium)}}$$

Fresnel's Equations

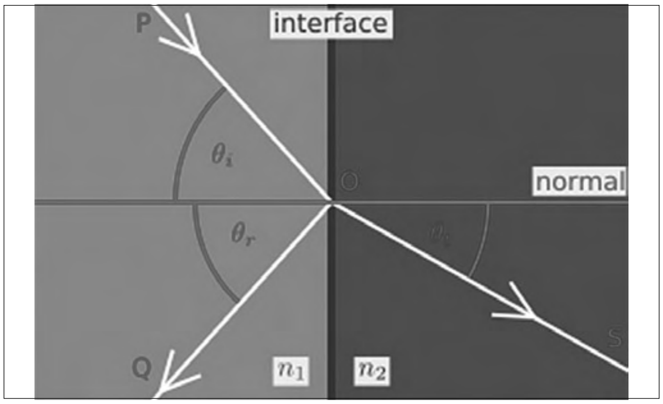

FIGURE 2. Demonstrates that Fresnel's equations takes into account for both the reflection and refraction the light in the interface and aids in reliability and accuracy of the equipment used today, but will allow for greater mobility to the user, and will be of great use in many different environments.

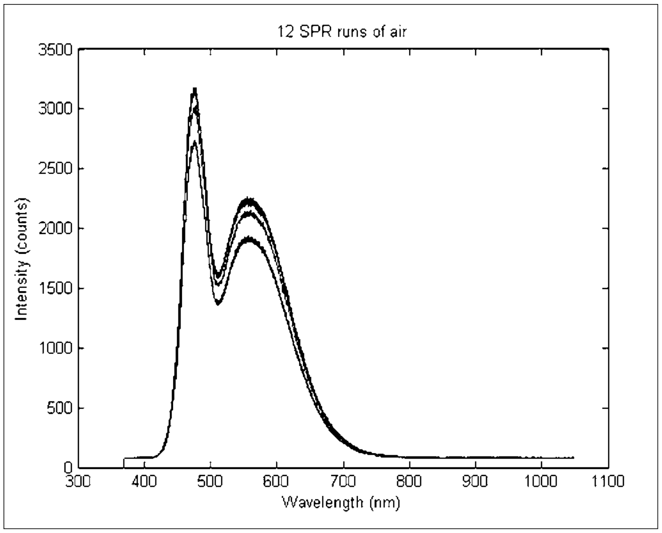

FIGURE 3. Intensity(arb. u.) vs. Wavelength(nm)- shows the spectrometer output to the computer, this is the white LED, showing the visible light spectra, having peaks in the blue and green wavelengths

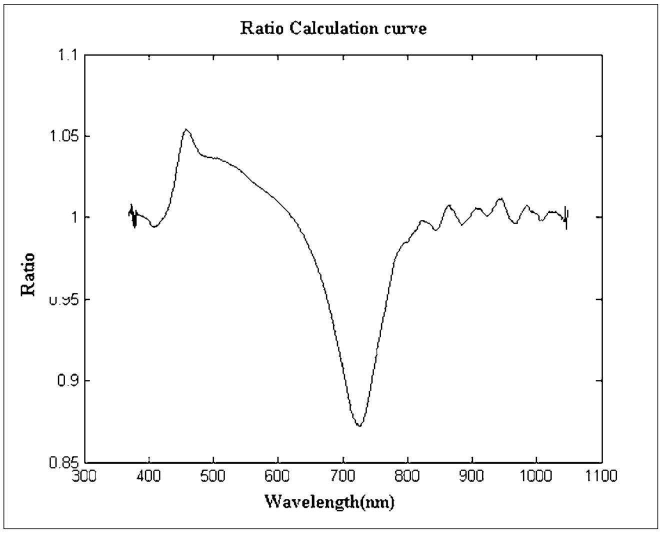

FIGURE 4. Ratio Air vs. Sample- demonstration of how to determine the wavelength at which the most energy is transferred, by taking the ratio of the spectra from sample versus spectra from known RI

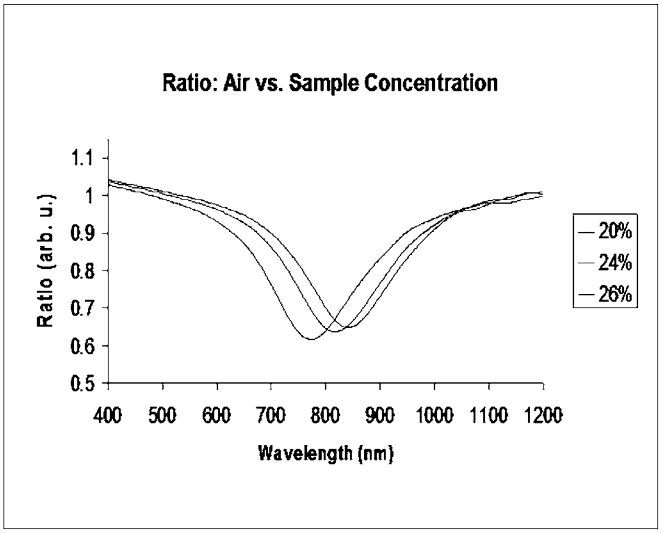

FIGURE 5. Ratio: Air vs. Concentration (Not all concentrations shown)—shows that as the concentration of the sample changes, the resonant wavelength changes.

As the change in RI is confirmed by the previous setup, the spectrometer was replaced with the photodiode circuit, measuring the output of the photodiode versus the intensity/current of the LED. Intensity of the LED is dependent on the current passing through the LED. We varied the current of the LED, to determine the best intensity for the device to be able to distinguish between the samples. This is plotted for the various samples as shown in Figure 6, with s1=35%, s5=33%, s10=30.5%, s15=28%, s20=25.5%

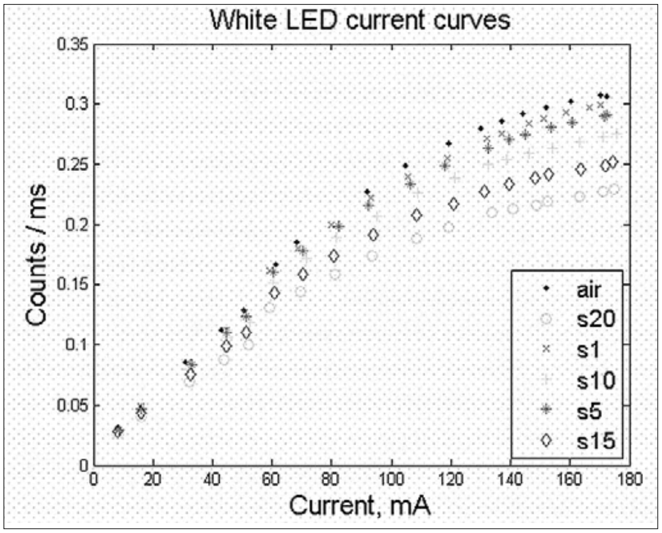

FIGURE 6. Intensity(counts/ms) vs. Current(ma)- here shows that with a change of current of the LED and the change in concentration of the samples produces a measurable change in the output of the photodiode circuit.

Results and Discussions

This experiment will try to demonstrate that there can be an equivalent electrical device to replace the spectrometer, capable of providing the same accuracy, while being a more mechanically stable device. Many of the basics principles that drive SPR now, will still apply here, with the only major change being that a photodiode will be used to convert the light energy into electrical energy. Initially twenty samples were prepared using sucrose dissolved in water as the chemical target. Solutions varied in concentration by percent mass, with the range being twenty five to thirty five percent, in half percent increments. The light source is a white Light Emitting Diode (LED), giving a polychromatic source. The SPR probe is a fiber optic waveguide, with a thin-filmed gold deposit on the surface. The reflected light from the probe is then analyzed by the spectrometer, providing a graphical output on the computer as demonstrated in Figure 3.

After data is collected on the response of the probe to a substance of known RI, the known substance being air, the probe is then inserted into a sample to determine how the RI changes with the environment. This is determined by taking the ratio of air versus sample to determine at what wavelength the most energy is transferred from the fiber optic probe to the solution. This gives the resonance frequency or wavelength, which can be used to calculate the RI. Taking this ratio produces Figure 4, showing the minimum point being the wavelength transferring the most energy. As the solution concentration is changed, there is a corresponding change in the minimum point, showing a change in RI, as shown in Figure 5.

Conclusions

As demonstrated, an equivalent electrical device can replace the spectrometer, providing a reliable alternative in SPR technology for evaluating the environment. Future work is going to use the same electrical device to determine the changes in the fluorescent intensity of a material *versus* the changes in concentration of the material. This will help collaborate the results from the SPR device.

Acknowledgements

Funds for this research were provided by the Center on Materials and Devices for Information Technology Research (CMDITR) and the NSF Science and Technology center No. DMR 0120967 and the Hooked on Photonics REU program No. CHE 0453596.

JOSEPH McCLURE. After completing my current enlistment in the United States Navy and my Bachelors Degree in Physics, I plan on attending graduate school to pursue a Ph.D. in science. Then I plan on continuing to do research and development.

Effect of Film Uniformity in the Performance of Spatial Light Modulators

IRMA A. NICHOLLS, University of Arizona
Haiyong Gan, Charles Greenlee, Robert Norwood, Nasser Peyghambarian, Mahmoud Fallahi
Fallahi Lab, Optical Sciences Center, University of Arizona

Abstract

Pixelated spatial light modulators were tested to evaluate the performance of each pixel by determining the finesse of the transmission peaks. Only 2-3 pixels out of 32 returned these results. A maximum finesse of 212 was obtained with a FWHM of 1.375 nm, and a free spectral range of 291. It was determined that the operation of these devices is affected by the roughness of the electro-optic film surface, the bowing of the substrate and fabrication errors. Future work will be focused in optimizing the fabrication process, using flatter polished substrates and decreasing the dimensions of the device.

Introduction

In this study, a 4x8 pixels and a 4x1 pixels matrix addressable samples were tested to assess their performance and to calculate the finesse of any transmission peaks obtained. The objective of this project is to evaluate the effect that the film uniformity, the bowing and roughness of the substrate, and errors in the manual assembly of the devices have in their performance to find solutions to improve their operation.

Fabry-Pérot étalon SLMs devices consist of a thin film layer of Electro-optic (EO) polymer with a distributed Bragg reflector (DBR) mirror on each side. This structure is a typical Fabry-Pérot etalon (Figure 1). Indium tin oxide (ITO) electrodes are adopted in the SLMs to apply voltage.[1]

EO polymers respond to a voltage applied to them by changing their refractive index. These materials have an EO coefficient that determines how sensitive they are to this effect. The change in index of refraction of the material is directly proportional to the EO coefficient and applied voltage. Therefore using a material with a higher EO coefficient will require less voltage to achieve the same effective change in refractive index.[2] Organic polymers and inorganic crystals observe this effect. The polymer AJL8/APC is inserted in the cavity, in between the two mirrors. This material is poled to align its molecules and make it sensitive to the application of a voltage.

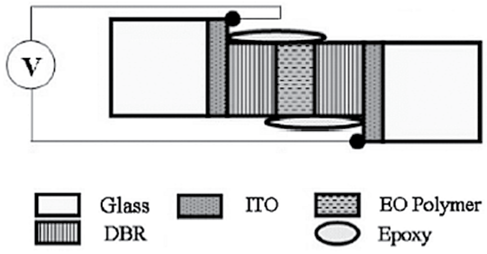

FIGURE 1. Fabry-Perot SLM structure.

The indium tin oxide (ITO) electrodes are deposited on the outside of the cavity, next to the mirrors. ITO was chosen for the electrodes due to its transparency. If a voltage is applied to the electrodes, the refractive index of the polymer inside the cavity changes. This produces a shift of the resonant wavelength. The device is covered by pieces of glass on both ends.

Non-uniformity in the polymer film, bowing of the substrates and thickness differences throughout device due to its manual assembly cause random phase changes in the waves of light that are going through the sample causing the transmission to be low, or the resonant wavelength to be shifted from its designed position. In many cases, no there is no wavelength selection and the light source is transmitted completely. Knowing how severe the damages are will provide useful insights about future improvements to better the performance of the SLMs.

This project requires the understanding of the operation of Fabry-Pérot optical cavities, the EO effect, the process of poling and why it is useful, the concepts of finesse and FSR and how they are related to the performance of an optical system. Also, it is important to understand the structure and optical properties of the EO polymers.

The tasks involved in this project require the ability to make decisions about the instruments needed to perform the experiments and the ability to setup and use ray tracing to align the devices, and know how to measure the EO coefficients. Also, it is required to know how to use many electronic equipments such as optical spectrum analyzer, a multimeter, a power source, an erbium doped broadband light source, and etc. One should also have the ability to interpret and organize the collected data.

Experimental Methods

The performance of the SLMs will be determined by shining light from a broadband source on each pixel of the device and calculating the finesse of the transmission peaks observed using an optical spectrum analyzer to visualize the intensity of the light that goes through each pixel as a function of the transmitted wavelength.

The measurements are made using an erbium doped fiber broadband source that is connected to an optical fiber that brings light to the system. A lens is used to collimate the light that subsequently passes through an adjustable aperture and it is transmitted through the sample. The light is then focused by another lens to be collected by a second optical fiber that takes it to an optical spectrum analyzer (OSA).[1,2] Figure 2 illustrates this setup.

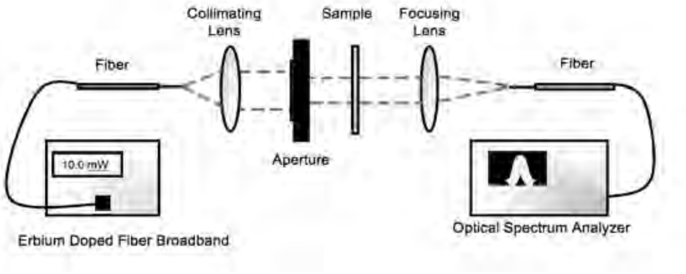

FIGURE 2. Testing setup.

The device is mounted on a 2D-translational stage that allow it to be scanned in the horizontal and vertical directions. Each pixel in the device is scanned and the results are recorded by the OSA and afterwards the data is transferred to a computer using LabView. The tests were performed on a (4x8) and a (4x1) matrix addressable device using two beam sizes, 1 mm and 500 μm.

The finesse is a quantity that denotes the quality of a Fabry-Perot peak. The devices are designed to work at a wavelength of 1550 nm. It is expected to that a good device will produce narrow peaks with high intensity relative to the light source at this wavelength with no voltage applied. The effective finesse is defined by equation (1) as the free spectral range (FSR) divided by the full width at half the maximum (FWHM) intensity of the peaks.[3] These dimensions are illustrated in figure 3.

$$Finesse = \frac{\Delta\lambda_{FSR}}{\Delta\lambda_{FWHM}} \qquad (1)$$

Each peak is designated by an order number m. In general, the performance is better if the finesse is higher.

Since the bandwidth of the source is not wide enough to produce two peaks, the free spectral range will be estimated.

Having an estimated value for the thickness of the polymer d, the order m to find the free spectral range can be obtained using the equation

$$\frac{2\pi}{\lambda}2nd - 2\Phi(\lambda, n) = 2m\pi \qquad (2)$$

Then equation (2)[2,3] is solved for the exact value of the thickness d.

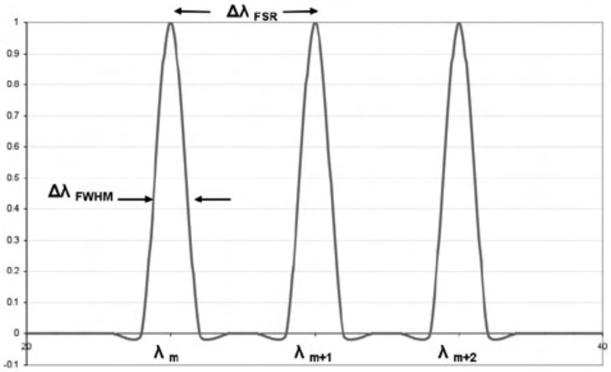

FIGURE 3. Fabry-Pérot peaks for finesse calculation.

The free spectral range is found using equation (3)

$$\frac{2\pi}{(\lambda \pm \Delta\lambda_{FSR})}2nd - 2\left[\Phi(\lambda, n) \pm \frac{\partial\Phi}{\partial\lambda}\Delta\lambda_{FSR}\right] = 2(m \pm 1)\pi \ldots \qquad (3)$$

Where n is the index of refraction of the polymer, d is the thickness of the polymer, λ is the peak wavelength and $\Delta\lambda_{FSR}$ is the free spectral range, $\Phi(\lambda,n)$ is the phase as a function of the peak wavelength and the index of refraction of the polymer, m is an integer and $\delta\Phi/\delta\lambda$ is the slope of the reflectance-phase vs. wavelength curve shown in figure 4.

Eight equations were obtained and solved for the FSR and the smallest value for FSR was chosen.

Results

The (4x1) device showed no Fabry-Perot peaks.

Two pixels in the (4x8) device show Fabry-Perot peaks using a 1 mm diameter beam. Figure 5 below was produced by one of the pixels. The resonant wavelength is at 1526.5 nm. The free spectral range of the device is 291 nm. The finesse of the peaks is 212, since both beam sizes produce peaks with a FWHM of 1.375 nm.

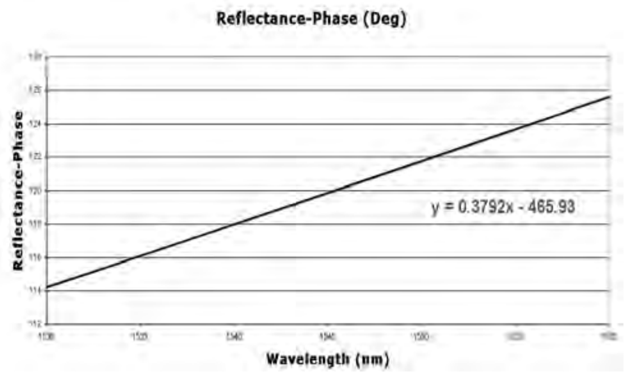

FIGURE 4. Reflectance-Phase vs. wavelength graph used for FSR calculation.

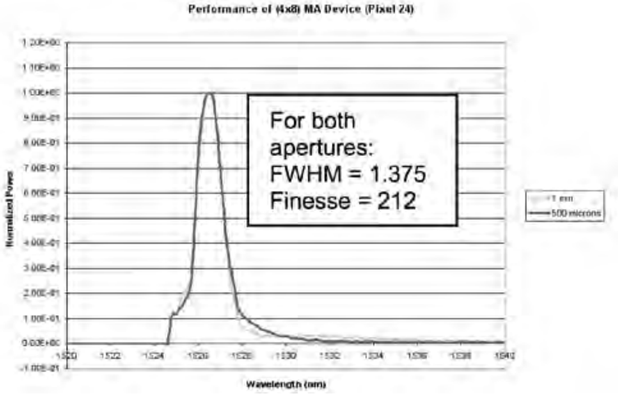

FIGURE 5. Transmission peaks produced by a pixel in a (4x8) MA device for 1 mm and 500 micron beam sizes.

Figure 6 illustrates three important results. First, it is observed that reducing the beam size improves the performance of the peaks in some cases. The peak produced with a 1 mm beam has a FWHM of 2.125 nm and a finesse of 137. Second, the peaks produced between pixels appear to be sharper than those produced by the center of the pixels. Third, the resonant wavelength is shifted to 1538 nm.

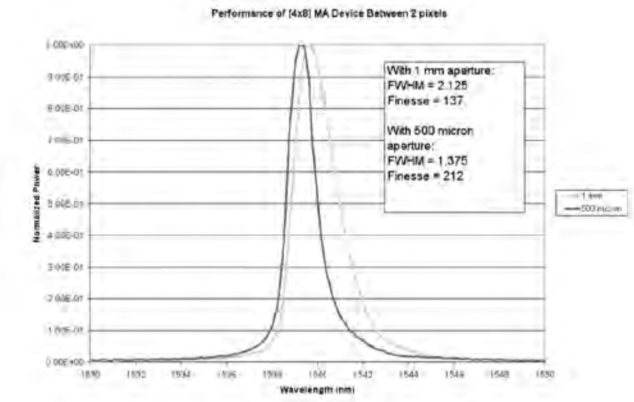

FIGURE 6. Transmission peaks produced in the space between two pixels in a (4x8) MA device for 1 mm and 500 micron beam sizes.

Discussion

Based on the previous results it can be inferred that the quality of the substrates, the roughness of the film, and fabrication errors have a great impact in the performance of the devices since the majority of the pixels produce no useful results. It is expected that using higher quality polished substrates and improving the current spin-coating techniques would solve the problem. The area in between pixels contains polymer but no ITO. The roughness of the electrode might be also causing difficulties. The consistency of the finesse values demonstrates that there is uniformity in an area within 500 micron squared. The wavelength shift is due to thickness changes in the device that can be produce by assembling the device manually. This problem could be addressed by reducing the size of the device. However, there is a limit for the pixel size since testing very small pixels represents great difficulties.

Conclusion

The result of testing Fabry-Perot spatial light modulators proved that film uniformity, the bowing and roughness of the substrate and assembly errors plays a central role in the performance of spatial light modulators. Future work will be oriented to the improvement of current spin-coating and assembly techniques. High quality substrates such as polished BK7 and silicon wafers will be used in order to reduce the bowing and surface roughness. Finally, the overall size of the device will be reduced to an area of 500 microns squared in order to avoid thickness differences.

References

1. H. Gan, H. Zhang, C.T. DeRose, R.A. Norwood, and M. Fallahi, Appl. Phys. Lett. 89, 141113 (2006).
2. H. Gan, H. Zhang, C.T. DeRose, R.A. Norwood, N. Peyghambarian, and M. Fallahi, Appl. Phys. Lett. 89, 041127 (2006).
3. Wyant, James; Optics 505 Spring 2000, http://www.optics.arizona.edu/jcwyant/Optics505(2000)/ChapterNotes/Chapter07/multiplebeaminterference.pdf (accessed June 2007/July 2007)

Acknowledgements

National Science Foundation
University of Arizona
Optical Sciences Center

Special thanks are given to Olli Nordman for ITO deposition, Elena Temyanko for mirror deposition and training, and Yevgeniy Merzlyak for optical fibers.

This work was made possible by the NSF sponsored Science and Technology Center on Materials and Devices for Information Technology Research, No. DMR-0120967.

IRMA A. NICHOLLS. I am currently an undergraduate at the University Of Arizona Optical Sciences Center. I plan to graduate with a Bachelor of Science degree in Optical Sciences and Engineering in 2008 and proceed to graduate school to earn a Ph.D. in Biomedical Engineering.

Nonlinear Optical Properties of Donor Acceptor Charge Transfer Composites

CHARLES C. OCHOA, Florida International University
San-Hui Chi, Dr. Joeseph W. Perry department of Chemistry, Georgia Institute of Technology

Objective

The objective of this study was to determine if polymers or compounds designed for two photon absorption (TPA) and PCBM form a charge transfer complex or interact through intermolecular charge transfer to perform as optical power limiting (OPL) materials

Background

Materials that selectively filter out high intensity light are called optical power limiting materials. Power limiters provide the ability to rapidly shield human eyes and sensors from high intensity light that could otherwise cause damage. Obvious applications are for personal eye protection to be worn by researchers that work with high intensity pulsed lasers, and for shielding sensitive sensors [1]. Two photon excited charge transfer (CT) is one mechanism by which OPL in organic devices may be realized.

Two photon absorption refers to the absorption of two photons each of half the energy needed for one photon absorption. Because this process requires absorbing two photons near simultaneously, it occurs under high intensity. Subsequent transitions might then be possible that correspond to the energy of the incident light (see Figure 1). This would result in an optical power limiter. However, dynamical concerns make this harder to achieve. If the rate at which the electrons return to their ground levels is relatively fast then the population in the excitedstate will not be sufficient to support strong absorption to further levels. To remedy this, charge transfer may be used to extend the duration of photo induced absorption.

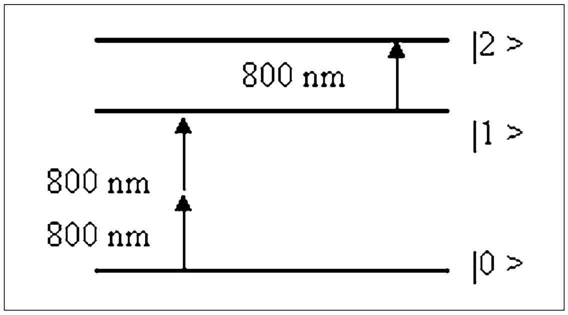

FIGURE 1. TPA energy level diagram.

Charge transfer refers to the transfer of charge between a molecule of low ionization potential (a donor) and one of high electron affinity (an acceptor) [2]. Photo induced charge transfer can be exploited for OPL use by selecting acceptor molecules that have strong high energy absorbance in the region to be limited. The photo excitation of the donor allows transfer to the acceptor where the strong absorption is present. Utilizing a donor with a large TPA cross section allows for two photon excited charge transfer. The ultimate benefit of such a scheme comes from its modification to the population dynamics. Typically, distancing the charges in separate donor and acceptor molecules lengthens the time that electrons take to fall back to their initial states and recombine with the positive charge left behind in the donor. Thus the strongly absorbing excited state transitions will remain sufficiently populated.

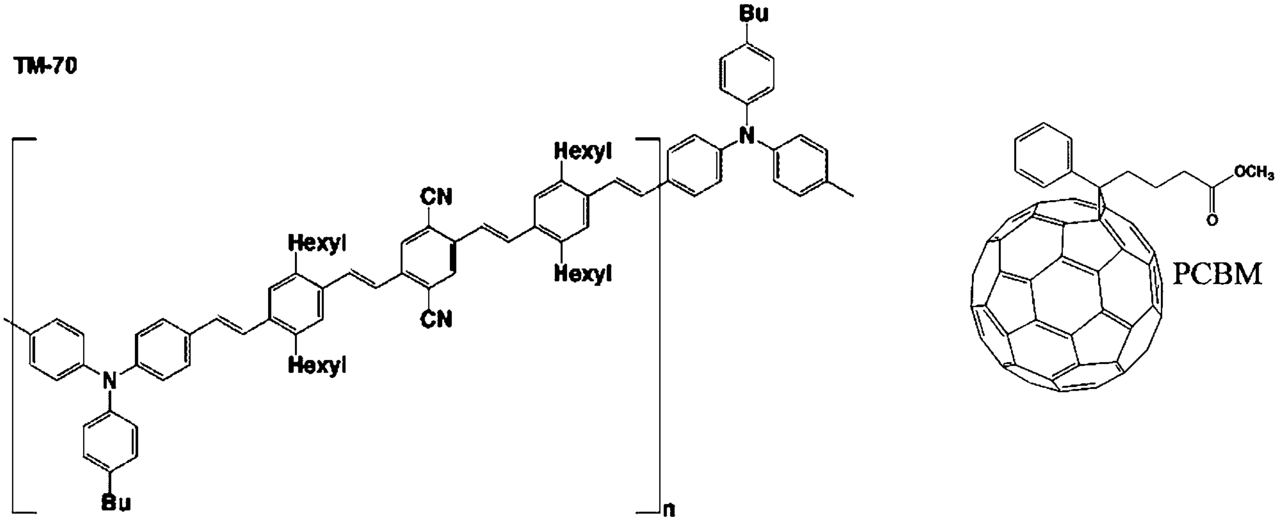

FIGURE 2. Chemical Structure of TM-70 and PCBM.

This study considers the mixture of donor polymer Poly [4-butyl -*N, N*-bis (4-ethenylphenyl) aniline-*co*-bis(2,5-di-*n*-hexylstyryl)-2,5-dicyanobenzene], TM-70, of large TPA cross section [3] with a strong acceptor PCBM (Solenne) , a soluble fullerene (see Figure 2). A commercially available polymer poly[2-methoxy-5-(2'-ethylhexyloxy)-1,4-phenylene vinylene], MEH-PPV, (Aldrich) was used as the control in both material processing and characterization, see Figure 3.

A previous study determined the TPA cross section of TM-70 to be about 1020x10^{-50} cm^4 s per repeat unit at peak absorption of 890 nm [3]. In this project, we report the study of the processing methodology of the material and its composite as well as their nonlinear optical properties for OPL applications in 700-900 nm.

Experimental:

I. Material processing & Characterization

To support a wide range of optical tests, both thin (200-300nm) and thick (>10 μm) films were required. Thin films can be produced via spin coating, whereas thick films can be made by melting.

Spin casting or coating is a technique for producing thin films by depositing solution on a substrate and then spinning to smooth and dry the surface. Spin casting has several variables which can be adjusted to achieve a good quality film; namely, solution viscosity (as adjusted by concentration) and the spin parameters (time and spin speed). Other variables like temperature, substrate wetting, and the presence of a solvent saturated environment can have a considerable impact on film thickness and quality. It has been shown [5] that typically film thickness is related by a power law to concentration and inversely to a power law of spin speed. Hot isostatic compression or melting, likewise, is a process whereby some sample is heated between two slides and a thickness controlled spacer to above its glass transition temperature and then quickly quenched to avoid the formation of crystalline microdomains.

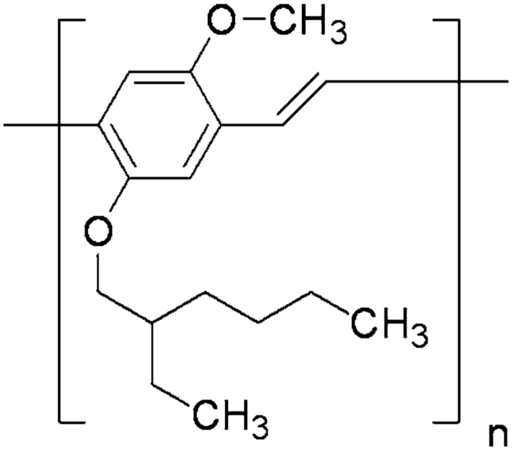

FIGURE 3. Chemical structure of MEH-PPV.

A. THIN FILM PROCESSING & CHARACTERIZATION

MEH-PPV was selected to optimize the processing procedures for TM-70, the latter being in short supply. For thin films this required determining the effects of solution concentration and spin speed on film thickness. Methods for removing defects such as particles and aggregates were also developed and evaluated.

Solutions of both neat MEH-PPV and MEH-PPV/PCBM were made by dissolving in chloroform. Film thickness measurements were made with a profilometer and absorption spectra were taken in a UV-Vis spectrometer (HP 8453). Images with 40x magnification were produced with a microscope (Digilab UMA 600) for analysis. Composite films ranging from ~10% to 30% PCBM by weight were produced in the same manner.

B. THICK FILM PROCESSING & CHARACTERIZATION

Thick films were produced by pre-dissolving MEH-PPV with or without PCBM in a mixture of dichloromethane and Dioctyl phthalate, DOP (Aldrich) plasticizer in quantities that would yield about 50% plasticizer by weight, see Figure 4. The pre-dissolved solution was sonicated and stirred to achieve homogeneity, and then dried under vacuum to remove solvent. The remaining material was hot melt pressed at ~210°C to produce 25 and 100 μm thick films.

The absorption band edge and transmittance in the 700-900 nm region was characterized by a UV-Vis-NIR spectrophotometer (Shimadzu UV-3101PC). Images (40x) were also taken to qualitatively determine the optical quality of films.

II. Transient absorption

An attempt was made to measure the lifetime of the charge transfer states. High intensity light from a 532 nm 500 mJ pulsed laser was passed through a sample. A white light incident on the sample, operated at 110 watt, was passed through a monochronometer and then into a photomultiplier tube (PMT). By measuring the output of the PMT before and after the laser pulse, the change in absorption and its time decay can be observed. The solutions used in this experiment were sampled 512 times each per measurement to average out the effects of noise in the signal.

Initial testing revealed very weak signal from spun films. As a consequence dilute solutions were utilized instead. Samples were prepared in chloroform and bubbled under nitrogen for approximately 10 minutes to avoid possible oxygen quenching.

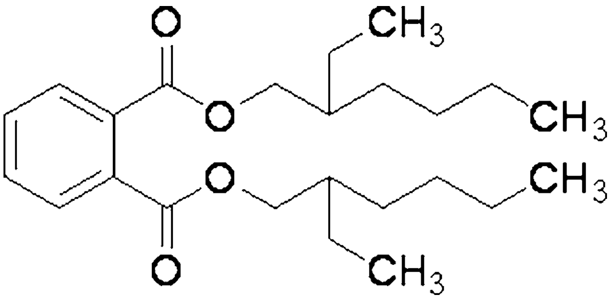

FIGURE 4. Chemical structure of DOP

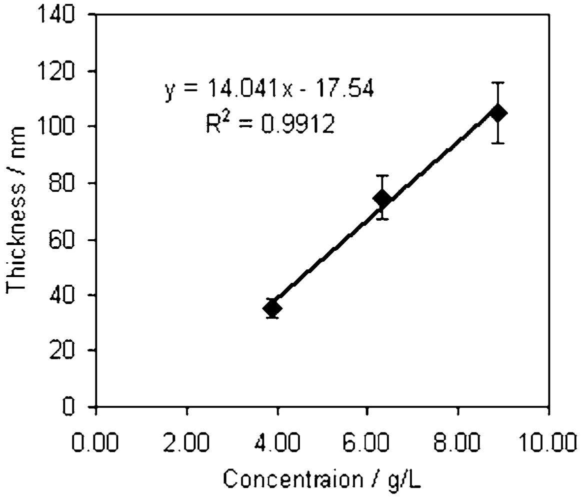

FIGURE 5. Concentration of neat MEH-PPV solution (g/L of CHCl3) versus film thickness (nm), spun at 2000 rpm for 2 min.

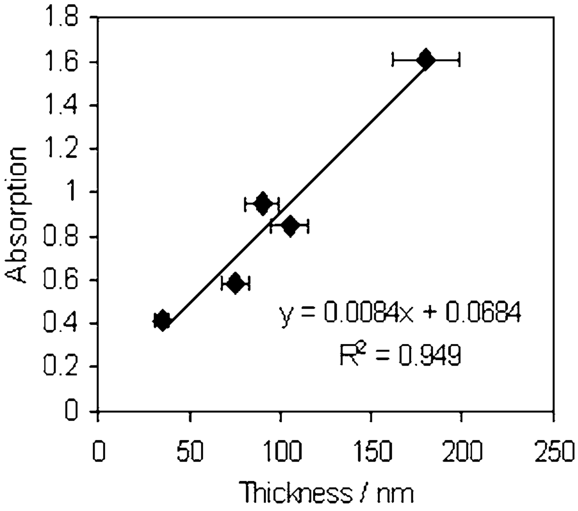

FIGURE 6. Thickness (nm) versus absorption of neat MEH-PPV spun films, 2000 rpm for 2 min.

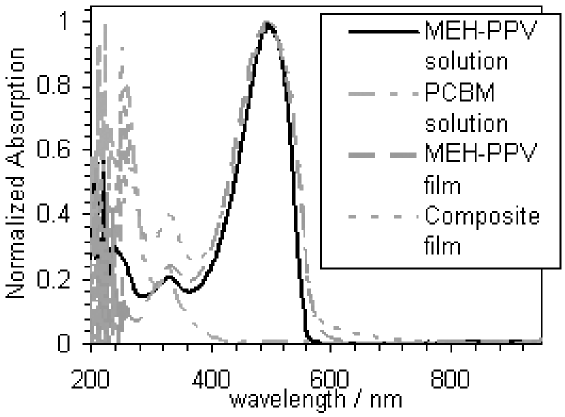

FIGURE 7. UV-Vis linear absorptions spectra for neat MEH-PPV, composite (20% PCBM) film, and solutions.

Results and Discussion

Film thickness as controlled by solution concentration was determined by profilometry (see Figure 5). A linear relationship was observed between peak absorbance and thickness as shown in Figure 6. UV-Vis linear absorption spectra were taken for neat and composite films as well as solutions. In all cases the materials showed weak absorption in the 700-900 nm region (see Figure 7). For composite films a slightly broadened peak was observed which could indicate some charge transfer absorption.

Phase separation might have been caused by uneven drying of the solvent prior to spinning (the time between starting to deposit the solution and spinning). To remedy this a few changes were made. The method for depositing solution was standardized so that all of the solution was deposited quickly in the center of the substrate. More importantly the spin casting environment was saturated with the solvent in use. In a solvent saturated environment the rate at which the solvent evaporated was moderate, allowing the film to spread evenly before significant drying. This proved effective in eliminating phase separation. The results of this change can be seen in images 1 and 2.

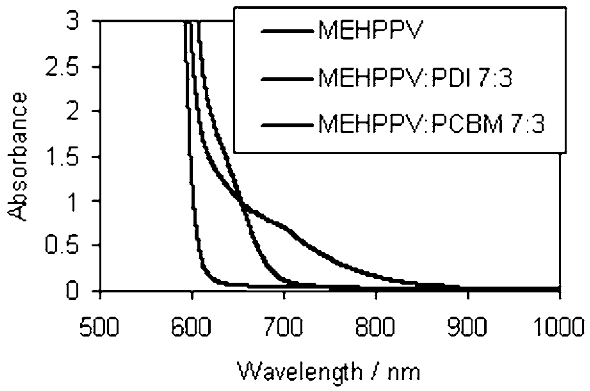

Average Transmission from 700-900 nm 25 µm films	
MEH-PPV	94.35%
MEH-PPV-PDI	93.20%
MEH-PPV-PCBM	64.39%

FIGURE 8. UV-Vis linear absorptions spectra for neat MEH-PPV and composite 25 µm DOP melted films.

As thicker films were produced by varying both the concentration and the spin speed, the particle count seemed to increase. Such particles could potentially scatter light and introduce error in optical tests. Solutions were sonicated to breakup any aggregates in conjunction with filtering to remove any non-soluble contaminants. Initial testing with 0.2 µm PTFE filters proved difficult due to the viscous nature of the solution. 1.0 µm filters were found to work but still proved difficult for thicker solutions. A program was written to analyze microscope image files and return particle size statistics via an image mask. It found dark pixels and recursively searched for connected clusters, which were treated as particles. The average particle size was found to be about 3.8 ± 1.5 µm. A GMF-150 filter of 2.0 µm was used and proved effective in reducing particle count while not impeding flow to any problematic degree.

With increasing film thickness, overall surface uniformity began to become an issue. A film that is locally smooth but has a global curvature could potentially act as a lens. A film that is severely non-uniform can diffuse light. To alleviate this problem spin speed and time were reconsidered. Uneven film thickness can possibly be attributed to in homogeneity in the starting solution or too low of a spin speed. Stirring the solution with a magnetic stirring bar immediately prior to spinning may help. However it is likely that some thickness could be sacrificed toward a higher spin speed which may solve the problem. Further research is required.

Melted films produced with plasticizer showed promising optical quality. UV-Vis spectrum revealed similar characteristics as the thin films including a slightly broader falloff in composite films, see Figure 8. Overall average transmission in the 700-900 nm region was high, ranging from 64-94%. The clarity of the films was also observed from microscope images, see images 9-12. Melting PCBM composite films proved more difficult than neat films. Some experimentation including Perylene diimide derivatives, PDI, as an acceptor molecule was also initialized, see Figure 9. MEH-PPV/ PDI composite films proved easier to melt. By the nature of its structure PDI may innately function as a plasticizer. A TM-70 and PDI composite film was melted with DOP (image 8) however further work is still needed.

The transient absorption was found to have both a fast and slow decay as modeled with a bi exponential and fit to minimum reduced chi-square. The fast decay was found to have a lifetime of about 0.7 ms and the slow decay calculated out to about 7 ms. The lifetime of the charge transfer state can then be estimated as the lifetime of the fast decay. There were however several issues. Poor signal quality forced the use of multiple pulses per measurement to average out random influences. An unoptimized experimental setup may have resulted in an overall offset; accounting for the negative signal. A baseline correction was allowed in the fitting function.

It was observed that, after the transient absorption test, a solution that was initially orange in color turned yellow. Figures 11 and 12 indicate a possible degradation of the polymer rendering any measurement after the first laser pulse uncertain. Figure 11 shows how rapidly the peak absorption dropped per 512 laser pulses, whereas Figure 12 shows the very noticeable decrease and shift of the linear absorption peak before and after the entire test. Signal degradation during averaging is then also likely to have happened. The successive average of decreasing signals with different rate constants

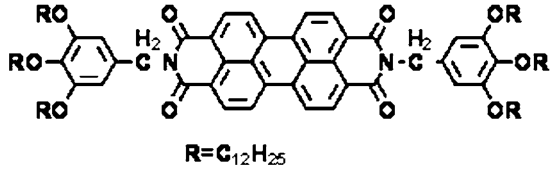

FIGURE 9. Chemical structure of PDI derivative

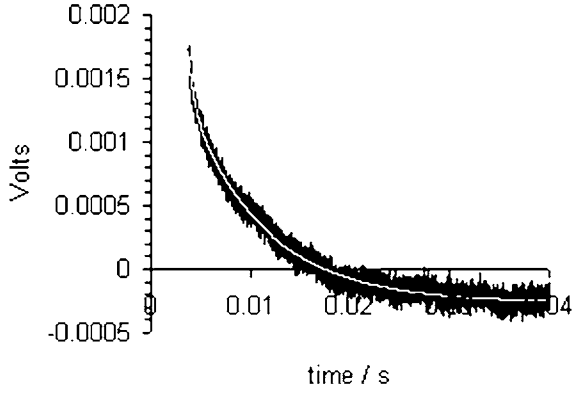

FIGURE 10. Change in absorption versus time for a 30% composite solution at 825 nm, pump wavelength at 532 nm. Bi exponential fit with fast decay .7 ms and slow decay of 7 ms.

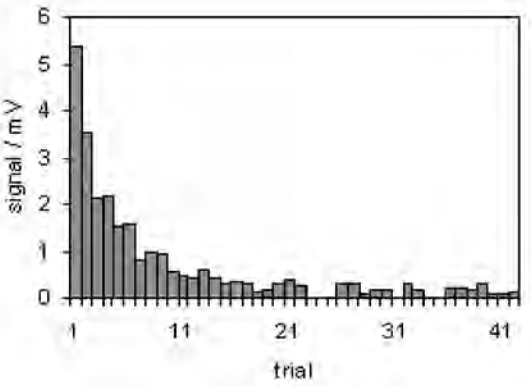

FIGURE 11. negative of max absorption signal versus trial for 30% composite solution at 825 nm.

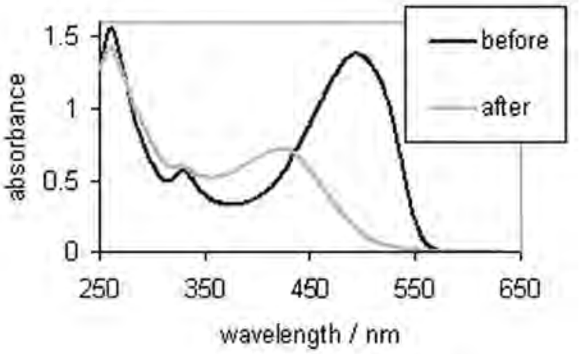

FIGURE 12. Before and after transient absorption test UV-Vis spectrum. 30% PCBM solution.

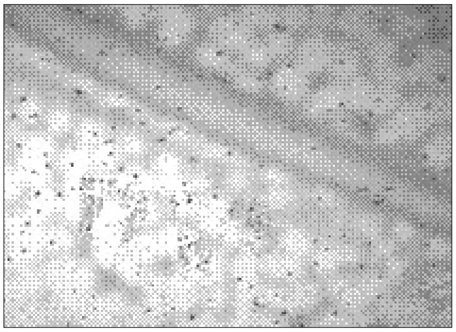

1. Neat MEH-PPV film of concentration ~6 g/L. Spun in non-saturated environment shows significant phase separation.

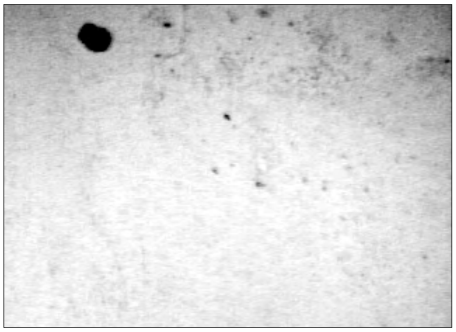

2. Same concentration as in 1, but spun in solvent saturated environment.

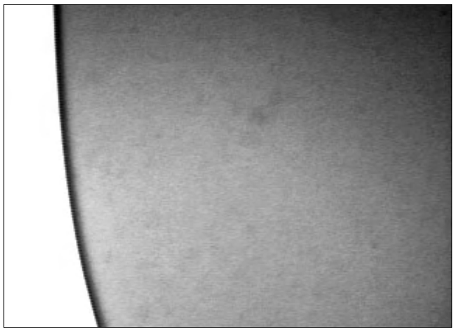

3. Neat MEH-PPV (~9 mg / 700 ul CHCl3) after 2 um filter, spun for 2 min at 2000 rpm. Large particles are defects in the glass slide, but could also possibly be debris added by the glass filter.

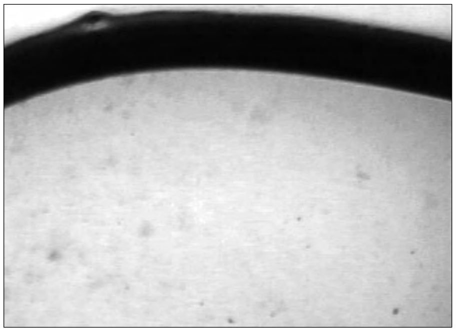

4. Image used in particle counting program. At least 245 particles in image.

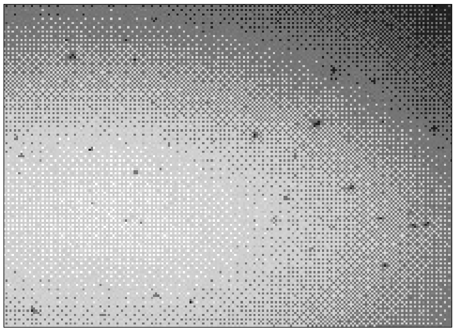

5. Mask of image 4. Dark region in the upper right corner was manually removed and not counted.

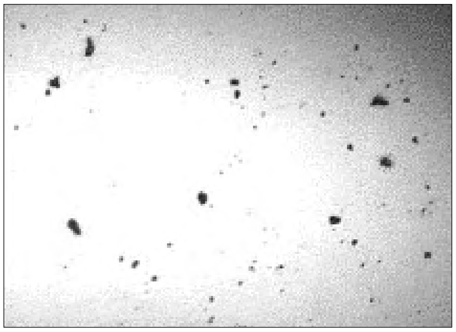

6. Same solution as in 3 but no filter

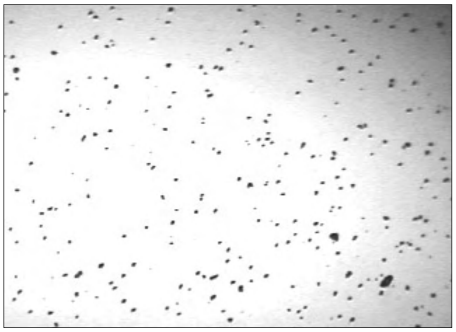

7. 8.88 mg MEH-PPV and 2.35 mg PCBM (20.93%) in 800 uL CHCl3, non-filtered spun for 4 min at 1600 rpm. 225 nm thickness.

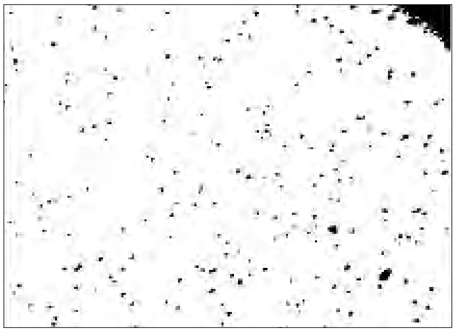

8. 1.27 mg TM-70 and 0.62 mg PDI with 1.8 mg DOP in CH2Cl2 25 μm composite film.

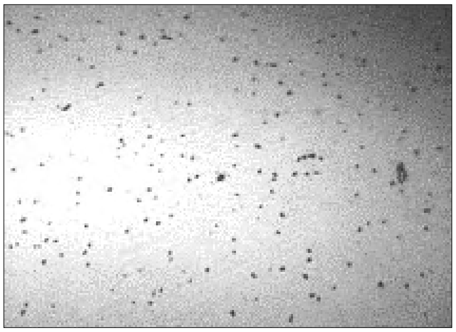

9. MEH-PPV 25 μm composite, good clarity

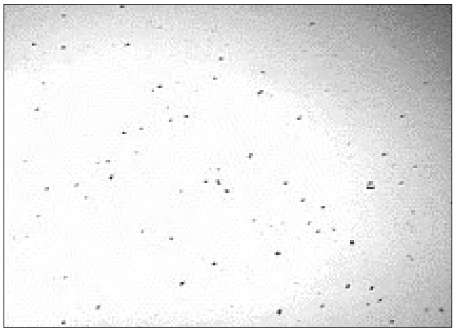

10. MEH-PPV PCBM 25 μm composite, shows in homogeneity due to difficulty in melting PCBM

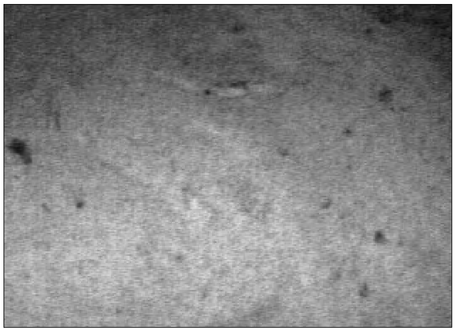

11. MEH-PPV / PDI 25 μm compsite, shows great clarity

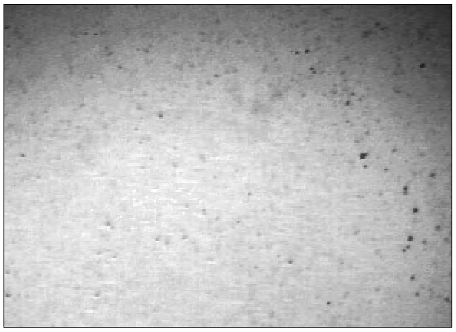

12. MEH-PPV 100 μm composite

would certainly modify the calculated lifetime. Reasonably, several other mechanisms may be responsible for the long lifetime observed. However it is expected that the use of chloroform for the solvent along with the possible presence of oxygen are directly responsible. Due to the sample degradation, a strict comparison with the pure donor material is difficult. The donor did show some signal albeit weak. Further work will seek to remove the environmental and chemical influences that might be responsible for such rapid degradation as well as the electrical issues in the setup which may have introduced noise and uncertainty.

Conclusion

This project has studied the processing of organic polymers which may be used for OPL applications. Achieving optical quality films through spin casting is an intricate process with several variables. Optimization of this process was carried out with MEH-PPV polymer and was able to yield thin films of about 200-400 nm with various degrees of quality. Very thick (100 μm) films of optical quality were produced through the liberal use of plasticizer and hot isostatic compression. Further work will continue to apply these processing techniques to the target donor TM-70. Furthermore, the nonlinear optical properties of these materials and their ability to function as optical power limiting devices will be explored.

Acknowledgments

The author would like to acknowledge several insightful conversations with both San-Hui Chi and Dr. Joe Perry, his mentor and advisor respectively. Additionally, Joel Hales is thanked for his help with the profilometer measurements. Additionally Matteo Cozzuol is thanked for his work on the transient absorption measurements. Research support is gratefully acknowledged from the National Science Foundation Center on Materials and Devices for Information Technology Research (CMDITR), DMR-0120967, and the Defense Advanced Research Projects Agency (DARPA) on MORPH program, ONR N00014-04-0095.

References

1. Spangler. C. W.; *J. Mater. Chem.*, 1999, 9, 2013-2020.
2. Bender, C. J. *Chem. Soc. Rev.*, 1986, 15, 475-502.
3. Wenseleers, W.; Stellacci, F.; Meyer-Friedrichsen, T.; Mangel, T.; Bauer, C. A.; Pond, S. J.K.; Marder, S. R.; Perry, J. W. *J. Phys. Chem.* B 2002, 106, 6853-6863.
4. J. W Perry, in *Nonlinear Optics of Organic Molecules and Polymers,* ed H.S. Nalwa and S. Miyata, CRC Press, Boca Raton, 1997, pp. 813-840.
5. Thompson, Bowden. *Introduction to Microlithography.* Pg 187-195.

CHARLES C. OCHOA recently graduated from Florida International University with a BS in Math and BS in Physics. He is pursuing a masters there in financial mathematics. He has interests in complexity, human intelligence, deterministic chaos and nonlinear systems. Following his masters he intends to pursue a Ph.D in an area tightly related to artificial intelligence and cognitive science.

Reversible Local Chemical Modification by Thermochemical Nanolithography

ODION OKOJIE,[†] Debin Wang,[†] Will D. Underwood,[‡] Marcel Lucas,[†] Simon C. Jones,[‡] Robert Szoszkiewicz,[†] Takashi Okada,[‡] Tai-De Li,[†] William P. King,[∞] Seth R. Marder,[‡] Elisa Riedo[†] • School of Physics, Georgia Institute of Technology; School of Chemistry and Biochemistry, Georgia Institute of Technology; University of Illinois, Urbana-Champaign

Introduction

Advances in nanolithography are essential for the miniaturization of devices for data storage, chemical/biological sensing and microfluidics [1]. So far, nanometer-size features have been patterned mostly by photolithography, which introduces only irreversible topographical changes. The development of the dip-pen lithography process enabled the surface chemical functionalization with the local deposition of inks, but this technique lacks the ability to erase and the speed required for the design of complex patterns on a large scale. Erasable nanopatterning techniques have been developed based on reversible electrochemical reactions and photosensitive polymers. Patterns as small as 400 μm were written and erased electrochemically with microelectrodes, but the same microelectrode could not be used to read the data, and the maximum writing speed was limited at 5 μm/s [2]. Also, high-resolution photolithography on photosensitive polymers requires expensive short-wavelength lasers and aligners [3].

Recently, sub-15 nm features were written and read at a high speed of about 1.4 mm/s by thermochemical nanolithography (TCNL), which introduces local surface chemical modifications by scanning the substrate with a hot atomic force microscope (AFM) tip [1]. However, the ability to erase the patterns was not demonstrated. In this study, a reversible chemical reaction is developed to add a write-read-erase-rewrite capability.

Experiment

Macroscopic films (thickness 500 nm) of a copolymer, poly (tetrahydro-2H-pyran-2-yl methacrylate)$_{80}$ poly(3-{4-[(E)-3-methoxy-3-oxoprop-1-enyl] phenoxy}propyl-2-methacrylate)$_{20}$ were spin coated on a glass substrate. At room temperature, the polymer samples present ester groups at its surface. At about 120ºC, the tetrahydropyranyl groups are removed, modifying the ester to a carboxylic acid. At about 180ºC, the acid groups turn into anhydrides. Anhydrides should revert back to carboxylic acids by immersion in an acidic aqueous solution (Fig. 1) [4].

Ten samples were first heated to 230ºC to convert the ester groups into anhydrides. Four heated samples were then immersed in 4 aqueous solutions of various pH: 2, 3, 4, and 7.6 for 14 hours. The remaining 6 samples were divided into 3 sets of 2 samples. The first set of samples underwent no agitation, the second set was placed in a sonic bath and the third set was immersed in a solution kept at 70°C. In each set, one sample was immersed in distilled water for 2 hours, while the other was immersed in an acidic solution of pH=3 for 2 hours.

The chemical modifications will be characterized by water contact angle measurements (Phoenix 150, SEO), friction measurements (CPII, Veeco), and Fourier transform infrared spectroscopy (FTIR) (UMA-600, Digilab) at room temperature. Contact angle measurements were taken on three different points of the sample and the results are the average of the left and right

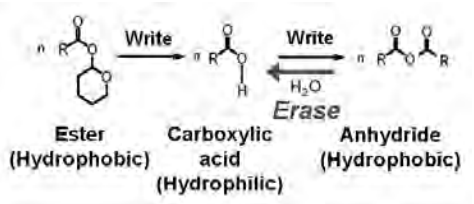

FIGURE 1. Chemical reactions involved in the writing and erasing processes.

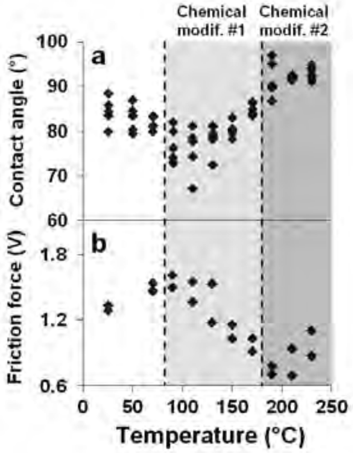

FIGURE 2. (a) Contact angle and (b) friction force after a heat treatment to a selected temperature.

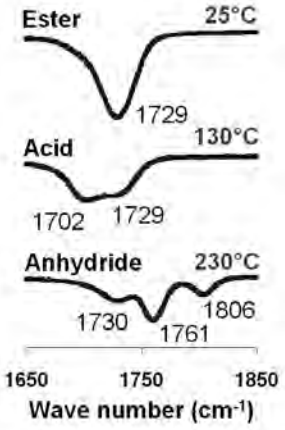

FIGURE 3. Infrared spectra before and after heat treatment at 130°C and 230°C.

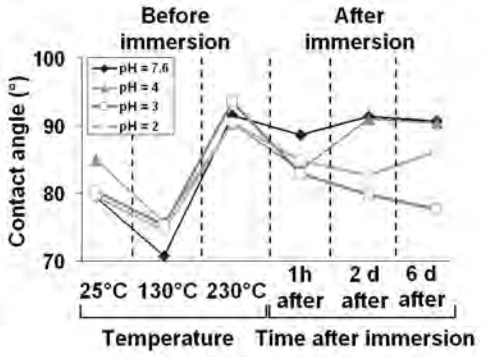

FIGURE 4. Contact angle before and after immersion in solutions of various pH. Before immersion, the contact angle was measured before and after the 2 chemical modifications. The contact angle was also measured 1 hour, 2 days, and 6 days after immersion.

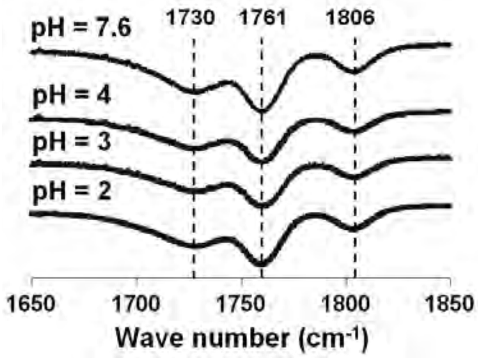

FIGURE 5. Infrared spectra after immersion in solutions of various pH.

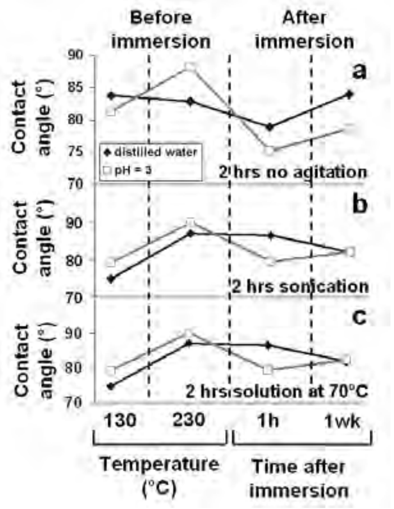

FIGURE 6. Contact angle before and after immersion for 2 hours in distilled water and a pH=3 solution (a) without agitation, (b) with sonication, and (c) maintained at 70°C.

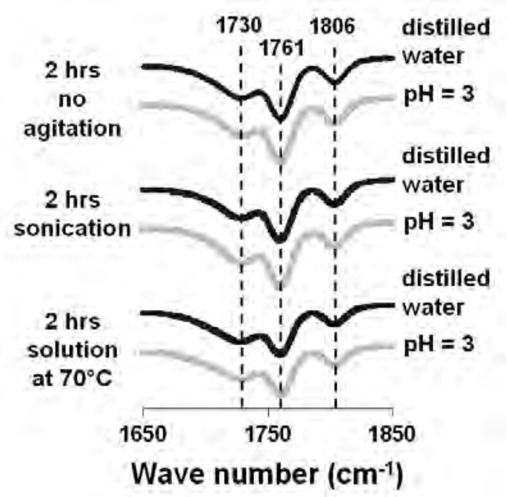

FIGURE 7. Infrared spectra after immersion for 2 hours in distilled water and a pH=3 solution without agitation, with sonication or maintained at 70°C.

contact angles. The friction force is measured by collecting pairs of lateral force images, when the tip is scanned over a small area of the sample (typically 500 nm x 500 nm) from left to right, and right to left. The Si_3N_4 cantilever (Veeco probes) used has a spring constant of 0.04 N/m. The lateral force signal is averaged over 256 lines and the friction force is defined as half the difference between the lateral force signals in the two scanning directions.

Results and Discussion

The water contact angle of the polymer sample was measured after a heat treatment at a temperature between 25ºC to 230ºC (Fig. 2a). It drops from 85º at room temperature to about 75º after a heat treatment at 110ºC, and then increases to about 90º after further heat treatment at 230ºC.

The water contact angle varies with the affinity of the polymer surface with water. If the material is hydrophilic, the water droplet tends to spread on the polymer surface, thereby making the contact angle more acute. If the surface is hydrophobic, the interface area between the water droplet and the sample is minimized, thereby making the contact angle larger. The contact angle drop is consistent with the successful conversion of the hydrophobic ester to the hydrophilic acid. At 230ºC, the contact angle increase is also consistent with a successful conversion to the hydrophobic anhydride (Fig. 1).

The friction force was also measured on the sample as a function of the temperature of the heat treatment. It increases as the temperature increases from 25ºC to 110ºC and then reduces with further heating at higher temperatures up to 230ºC (Fig. 2b). The AFM tip is hydrophilic so if the sample is also hydrophilic they tend to attract each other, making the friction force high, as the tip scan the sample. If the material is hydrophobic the AFM tip and the sample will repel each other, and therefore it will slide easily across the sample with a lower friction force. The friction force increase between 25ºC and 110ºC is consistent with the successful conversion of the hydrophobic ester to the hydrophilic acid. With further heating up to 230ºC, the friction force decrease is also consistent with a successful conversion to the hydrophobic anhydride (Fig. 2b).

The transition of the ester groups to carboxylic acids and then to anhydrides was confirmed by infrared spectroscopy (Fig. 3). At room temperature, the infrared spectrum shows a band centered at 1729 cm^{-1} which correspond to the C=O stretching mode in an ester. An additional peak at 1702 cm^{-1} in the spectrum of the sample heated to 130°C indicates that the ester transitioned into an acid. Finally, the IR spectrum of the sample heated to 230°C exhibits bands centered at 1761 cm^{-1} and 1806 cm^{-1} characteristic of an anhydride.

The contact angle was measured before and after immersion in solutions of various pH (Fig. 4). To ensure that the acidic solution did not interfere with the contact angle measurement, the samples were rinsed thoroughly and dried under ambient conditions. The contact angle was measured 1 hour, 2 days and 6 days after the samples were removed from their respective solutions. The contact angle measured 1 hour after immersion in solutions of pH = 2, 3, 4, 7.6 showed a drop compared to the contact angle before immersion, particularly on the sample immersed in the pH = 3 solution, where it dropped from 93° to about 83°. The contact angle measured 6 days after immersion in solutions of pH = 4 and 7.6 revealed that their respective values returned to the values before immersion, showing the effect of the solution on the measurement itself. The contact angle measured 6 days after immersion in solutions of pH = 2 and 3 showed that the drop persisted, and for the sample immersed in the pH = 3 solution, the contact angle further decreased to 79°. However, the infrared spectra of all the immersed samples still exhibit the bands characteristic of an anhydride (Fig 5).

The contact angle decrease from that of the hydrophobic anhydride indicates that the anhydrides were partially reconverted into carboxylic acids, since the contact angle drop after immersion is smaller than the contact angle increase after the conversion from carboxylic acids to anhydrides. It is possible that the reverse reaction occurred only at the surface of the samples and not within the layers of thickness of the polymer. FTIR spectroscopy probes the sample over its entire thickness and is therefore not sensitive to any surface chemical modification.

To reduce the immersion time and ensure complete reversibility of the acid-anhydride reaction, the solutions (distilled water and pH=3 solution) were sonicated or heated to 70°C for 2 hours, while the samples were immersed. The contact angles of 2 samples left in solutions for 2 hours without agitation or heat showed a contact angle drop after immersion, similar to the one after immersion for 14 hours (Fig 6a). Contact angle measurements also show that sonication and heat did not improve significantly the yield of the reverse reaction (Fig. 6b,c). The infrared spectra of the samples after immersion show the 3 bands characteristic of anhydrides (Fig. 7), and the band centered at 1702 cm^{-1} characteristic of the carboxylic acids is not observed (Fig. 3).

Conclusion

Based on water contact angle, friction measurements, and infrared spectroscopy it was demonstrated that the polymer can be chemically modified twice. The original hydrophobic ester undergoes a conversion to a hydrophilic acid with a heat treatment at 130ºC first, and then to a hydrophobic anhydride after further heating to 230ºC.

A contact angle variation indicates that immersion in an acidic solution of pH = 3 resulted in the reversal of the acid to anhydride reaction. Immersion times longer than 2 hours, sonication and heating the acidic solution to 70°C have no significant effect on the contact angle variation resulting from the reverse reaction. Infrared spectra indicate that the reverse reaction only occurs at the sample surface which was exposed to the acid solution.

Acknowledgments

This work is supported by the NSF grant DMR 0120967
and CHE 0453596.

References

1. Szoszkiewicz, R.; Okada, T.; Jones, S. C.; Li, T.-D.; King, W. P.; Marder, S. R.; Riedo, E. *Nano Lett.*, 2007, 7, 1064.
2. Turyan, I.; Krasovec, U. O.; Orel, B.; Saraidorov, T.; Renata, R.; Mandler, D. *Adv. Mater.,* 2000, 12, 330.
3. Athanassiou, A.; Varda, M.; Mele, E.; Lygeraki, M. I.; Pisignano, D.; Farsari, M.; Fotakis, C.; Cingolani, R.; Anastasiadis, S. H. *Appl. Phys. A,* 2006, 83, 351.
4. L.G. Wade, Jr.; *Organic Chemistry,* Fourth Edition. Prentice Hall, 1999.
5. Stevens, M. P. *Polymer Chemistry: An introduction,* Third Edition. Oxford University Press, 1999

ODION OKOJIE, Case School of Engineering, Case Western Reserve University.

"Speak your truth quietly and clearly and listen to others, even the dull and ignorant…
they too have their own their story" –ANONYMOUS

Anisotropic Kink Adsorption

of 2’, 7’ –Dichlorofluorescein in Potassium Acid Phthalate (KAP)

MIRANDA E. ROBERTSON, Edmonds Community College
Theresa V. Bullard, Bart E. Kahr, University of Washington

Introduction

Dyed crystals can be used as tools for understanding crystal growth and surface chemistries at a molecular level. They have also been created and used for spectroscopic and photonic purposes[1], crystal dye lasers, chiroptical investigations, single molecule photophysics, and understanding the orientation of single molecules in ordered media. The primary focus of this research was to try to determine how dye becomes incorporated into a model crystal system, known as potassium acid phthalate, C_6H_4·COOH·COOK (KAP), during growth, and how impurities influence the kinetics, shape and number of hillocks present in a crystal.

KAP was chosen as the model crystal system because of the distinctiveness in its appearance. When the KAP crystal reaches maturity, it produces a large clear (010) face or *b*-face; moreover, this crystal has well developed growth features, known as hillocks that appear on its largest expressed face2. With the *b*-face being large and clear, it allows for easy viewing of hillocks on the crystal surface.

Hillocks are shallow stepped hills that appear on a growing surface as a result of screw dislocations, disturbances in the crystal lattice with Burgers vector[3] perpendicular to the growing surface of the crystal[4]. KAP hillocks are polygonized into two slopes, a fast and a slow slope that result from KAP’s polar *c*-axis (Figure 1). The polar axis results from the phthalate molecules of KAP being aligned in a ‘herring-bone’ array along the *c*-axis, leading to a net dipole moment. Steps propagating in the +*c* and –*c* directions are therefore different in structure and become polygonized as a result of different rate constants and step kinetics[5].

Intrasectoral zoning of dyes[4] can be used to label polygonal hillocks throughout the growth history of a crystal grown from solution. The dye chosen for this research, 2’,7’-dichlorofluorescein (DCF), has been shown to selectively recognize and become overgrown within the fast slope of KAP hillocks[6].

This renders the fast slopes, visible to the eye under fluorescent light as more and more dye is incorporated during growth. Even though the mode of entry into the crystal is as yet unknown, DCF can be used as a tool to locate hillocks and probe surface chemistries during growth.

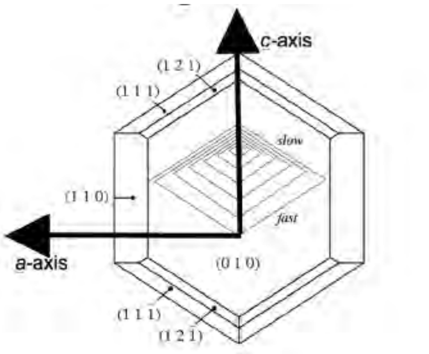

FIGURE 1. This is a representation of a KAP crystal. On the (010) face is a hillock that has become polygonized into a “fast” and “slow” slope along the polar *c*-axis, due to the difference in KAP’s structure in the +*c* and –*c* directions.

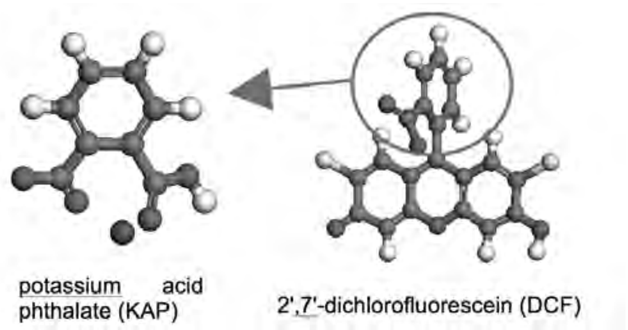

FIGURE 2. Circled carboxyl group in DCF is similar in molecular structure to KAP.

It was believed that DCF’s strong affinity for the KAP hillocks was due in part to its molecular structure being similar to the phthalate ion in KAP (Figure 2). To check this, modeling was preformed by Theresa Bullard using Accelrys Materials Studio Modeling Suite[7] to try and gain a better understanding of the DCF interactions in KAP. The modeling showed DCF behaves similar to the phthalate ion, with the upper carboxyl group connecting to the potassium ions in the KAP lattice. The simulations indicated that when DCF docked into the fast steps, it tended to align its transition dipole moment along the step edge[8]. Furthermore, early experiments performed by the Kahr group showed that the transition dipole moment orientation of DCF changes with increasing dye concentration. The initial modeling, in concert with the experimental data, lead to the hypothesis that the dye orientation was coupled to the fast step orientation. Additionally, the presence of the dye may induce morphology changes within the hillocks, thereby manifesting as an observed change in transition dipole moment orientation. In order to verify this experimentally, the use of trivalent cations was proposed to significantly manipulate the hillock morphology and see how this influenced the dye behavior.

This research project built off of studies performed by Hottenhuis *et al.*, where intentional trivalent cationic impurities were shown to have specific step and kink inhibiting effects when adsorbed into

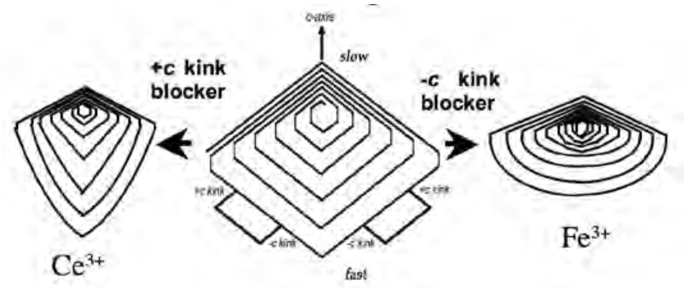

FIGURE 3. This image shows where the two cations enter the kink sites. Ce^{3+} enters the +*c* kink site and Fe^{3+} the –*c* kink. These two ions block the dye and KAP from entering the kink site of its preference[2,5,9].

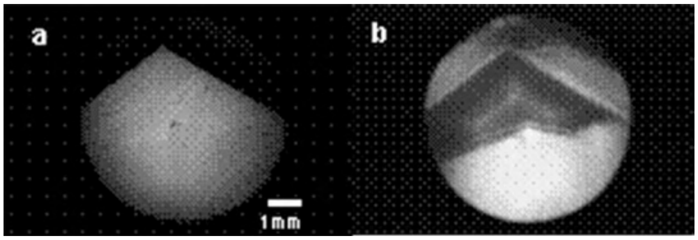

FIGURE 4. A comparison of images showing reflected light differential interference contrast microscopy (DICM) of the crystal surface and hillocks (a) and fluorescence microscopy of the same area (b).

KAP hillocks[2,5,9]. Ce^{3+} and Fe^{3+} in particular were chosen because each one influences the shape of the hillock in a very distinct manner through selective kink adsorption. Ce^{3+} and Fe^{3+} were presumed to block opposite kink sites, based on their resulting effects on hillock morphology. Ce^{3+} blocks the +*c* kink site, and as a result the hillock morphology changes to an elongated form (Figure 3). Fe^{3+} has the opposite effect on hillock morphology. Fe^{3+} blocks the –*c* kink site, and as a result the hillocks become wider and round in the fast slope (Figure 3).

With the addition of DCF, we proposed to observe how the dye's behavior becomes altered by the impurities' influences on hillock morphologies and kink blocking. With this we hoped to isolate where the dye was incorporating, and more clearly identify its correlation to KAP hillock morphology.

Experimental

All KAP crystals consisting of each impurity were grown in a systematic fashion. The change in trivalent cation concentration was systematic, as were the changes made to DCF concentration. The range of concentrations used for each are as follows 0.1ppm to 15.0ppm for Ce^{3+}, 5.0ppm to 20.0ppm for Fe^{3+}, and 1×10^{-6}M to 5×10^{-5}M for DCF (1ppm of Ce^{3+} and Fe^{3+} = 5.56×10^{-5}M)[9]. Crystals were grown from supersaturated aqueous solutions at constant temperature, via spontaneous nucleation consisting of KAP salt and purified water (Barnstead NANOpure Diamond™).

The salt forms of the impurities used were cerium (III) chloride ($CeCl_3$) and ferric nitrate ($Fe(NO_3)_3 \cdot 9H_2O$). The amount of KAP salt and impurity salt were determined thru stoichiometry methods.

After dissolving impurities into 110 g/L KAP solution, the solutions were filtered using VWR International filter papers 415 (20.5cm) into crystallization dishes. Solutions were then placed in a PRECISION Microprocessor Controlled 280 Series Water Bath at a constant temperature of 30°C and left uncovered for growth by slow evaporation. Crystal solutions remained in the water bath for 3 to 4 days until they reached maturity. Single crystals were then harvested and the (010) face blown dry using a jet of nitrogen air. The crystal (0-10) bottoms were cleaved off for better imaging and analysis.

A combination of qualitative and quantitative data was taken for final analysis. The methods used to collect the qualitative data were differential interference contrast microscopy (DICM) and fluorescence imaging. The instrument used for both theses methods was a LEICA DIC/Fluorescence microscope with a Nikon D80 attached to it. In DICM mode this microscope uses cross polarized reflective light and a prism for enhancing contrast of interference light that reflected off the surface hillocks (Figure 4a). Under fluorescence, DCF emits green (~530nm.) light, illuminating the location of the hillocks and allowing for the apex angles to be determined (Figure 4b). The fluorescence images made it possible to view the hillocks throughout the entire crystal. In compilation, these methods were used to determine hillock morphology changes as impurity concentrations were systematically increased.

Quantitative fluorescence data were taken using a FluoroMax-2 Fluorimeter coupled to an inverted stage Olympus microscope. This instrument was used to measure fluorescence intensity of DCF by collecting emission spectra through an Olympus 10x objective, which was then normalized by crystal thickness, as measured with micron-scale calipers. Another instrument used to gather quantitative data was the Olympus BX50 attached to a Photonics UV-VIS Spectrophotometer. This instrument was used to systematically gather polarized absorption anisotropy spectra for all the crystals with different DCF concentrations..

The extinction directions along the *a*- and *c*- axes of the birefringent KAP crystals were used to orient the sample relative to the input polarization. Absorption transition dipole moment orientations were computed according to: , where the dichroic ratio (DR = I_a/I_c) is corrected for sample birefringence (Figure 5).

Results and Discussion

The two microscopy techniques made it possible to qualitatively determine the morphology changes of the hillocks and to see if and where the dye was incorporated. In the case of Fe^{3+}, the inclusion of DCF was minimal; therefore, it was not possible to obtain emission intensity spectra. However, for Ce^{3+}, there was enough dye incorporated into the crystals to collect spectra. It was observed that the hillock angles would increase as the Ce^{3+} concentration was increased do to the boundary between the fast and slow slope increasing progressively, until the slow slope essentially disappears from the fast slope spanning almost 360° and the dye entering the entire (010) face (Figure 6).

The fluorescence intensity of dye increased until 4.0ppm of Ce^{3+} and then progressively decreased afterwards (Figure 7). The initial increase in fluorescence intensity is due to more dye incorporation resulting from fast slope morphology changes. After 4.0ppm, the Ce^{3+} impurities begin to significantly impede growth and inhibit the inclusion of DCF into the crystal, leading to thinner crystals, less dye incorporation, and an overall lower emission intensity.

Polarized absorption spectroscopy data were systematically taken for each impurity and dye concentration. Measurements were taken for light polarized along the *a*-axis and *c*-axis at three different positions on each crystal. From these spectra the absorption maxima (470nm & 500nm) were used to quantitatively determine the average bulk orientation of the dye's transition dipole moments with respect to the *a*-axis (Figure 8).

Dye orientation data were also confirmed via confocal polarized fluorescence measurements performed by Kristin Wustholz to match the values obtained from polarized absorption anisotropy, within the experimental uncertainties.

The averaged orientation data collected from polarized absorption spectra are shown in the summary plots below. The first summary plot is for the crystals grown with Fe^{3+} (Figure 9), showing that as the concentration of Fe^{3+} was increased the average DCF dipole transition moment orientations remained consistently between 40 and 45 degrees from the *a*-axis, indicating no change in dye orientation as a result of hillock morphology changes. It was also interesting to note that when the Fe^{3+} concentration increased past a critical point, not only would the hillock morphology change, but the crystal habit itself changed; the crystals became smaller and had a rounded –*c* en d.

Recall that Fe^{3+} blocks the –*c* kink site, thus forcing KAP and dye incorporation to take place at the +*c* kink site or along the step edge. However, it was observed that far less dye was incorporated into the crystals indicating a competition between DCF and Fe^{3+} for the same kink site, and an aversion for the dye to go into the +c kink site.

A similar summary plot was constructed for Ce^{3+}, but it showed a different behavior than that of the Fe^{3+} data (Figure 10).

This plot shows the average orientations of DCF's transition dipole moment moving closer to the *a*-axis as the concentration of Ce^{3+} progressively increases. For example, at 0.1ppm the orientation is at approximately 45° and progressively decreases towards

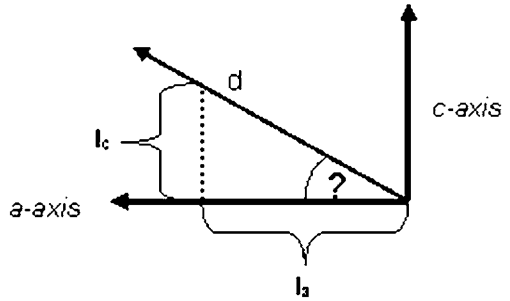

FIGURE 5. Diagram of dipole orientation and equation used to calculate the dipole orientation angle of DCF.

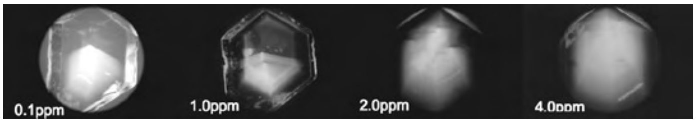

FIGURE 6. As Ce^{3+} concentration increases (from left to right), the boundary between the fast and slow slope increases progressively until dye enters the entire (010) face.

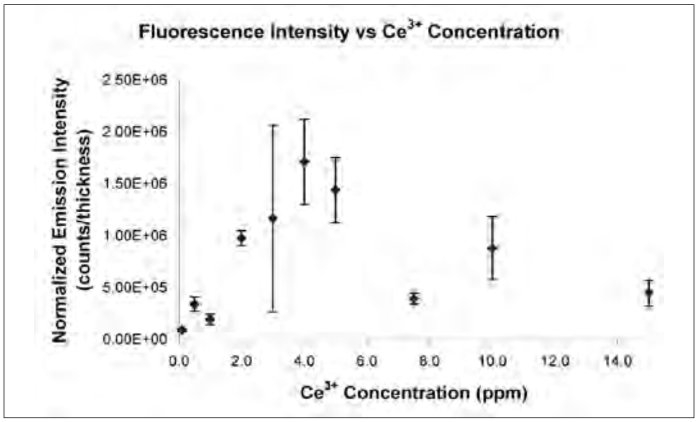

FIGURE 7. Normalized fluorescence intensity versus Ce^{3+} concentration, showing an initial increase in dye inclusion, followed by a decrease due to severe kink blocking and growth inhibition.

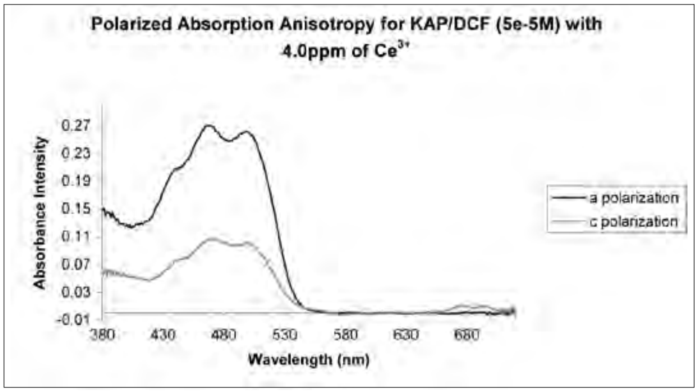

FIGURE 8. This is an example of the spectra gathered from polarized absorption spectroscopy, showing anisotropic absorbance intensity for light polarized along the *a* and *c* axes.

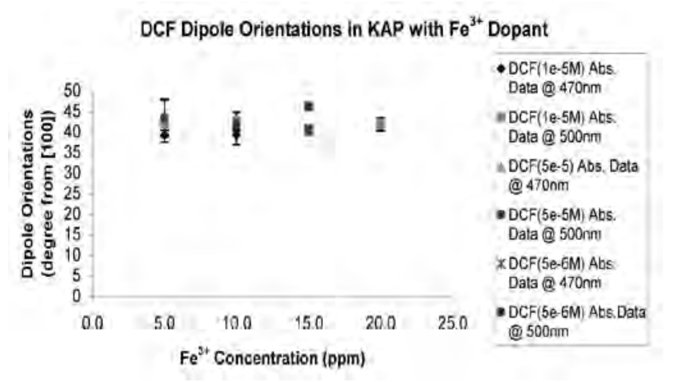

FIGURE 9. Average transition dipole moment orientations remained consistent as the Fe^{3+} concentration was increased

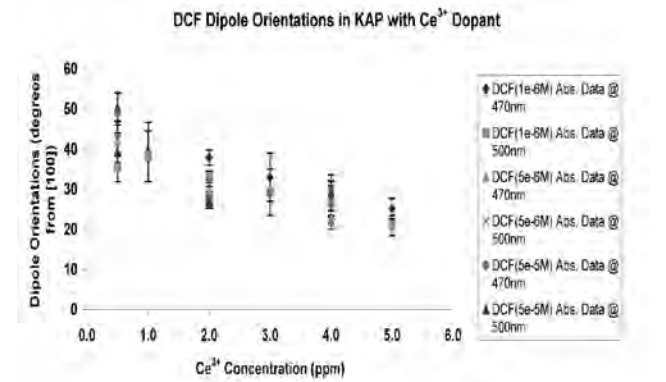

FIGURE 10. As the concentration of Ce^{3+} increases the dipole angle decreases towards the a-axis.

approximately 25° at 5.0ppm Ce^{3+}. It was additionally observed that this trend is independent of DCF concentration; the orientation angles were not affected by the increased concentration of dye. As stated earlier, Ce^{3+} blocks the +*c* kink site, and as a result this forces the dye into the –*c* kink site or along the step edge. The inclusion of dye in the Ce^{3+} crystals was very noticeable. The large amount of dye incorporated into the crystals lead us to surmise that there is no competition between Ce^{3+} and DCF for the +*c* kink site, and that the –*c* kink is the preferred site for DCF to incorporate itself into the crystal lattice. In fact, it was observed that more DCF goes into the crystal with the presence of Ce^{3+} than without it, indicating that the morphology changes to the hillocks potentially create even more –*c* kink sites for the DCF to bind. In addition, when the Ce^{3+} concentration increased passed a critical point the crystal habit also changed, although not as drastically as with the Fe^{3+}; the crystals became long and thin.

The DCF transition dipole moment orientations for both impurities and the interpretations of the data were supported by modeling once again done by Theresa Bullard. The modeling showed that indeed the kink sites are more energetically favorable for docking a DCF molecule than was the step edge. It also predicted dye orientation angles for the +*c* kink site to be 64 +/- 8° from the *a*-axis, the –*c* kink site gave 25 +/- 8° from the *a*-axis, and for the step edge it was 39 +/- 3° from the *a*-axis. These predicted values were used to help interpret the summary orientation plots for both impurities. Specifically, the dipole orientations from the Ce^{3+} data approaching closer to the *a*-axis as the impurity concentration increases, ultimately reaching an orientation of about 25°. This changing dye orientation, however, is in the opposite direction as would be expected if the transition dipole moment were aligned with the fast step edge, as Ce^{3+} misorients the steps towards the *c*-axis. This suggests that dye orientation is not driven by step misorientation as originally hypothesized. Rather, it indicates an increasingly greater DCF incorporation into the –*c* kink site. The Fe^{3+} data, on the other hand, was interpreted to be the result of an averaging between the orientations adopted from the dye going into the straight step edge with a little +*c* kink integration.[8]

Conclusion

From all methods of analysis, there was a clear competition between Fe^{3+} and DCF, and an almost cooperative effect between the Ce^{3+} and DCF, all indicating that DCF prefers the –*c* kink site. In general, a kink site is chemically specific and a favored growth site because it results in a minimal change of surface free energy upon addition of a new unit. In KAP, the (010) kink sites are non-equivalent and chemically specific due to the polar *c*-axis. The selective recognition of DCF for the –*c* kink sites demonstrates high chemical specificity of dye inclusion. Arriving at these conclusions required the combined use of many experimental methods along with computer modeling to justify the inferred interpretations. *Direct* observation and confirmation of these conclusions would require high precision, *in situ* observation with an atomic force microscope coupled to a confocal luminescence microscope, in order to obtain a real-time look at the development of KAP hillocks doped with Ce^{3+}, Fe^{3+}, and DCF. The question of how dye becomes incorporated into a model crystal system may not have been directly answered; however, there is strong evidence for highly specific chemical interactions at a growing surface that are a very important part of how the dye becomes incorporated within the fast slope of KAP hillocks.

References

1. Kahr, B. Gurney, G.W.; *Dyeing Crystals;* Chemical Reviews, 101 (2001), 893-951.
2. Hottenhuis, M.H.J.; Lucasius, C.B.; *Crystal Growth*, 78 (1986) 379-388.
3. Hull, D.; Bacon, D.J.; *Introduction to Dislocations*; Butterworth-Heinmann, Oxford, 2001
4. Bullard, T.; Kurimoto, M.; Avagyan, S.; Jang, S. H.; Kahr, B.; *American Crystallographic Association*©, 39 (2004) 62-72
5. Hottenuis, M.H.J.; Luscasius, C.B.; *Crystal Growth*, 94 (1989) 708-720.
6. Bullard, T.; Freudenthal, J.; Avagyan, S.; Kahr, B.; *Faraday Discuss.,* 2007, **DOI**; 10.1039/b616612c
7. Accelrys, *Materials Studio Getting Started, Release 4.0*, Accelrys Software, Inc.; San Diego, 2006.
8. Unpublished work to be submitted for publication in a month.
9. Hottenuis, M.H.J.; Oudenampsen, A.; *Crystal Growth,* 92 (1988) 513-529.

Acknowledgments

Special thanks to my mentor Theresa Bullard, Kristin Wustholz, Professor Bart Kahr, CMDITR (DMR-0120967), and the NSF for supporting the Hooked on Photonics program (CHE-0453596)

MIRANDA E. ROBERTSON. Miranda plans to obtain a BS in biochemistry and pursue a master's degree in the same field.

Optimization of the Deposition of Aluminum Electrodes

onto Organic Thin Films for Solar Cells Using E-Beam Deposition

MATTHEW RODY, William Potscavage and Bernard Kippelen
Center for Organic Photonics and Electronics (COPE), School of ECE, Georgia Institute of Technology

1. Introduction

Solar cells made with organic semiconductors rather than inorganic semiconductors (such as silicon) have been of growing interest in the scientific community. Organic semiconductors can be solution-processed and therefore can be used to fabricate organic photovoltaic devices that are extremely thin, flexible and potentially more cost-effective than silicon-based solar cells. In terms of efficiency, organic solar cells still fall short of their silicon-based counterparts, though improvements are continuously being made through research.

There presently exist several architectures for making organic solar cells that are commonly used in experimentation. Of these architectures, those that utilize the dispersed heterojunction structure have shown to be promising in terms of delivering high power conversion efficiencies.[1] The dispersed heterojunction combines both hole and electron transport semiconductors in a solution before processing that solution into a film, usually by spin-coating. The resulting film is then a blend of the two semiconductors that has many closely spaced heterojunctions dispersed throughout the film. Excitons created by absorbed light can separate into free carriers at the interface of the heterojunctions to generate a photocurrent in the solar cell.

The solar cells used in this experiment utilized this structure using poly(3-hexylthiophene) (P3HT) and [6,6]-phenyl C_{61} butyric acid methyl ester (PCBM) as the electron donor (electron transport) and acceptor (hole transport), respectively. Previous success was met with the P3HT:PCBM blend, and efficiencies have been reported as high as 5%. Indium tin oxide (ITO) is generally used as a transparent anode for these devices due to its relative transparency and low resistivity, and it is often purchased already on a glass substrate, directly from the manufacturer. Metals such as aluminum or silver are usually used as the cathode and are typically deposited on top of the active layer by thermal physical vapor deposition (PVD) under vacuum. An alternative to thermal PVD is electron-beam (e-beam) PVD, which has the benefit of being able to evaporate a substance without it being contaminated by material from the crucible that holds it.

Studies have shown, however, that device performance is dependant on some metal deposition parameters.[†] Because the metal cathode is deposited directly onto the organic layer, the nature of this interface can greatly affect the ohmic resistance of the interface. An increased resistance will limit the short circuit current flow and therefore impact the device efficiency negatively. In a study done by Cho, et. al. the use of slower deposition rates in a thermal PVD system resulted in a greater interface resistance between the organic layer and deposited metal due to increased metal penetration.[6] Consequently, there is concern that similar results will be obtained using an e-beam system. Therefore, in this study we investigated the effects of different cathode deposition rates used in e-beam evaporation on the efficiency of P3HT:PCBM solar cells in an effort to determine an optimal deposition rate.

2. Experimental

Photovoltaic devices used for this experiment were created on an ITO-coated glass substrate, spin-coated with poly(3,4-ethylenedioxythiophene): poly(styrene sulfonate) (PEDOT:PSS) (H.C. Starck, Baytron P VP AI 4083), and were composed of a P3HT (Rieke Metals, 4002E) and PCBM (Solenne BV) (see FIG. 1(a)) dispersed heterojunction topped with an Al metal cathode, giving an overall geometry of ITO/PEDOT:PSS/P3HT:PCBM/Al which can be seen in Figure 1(b). Before making depositions, the ITO was patterned with either a chemical vapor etch or a SiO deposition, and the ITO substrates were cleaned with a series of ultra sonic baths (detergent water, deionized water, acetone, and isopropyl alcohol for 20 minutes each) followed by an air plasma treatment for 2 minutes.

Samples were then spin-coated with a thin layer of PEDOT:PSS (1 minute at 5000 rpm) and subsequently annealed (10 minutes at 140 °C) before being loaded into a nitrogen-filled glovebox. A mixture of P3HT:PCBM in chlorobenzene (1.0:0.8 by weight at 18mg/ml)[4] was then spin-coated onto the samples after being stirred for two days. Samples were transferred to an e-beam vacuum deposition system where 150 nm of Al was deposited through a shadow mask to form five discrete devices per substrate, the average device area being 0.11 ± 0.01 cm^2. Al was deposited under a vacuum of $< 2 \times 10^{-6}$ torr at rates of 0.2, 0.5, 1.0, 1.5, 2.0, and 5.0 Å/s. After Al deposition, samples were annealed in the glovebox for 30 minutes at 115 ° C, 125 °C, or 135 °C to confirm the optimum annealing temperature.

Due to limited fabrication capabilities, devices were made in three different rounds. The same mixture of P3HT:PCBM was used in making the first two rounds of devices (with 12 days elapsed between the rounds), and a second mixture was made for the third round, using the exact same recipe.

---

[1] Power conversion efficiency, or the maximum output power divided by the input power, is the main factor by which solar cells are compared.

[†] Both of these methods merely pattern the ITO and do not affect the metal cathode interface, which is the subject of this experiment. Confirmation of this detail was given in that results from the SiO-coated v. etched ITO were extremely close in parallel experiments.

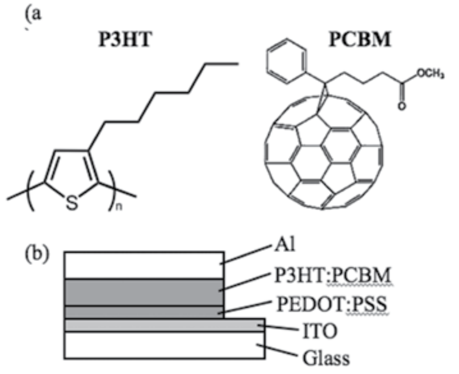

FIGURE 1. (a) Chemical structures for the organic semiconductors used in this experiment. (b) Schematic of device structure used in this experiment.

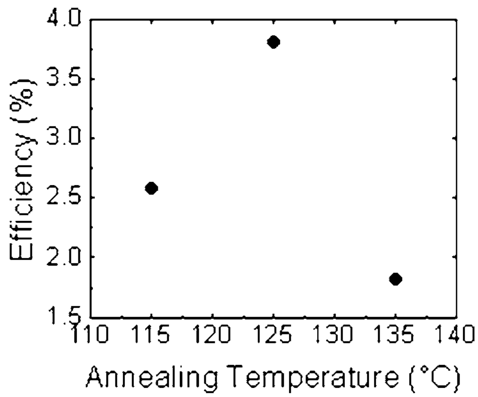

FIGURE 2. Device efficiencies with post-production annealing at different temperatures. All samples had Al cathodes deposited at 1 Å/s and were annealed for 30 minutes post-production. Efficiencies are averages for 5 devices.

Devices were tested in a glovebox, illuminated by broadband light from a filtered Xe lamp (CVI ASB-XE-175EX, 350-900nm) with an irradiance I_L of 86 ± 1 mW/cm2. Light intensity was measured using a calibrated silicon solar cell. Data were collected using a Keithley 2400-LV source meter.

3. Results and Discussion

The recipe for the solar cells used in this experiment calls for a P3HT:PCBM weight-ratio of 1.0:0.8 rather than 1:1 for the dispersed heterojunction because, as suggested by Ma, et. al.[4], an excessive amount of PCBM leads to decreased device performance due to "overgrown" PCBM crystals from annealing. Previous testing, however, suggested an ideal post-production (after Al deposition) annealing temperature of ~125 °C rather than the 150 °C suggested by Ma, et. al. (See FIG. 2). Samples on which Al was deposited at 1 Å/s were annealed for 30 minutes at 115, 125 and 135 °C before testing. Resulting efficiencies, averaged for 5 devices, were 2.6 ± 0.1, 3.8 ± 0.4 and 1.8 ± 0.1%, respectively. Though further testing is necessary before drawing conclusions, 125 °C was chosen as the post-production annealing temperature.

In a similar study, samples on which Al was deposited at 1.5 Å/s were annealed at 125 °C for periods of 0, 1, 5, 10 and 30 minutes in order to determine optimal annealing time. Resulting efficiencies (0.016 ± 0.003, 1.5 ± 0.1, 2.1 ± 0.2, 2.3 ± 0.1 and 2.4 ± 0.1, respectively) showed the optimal post-production annealing time to be 30 minutes, in agreement with Ma, et. al.[4] (see FIG. 3).

Figure 4 shows the efficiency of the devices made with respect to the rate of Al deposition in an e-beam deposition system. Al was deposited at rates of 0.2, 0.5, 1.0, 1.5, 2.0 and 5.0 Å/s. Measured efficiencies for these devices can be found in Table I. With the exception of the two empty points, there is a clear upward trend with improving efficiencies as the Al deposition rate increases. This is consistent with the findings of Cho, et. al.[6] which show improved device performance with higher deposition rates of metal onto organic thin films. Though the maximum device efficiency was achieved at 5.0 Å/s, device efficiency increasing with deposition rate appeared to be continuing at this point and there were no faster rates tested. This leaves room to believe that higher deposition rates yet could result in even higher device efficiencies, though at a point current needed to achieve these faster rates while using an e-beam PVD system would become a limiting factor.

Upon examining the lower part of the trend, there appears to be a critical cutoff point at ~1.0 Å/s where any Al depositions made at a slower rate lead to significantly reduced performance. The reason for the characteristics of this trend are yet uncertain, though it is a good possibility that the effect being studied is that noticed by Cho, et. al.[6] – namely that at lower deposition rates, metal atoms are more easily able to penetrate the thin organic film, leading to poorer interface quality. Electron microscopy technology could confirm this hypothesis, but as of yet definitive images have not been obtained.

As previously noted, the empty data points hitherto ignored reflect devices that were made with a mixture of organic materials that was the same as the others but that had been left to mix for an additional 12 days. Initially this discrepancy was not thought to make a difference, but after compiling all results, they seemed to suggest a difference in performance due to an increased time period between making the organic mixture and depositing it onto devices. Evidence for this can be demonstrated by comparing data collected at overlapping deposition rates. Devices made from mixture 1 and left to stir only 2 days performed 9% better than those of mixture 2, also left to stir for 2 days. However, devices made from mixture 1 that were left to stir for 14 days performed on average 36% *worse* than devices from mixture 2 left to stir only 2 days. These comparisons suggest that while the difference between the two mixtures was negligible, the amount of time the organic material was left in its chlorobenzene mixture significantly impacted device performance. The conclusion that must be drawn then is that after preparing a mixture of P3HT:PCBM in chlorobenzene, at some point the material begins to degrade in quality. The nature of this degradation remains unknown, although further testing could grant a better understanding.

4. Conclusion

In conclusion, post-production annealing conditions for solar cells that employ the P3HT:PCBM dispersed heterojunction were optimized to be 30 minutes at 125 °C. Then, using this optimized annealing metal cathode deposition onto a thin-film P3HT:PCBM dispersed heterojunction using an e-beam deposition system was optimized at a rate of 5.0 Å/s, though faster deposition rates could result in even higher efficiencies. Devices made with Al deposited at a lower rate perform comparably well, though at rates below 1.0 Å/s device performance decreases rapidly. Aside from deposition rates, it was also observed that devices made with organic material that had been in mixture form for an extended period of time performed significantly worse than those made with a fresher organic mixture. This suggests that P3HT:PCBM degrades when left mixed in chlorobenzene.

Acknowledgements

This research was made possible by the help and guidance of William Potscavage as well as Bernard Kippelen and the Kippelen Research Group. Funds for this research were provided by the Center on Materials and Devices for Information Technology Research (CMDITR), and the NSF Science and Technology Center No. DMR 0120967.

References

1. C. J. Brabec, Sol. En. Mat. 83, 273 (2004).
2. G. Yu, J. Gao, J. C. Hummelen, F. Wudl, and A. J. Heeger, Science. 270, 1789 (1995).
3. S. E. Shaheen, C. J. Brabec, N. S. Sariciftci, F. Padinger, T. Fromherz, and J. C. Hummelen, Appl. Phys. Lett. 78, 841 (2001).
4. W. Ma, C. Yang, X. Gong, K. Lee, and A. J. Heeger, Adv. Funct. Mater. 15, 1617 (2005).
5. S. Schiller, U. Heisig, and S. Panzer, Electron Beam Technology, John Wiley & Sons (1982).
6. J. H. Cho, D. H. Kim, Y. Jang, W. H. Lee, K. Ihm, J. Han, S. Chung, and K. Cho, App. Phys. Let. 89, 132101 (2006).
7. A. C. Dürr, F. Schreiber, M. Kelsch, H. D. Carstanjen, H. Dosch, and O. H. Seeck, J. App. Phys. 93, 5201 (2003).

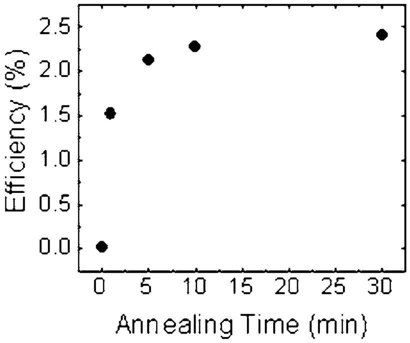

FIGURE 3. Device efficiencies with post-production annealing for different amounts of time. All samples had Al cathodes deposited at 1.5 Å/s and were annealed for 30 minutes post-production. Efficiencies are averages for 5 devices.

Mixture	Days Stirring	Al Deposition Rate (Å/s)	Efficiency (%)
1	2	0.2	0.1 ± 0.1*
1	2	0.5	3.5 ± 0.4*
1	2	1.0	3.8 ± 0.3*
1	14	1.5	2.5 ± 0.1*
1	14	2.0	2.6 ± 0.1*
2	2	1.0	3.5 ± 0.6*
2	2	1.5	4.1 ± 0.4*
2	2	2.0	3.9 ± 0.1†
2	2	5.0	4.4 ± 0.1†

TABLE 1. Measured efficiencies for devices with Al cathodes deposited at different rates. Organic mixture and number of days it was left stirring are also indicated. * signifies efficiencies averaged for 10 devices while † signifies efficiencies averaged for 5 devices.

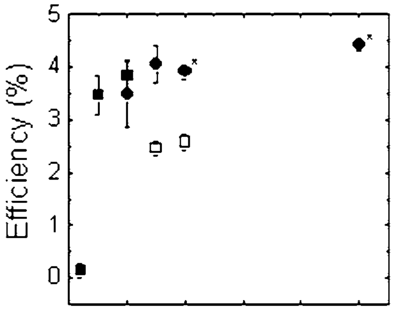

FIGURE 4. Efficiencies or devices with Al deposited at rates ranging from 0.2 to 5.0 Å/s. 3 trials using 2 different P3HT:PCBM mixtures (same recipe) were made for this experiment. Squares indicate mixture 1 while circles indicate mixture 2. Solid shapes indicate the organic mixture was spin-coated after 2 days of stirring while empty shapes signify a stirring period of 14 days. All post-production annealing was done for 30 min at 125 °C. All efficiencies are averages for 10 devices except for those marked * (5 devices).

MATTHEW RODY plans to graduate from Goshen College (Goshen, IN) in 2008 with a major in physics and a minor in music. After graduating, he hopes to seek fulfillment in life.

Syntheses of Two-Photon Dyes for Use in Precise Biological Stimulus Transfer

ISAAC E. STORMER, Joshua Davies
University of Washington

Introduction

The applications of two photon dyes are numerous. One of the more important possible uses is the possible transfer of drugs, medicines, or other chemicals into certain biological tissues or cells. Due to their highly lipid-soluble character, the chromophores made in this project could be readily associated to biological structures which contain lipid bilayers as membranes. Included into the walls of microscopic vesicles (diameters usually around 100-700nm) containing a biological stimulus, the dye can be used to release those contents. Once the vesicles containing the drugs are bonded to the tissue, the vesicles can then be opened by irradiating the biological structure with long wavelength (and thus low energy) light using a laser nanopulse. The two photon dye will then absorb the photons of radiating infrared (IR) light and cause the vesicle to explode and thus release its contents. Precise release of the stimulus can be attained using the focal point of the laser as only at this point is there enough energy to activate the dye. Thus the stimulus is only released near the target tissue rather than dispersed over a large area where it may come into contact and damage other cells. By using this method stronger, more potent stimuli may be used without damaging nearby healthy tissue. Due to absorbance of IR radiation rather than high energy radiation, damage is not done by the laser to the biological tissues and a much better penetration can be acquired as IR travels much deeper through tissue than does high energy light such as UV (ultraviolet).

Results and Discussion

Synthesis.

The chromophores were synthesized according to experimental techniques researched in the literature.

3-{4-[Bis-(4-hydroxy-phenyl)-amino]-phenyl}-2-[4-(2-{4-[bis-(4-hydroxy-phenyl)-amino]-phenyl}-1-cyano-vinyl)-phenyl]-acrylonitrile (P-1) (JD2051 formed earlier in different project)

0.700g (0.89mmoles) JD2051 dissolved in 35mL DCM (dichloromethane) and brought to 0oC in ice bath. 10.7mL (10.7mmoles) boron tribromide added dropwise. Stirred in ice bath for 3hrs. Extracted with ethyl acetate. Purified by column chromatography (15% ethyl acetate in hexane). Yield: 0.526g (81.2%). see **Scheme 1.**

(P-2) 0.794g (1.09mmoles) of **(P-1)** combined with 0.362g (9.05mmoles) sodium hydride and 0.062g (0.37 mmoles) potassium iodide and flushed with argon gas. Mixed for ten minutes then added 4.097g (9.81 mmoles) 11-bromomethyl-tricosane and heated @80°C for 14hrs. Then extracted with DCM and purified using column chromatography (15% ethyl acetate in hexane). Yield: 0.555g (24.5%). see **Scheme 1.** ^{1}H NMR (500MHz, TMS, $CDCL_3$) δ: 0.881 (t, 12H), 1.265 (m, 80H), 1.776 (m, 2H), 3.827 (d, 4H), 6.879 (d, 4H), 6.901 (d, 2H), 7.103 (d, 4H), 7.428 (s, 1H), 7.666 (s, 2H), 7.747 (d, 2H).

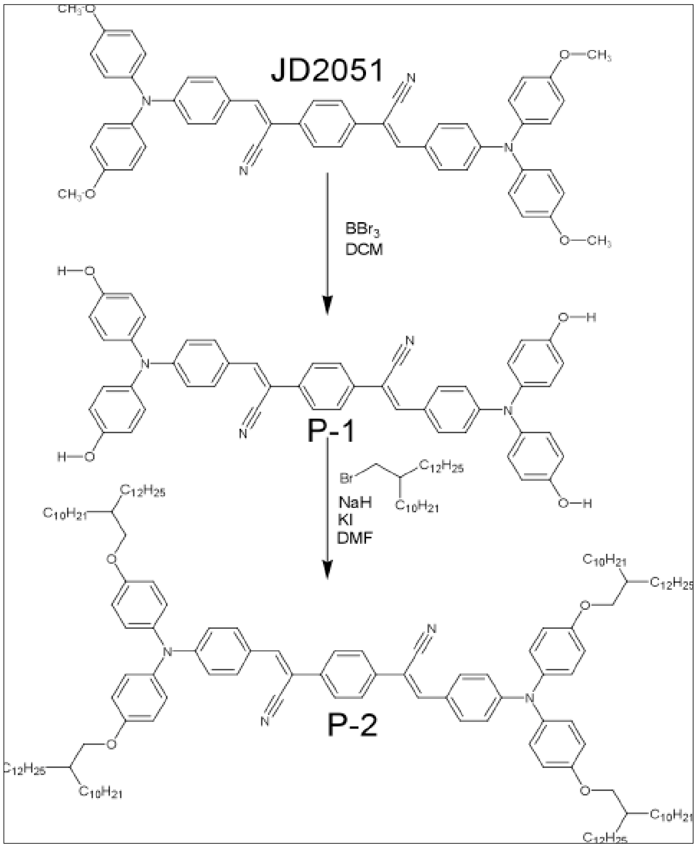

SCHEME 1. Synthesis of Chromophore 1

4-[Bis-(4-hydroxy-phenyl)-amino]-benzaldehyde (P-3) (JD2013 formed previously for use in a different project) 1.551g (4.65mmoles) JD2013 dissolved in 60mL DCM. Brought to 0°C in an ice bath then added 27.9mL (27.9mmoles) boron tribromide dropwise. Stirred in ice bath for 3hrs. Extracted with ethyl acetate. Purified using silicon plug. Yield: 1.978g (135%). See **Scheme 2**. (appeared pure from TLC despite impossible yield). ^{1}H NMR (500MHz, TMS, $CDCL_3$) δ: 5.301 (s, 1H), 6.828 (d, 4H), 6.860 (d, 2H), 6.891 (d, 4H), 7.615 (d, 2H), 9.750 (s, 1H)

4-{Bis-[4-(2-decyl-tetradecyloxy)-phenyl]-amino}-benzaldehyde (P-4) 0.183g (0.60mmoles) of **(P-3)** dissolved in 5mL dry acetone and combined with 1.564g (11.32mmoles) potassium carbonate and heated for 30min at 75°C. Then, 0.752g (1.80mmoles) 11-bromomethyl-tricosane was added and refluxed for 13 hrs. Product was then extracted using DCM and run through a column chromatograph to purify (15% ethyl acetate in hexane). Yield: 0.391g (66.7%). See **Scheme 2.** ^{1}H NMR (500MHz, TMS, $CDCL_3$) δ: 0.879 (t, 12H), 1.263 (m, 80H), 1.750 (m, 2H), 3.815 (d, 4H), 6.828 (d, 4H), 6.860 (d, 2H), 6.891 (d, 4H), 7.615 (d, 2H), 9.750 (s, 1H)

2,5-Dimethyl-terephthalonitrile (P-5) 25.000g (94.71mmoles) 1,4-Dibromo-2,5-dimethyl-benzene was combined with 25.4g (283.61mmoles) copper cyanide and reflux in DMF for 2 days. Mixture was then washed with 1.5L ammonia solution (15% by weight) and white precipitate was collected and washed with another 1.5L ammonia solution. Solid washed again with 1.5L water then dried in desiccator. Solid then extracted in hot acetone in Soxhlet apparatus using 200mL dry acetone. Finally ran through silicon plug using pure DCM. Yield: 14.792g (82.9%). See **Scheme 2.**

2,5-Bis-bromomethyl-terephthalonitrile (P-6) 12.06g (77.22mmoles) **(P-5)** was added combined with 0.107g (0.77mmoles) benzoyl peroxide and 34.370g (193.11mmoles) n-bromosuccinimide in flask and dissolved solids in 300mL carbon tetrachloride. Solution was refluxed for 4 days and followed by TLC. Once reaction reached completion the precipitate was filtered off at room temperature and then filtrate was rotovaped to remove solvent. (**P-6**) was then purified by column chromatography (15%ethyl acetate in hexane) and recrystallized in boiling ethyl acetate/hexane (60% ethyl acetate). Yield: 0.790g (3.26%). See **Scheme 2.** ^{1}H NMR (500MHz, TMS, $CDCL_3$) δ: 4.611 (s, 2H), 7.861 (s, 1H).

[2,5-Dicyano-4-(diethoxy-phosphorylmethyl)-benzyl]-phosphonic acid diethyl ester (P-7) 0.790g (2.52mmoles) **(P-6)** was combined with 1.20mL (7.55mmoles) triethyl phosphite and heated at 160°C for 12hours. Excess phosphite was removed using vacuum. Yield: 4.70g (43.5%). See **Scheme 2.** ^{1}H NMR (500MHz, TMS, $CDCL_3$) δ: 1.298 (t, 6H), 3.381 (s, 2H), 4.124 (m, 4H), 7.802 (dd, 1H).

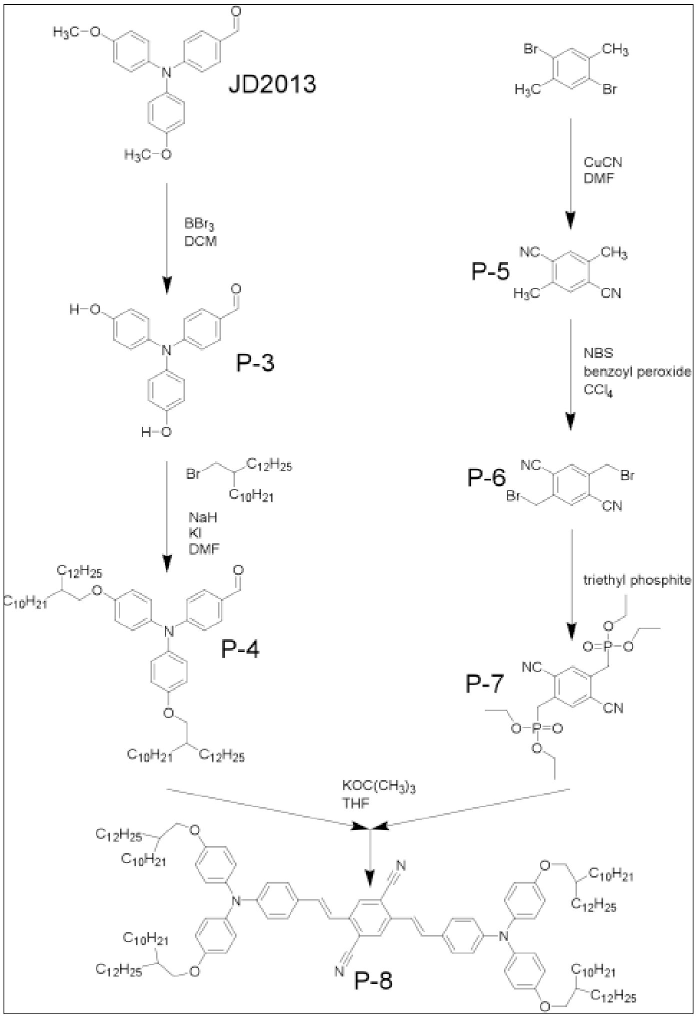

SCHEME 2. Synthesis of Chromophore 2

(P-8) 0.075g (0.24mmoles) (P-7) and 0.441g (0.45mmoles) (P-4) were combined in a flask and stirred with 0.5mL potassium *t*-butoxide. This was dissolved in 2mL THF (tetrahydrofuran), and stirred for 30min. Solution was extracted first with DCM and then hexanes. Compound was purified using column chromatography (15% ethyl acetate in hexane). Yield: 0.471g (95.0%). 1H NMR (500MHz, TMS, CDCL3) δ: 1.263 (t, 12H), 1.331 (m, 80H), 1.767 (m, 2H), 3.813 (d, 4H), 6.839 (d, 4H), 6.856 (d, 2H), 7.076 (d, 4H), 7.163 (s, 2H), 7.366 (d, 2H), 7.957 (s, 1H).

Data

Ultraviolet/Visible light Spectroscopy was performed and spectrum of both chromophores was collected and compared (see graph on facing page).

From the UV/vis spectrum (**Figure 1**), a definite red shift can be seen in the absorbed wavelength. Although this tells nothing of the dye's performance, it shows that the second dye **(P-8)**, which is expected to be much better than the first **(P-2)**, already has an advantage over the first.

$E = h\nu$ and $\lambda\nu = c$ so $E = \frac{hc}{\lambda}$

Since low energy light is desired, a longer wavelength absorbed would be better for the projected applications (energy is inversely proportional to wavelength).

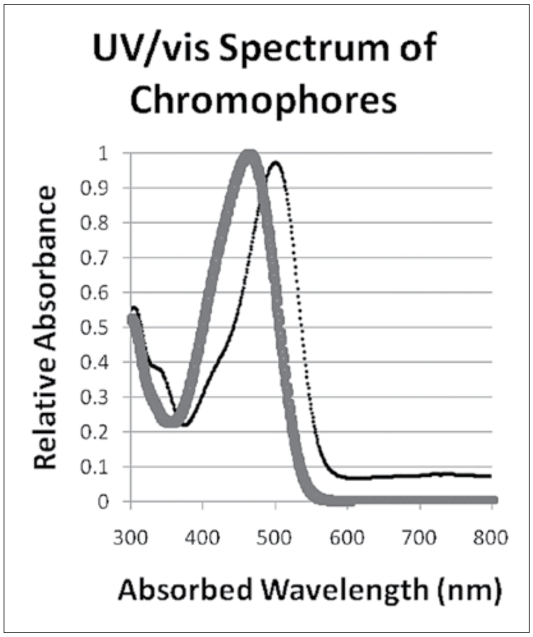

FIGURE 1. UV/vis spectrum of chromophores [thin, dashed line is second chromophore (P-8)]

Conclusions

From this project two dyes were formed for the use of biological stimulus transfer. Once testing has been completed, these dyes have the ability to revolutionize biological stimulus transfer.

Acknowledgements

I, the author, thank the Dalton Group at the University of Washington for accepting me into their lab. I look forward to continuing working with them throughout my education. I thank graduate student Joshua Davies for his time and helping me so much with this project. Josh spent a lot of time showing me synthetic and purification techniques. Also, Dr. Phil Sullivan for accepting me into the lab and being my official mentor. I thank the Hooked on Photonics REU staff for this excellent summer research opportunity. Funding for this program is provided by the NSF in the form of two grants with the numbers: DMR-0120967 and CHE-0453596

References

1. One- and Two-Photon Spectroscopy of Donor-Acceptor-Donor Distyrylbenzene Derivatives: Effect of Cyano Substitution and Distortion from Planarity *J. Phys. Chem. A* 2002, 106, 11470-11480

ISAAC STORMER

Polythiophene-based Organic Field-Effect Transistors

RANBEL SUN,[1]* Benoit Domercq,[1] Shannon Watt,[2] Xiaohong Zhang,[1] David Collard,[2] Bernard Kippelen[1]
Center for Organic Photonics and Electronics (COPE),[1] School of Electrical and Computer Engineering & [2] School of Chemistry and Biochemistry,
Georgia Institute of Technology, Atlanta, GA 30332 * Home Institution: Massachusetts Institute of Technology

Introduction

Technologies using organic semiconductors have attracted significant research interest in recent decades due to their potential as a low-cost, structurally flexible alternative to traditional technologies using inorganic semiconductors such as silicon (Si). In particular, organic materials are being used as the semiconducting layer in thin film transistors (TFTs). Because of the low processing temperature required to fabricate organic thin films, they are compatible with flexible plastic substrates.[1] In addition, the potential to process organic materials from solution opens up the possibility for large area devices via cost-effective manufacturing methods such as ink-jet printing deposition. Applications can include flexible electronic displays, radio-frequency identification tags (RFIDs), and photosensors.

Currently, the best charge carrier mobilities measured for organic semiconductors (as seen in pentacene) are of the same order of magnitude than amorphous silicon (around 1 $cm^2/V.s$). However, wet-processed organic semiconductors still exhibit mobilities that are 1 or more orders of magnitude smaller. In general, lower mobility in organic materials is attributed to the inherently different mechanism of carrier transport and the weak intermolecular bonds in organic compounds.[2] Another important organic field-effect transistor (OFET) limitation is that environmental conditions such as atmosphere and light induce carrier traps in the organic semiconductor, reducing the mobility and degrading the device. In addressing these limitations, polythiophene semiconductor films have been widely studied due to their high crystallinity and relative air stability under operation. Various polythiophene OFETs have been shown to possess large crystalline domains[3,4] that would facilitate charge carrier transport and lead to higher mobility. Values of up to 0.7 $cm^2/V.s$ have been reported,[3] which are comparable to mobilities for vacuum deposited pentacene.

This research focused on studying newly synthesized polythiophene copolymers (Figure 1) as a potential semiconductor for OFETs. The three different compounds we worked with differed in the lengths of their alkyl and fluorine side chains.

Like in other polythiophenes, the planar ϖ-electron network strengthens intermolecular bonds and results in more rigid crystalline structures. The fluorine chains, however, are particularly interesting because they can potentially segregate and self-align during deposition and further reduce carrier scattering. We hope to fabricate high performance transistors by developing these new materials, optimizing fabrication and processing steps, and investigating self-assembled monolayer (SAM) interfaces.

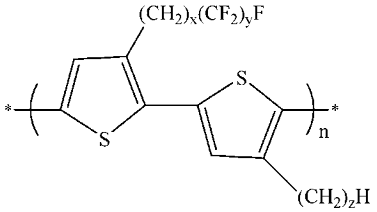

FIGURE 1. Polythiophene (x,y/z)Polythiophene (5,4/12), (5,4/8), and (11,4/8) were investigated, differing in the lengths of their alkyl and fluoro substituents.

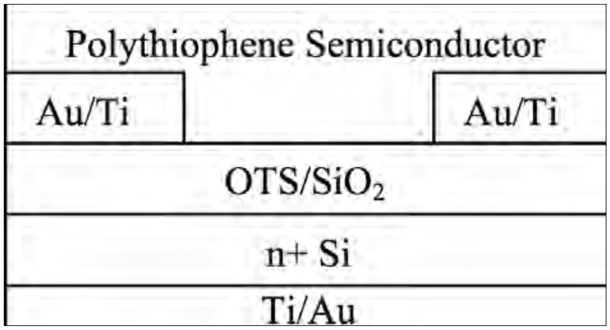

FIGURE 2. Composition of experimental OFETs in bottom-contact configuration.

Experimental Methods

Device Fabrication: The OFETs fabricated for this research were in bottom-contact configuration. (Figure 2) A heavily n-doped Si wafer (550 µm) served as both the substrate and the gate electrode, through which voltage could be applied to control the flow of current between the source and drain contacts. The back of the Si was coated with a thin layer of titanium (10 nm) as an adhesion layer for gold (100 nm). Since polythiophene is known to be of p-type (hole-conducting), we used a high workfunction metal for improved hole injection. A 200 nm thick SiO_2 insulator was thermally grown on top of the Si. A thicker insulating layer (or one with a lower dielectric constant) is more effective at reducing gate leakage, but it also inhibits the driving ability of the transistor. Ti/Au (5 nm/100 nm) source and drain contacts were patterned over the dielectric surface using photolithography and a lift-off process. The chips were cleaned extensively in an ultrasonic bath with detergent water, deionized water, acetone, and ethanol. They then underwent 4 minutes of UV-ozone plasma treatment, immediately after which they were submersed overnight in a 0.4 w.t.%

octadecyltrichlorosilane(OTS)/toluene solution while in a nitrogen-filled glovebox (<3 ppm H_2O, <12 ppm O_2). OTS formed a self-assembled monolayer by eliminating surface hydroxyl groups which would otherwise trap electrons and inhibit device performance. The prepared chips were baked at 120°C for 30 minutes, cleaned with chloroform and ethanol, and dried on a hotplate.

The polythiophene was solubilized in 1,2-dichlorobenzene at a concentration of 0.25 mg/mL and dropcasted over the contacts in air. Spincoating would have produced a more uniform film, but we chose to dropcast because of the potential to lead to slower film formation and a higher degree of organization.

Phosphonic Acid Treatment: The phosphonic acid SAM procedure was similar to that for OTS. Substrates were cleaned by sonication and dried on a hotplate. Immediately following a 4-minute plasma etch, the substrate was submersed overnight in a 1mM solution of either alkylphosphonic acid (APA) or perfluoroalkylphosphonic acid (PFAPA) made with a 3:2 ratio of chloroform/ethanol as solvent. The solvent evaporated over time, leaving phosphonic acid molecules adsorbed to the substrate surface. Samples were baked at 140°C for 6-12 hours and underwent post-modification cleaning in ethanol. To verify SAM coverage, contact angle measurements were conducted to test the hydrophobicities of the treated surfaces.

Device Characterization: In a transistor, applying a certain bias to the gate electrode (V_{GS}) induces the formation of a charge carrier channel through the semiconducting layer, a phenomenon also known as the field effect.[1] A source-drain voltage potential (V_{DS}) results in the movement of these accumulated charges, or in other words an electric current, between the source and drain contacts. Organic semiconductors are usually intrinsically inclined to conduct either electrons or holes and greatly differ in their charge transport ability.

Testing took place in gloveboxes so that H_2O and O_2 would not interfere with device operation. The sample sat on an aluminum block with the gold backing adjacent to the aluminum. Electrical contacts were made to the gate (via the aluminum), source, and drain using a microprobe station and connected to a power source/monitor unit. To generate output curves, we measured the source-drain current (I_{DS}) as a function of V_{DS} for several discrete values of V_{GS}. For transfer measurements, we swept V_{GS} for fixed values of V_{DS}.

The field effect mobility (μ), threshold voltage (V_{TH}), and on/off current ratio (I_{ON}/I_{OFF}) are figures of merit that quantify OFET performance. In the saturation regime, the mobility can be calculated from the square law:

$$I_{DS} = \frac{W}{2L} C_i \mu (V_{GS} - V_{TH})^2$$

where W and L are the width and length of the semiconducting channel respectively, and C_i is the capacitance density of the SiO_2 insulator. The threshold voltage is the gate voltage necessary to induce mobile charges in this channel, or essentially, when I_{DS} is no longer zero. The on/off current ratio is the maximum over minimum I_{DS} as seen on the transfer curve, another useful characteristic that helps gauge the switching abilities of the device.

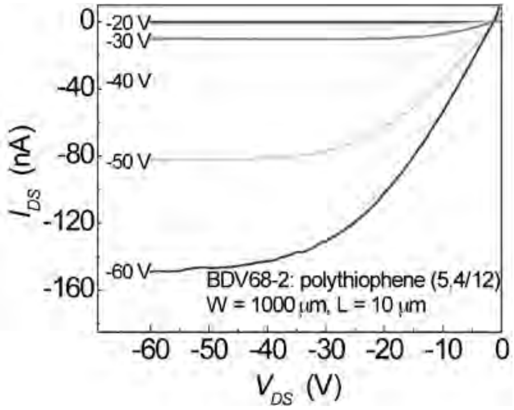

FIGURE 3. Output characteristics for a polythiophene (5,4/12) transistor with W = 1000 μm and L = 10 μm. The semiconductor is notably p-type, since negative voltage induces charge transport.

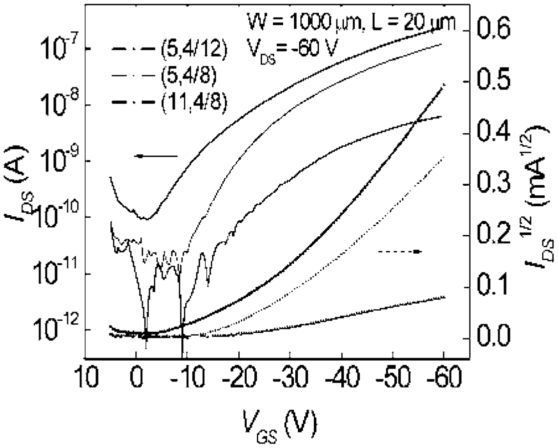

FIGURE 4. Transfer measurements for polythiophene (5,4/12), (5,4/8), and (11,4/8) devices with W=1000 μm and L=20 μm. The low mobility for the (11,4/8) device is attributed to its thicker semiconducting film.

Results and Discussion

Polythiophene OFETs: Figure 3 shows output curves, also known as I-V curves, for a polythiophene (5,4/12) transistor with W = 1000 μm and L =10 μm (W1000L10). We can see that the polythiophene semiconductor is of p-type because current increases with negative V_{DS} and V_{GS}. Typical OFET behavior is observed: The current increases with V_{GS}, and as V_{DS} is swept from 0 V to -60 V, it experiences a linear gain until eventually reaching a saturation value when the conducting channel becomes pinched-off by an insufficient potential between the gate and drain.

Having successfully made devices using this new copolymer, the three polythiophene compounds were compared by taking transfer measurements of transistors with the same channel dimensions. Figure 4 displays a semi-logarithmic plot of the source-drain current (I_{DS}) as a function of gate voltage (V_{GS}) and a plot of $I_{DS}^{1/2}$ for linear fitting purposes.

t=150 nm	L50	L20	L10	L5
W500	2.9×10^{-5} (-15.3)	4.1×10^{-6} (-33.1)	1.6×10^{-6} (-30.7)	4.3×10^{-7} (-31.9)
W1000	---	1.1×10^{-5} (-20.9)	2.6×10^{-6} (-34.7)	---
t=15 nm				
W500	1.4×10^{-3} (-13.1)	3.3×10^{-4} (-19.0)	1.6×10^{-4} (-21.3)	---
W1000	---	3.7×10^{-4} (-20.5)	3.7×10^{-4} (-27.7)	3.3×10^{-4} (-21.1)

TABLE 1. Mobility values (cm^2/V.s) and threshold voltages (V) for OFETs on two polythiophene (5,4/12) chips with different thicknesses, 15 and 150 nm. Columns correspond to channel lengths and rows to channel widths, as measured in microns.

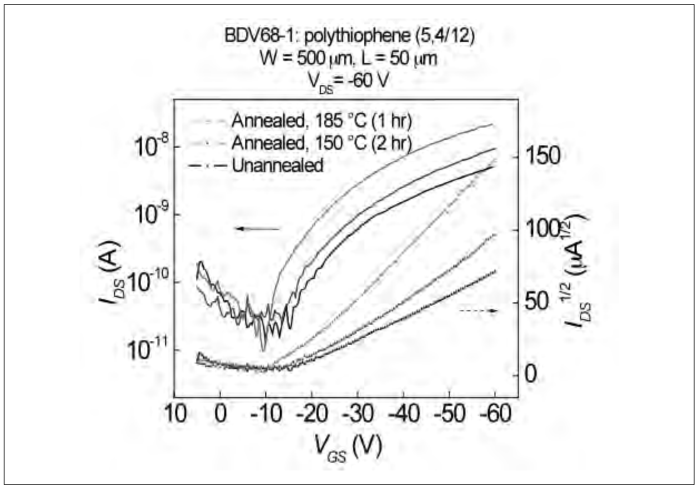

FIGURE 5. Transfer curves for a 150-nm, *W*=500 μm and *L*=50 μm polythiophene (5,4/12) transistor annealed at different temperatures. Annealing produced a noticeable improvement in mobility.

The polythiophene (5,4/12) gave the highest mobility, 3.3×10^{-4} cm^2/V.s., and (5,4/8) performed similarly with a mobility of 2.1×10^{-4} cm^2/V.s. However, a significantly lower mobility of 8.7×10^{-6} was measured for the (11,4/8) device. The (11,4/8) was found to have a film thickness of 100 nm, compared to 15 nm for the other two. The disparity in mobility may be attributed to the thickness difference rather than the inherent properties of the polymer. This is supported by the data in Table 1, which compared μ and V_{TH} for two (5,4/12) chips with different thicknesses, 15 and 150 nm, for the organic film.

Untreated	37°
APA	69°
PFAPA	79°
OTS	89°

TABLE 2. Contact angles for various SAMs on Si/SiO$_2$

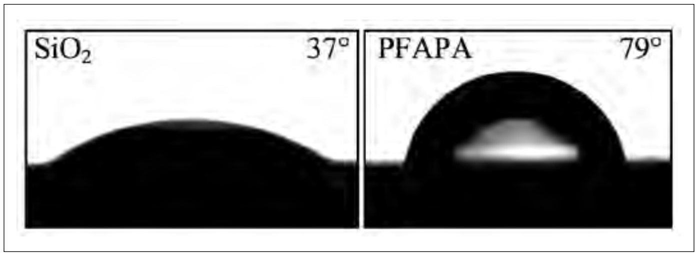

FIGURE 6. Graphical comparison of contact angle before and after the insulator surface is treated with a PFAPA SAM layer. PFAPA eliminates charge-trapping hydroxyl groups, leading to a more hydrophobic surface.

Higher mobilities were achieved with a thinner film, regardless of device geometry. The highest mobility value measured was 1.4×10^{-3} cm^2/V.s. Device geometry clearly had an effect on performance, where the best performing transistors had channel widths and lengths of 500 and 50 μm. According to the data, decreasing the length and width corresponded to decreased mobility for this device structure. Ideally, we would like to be able to decrease size without compromising performance. The threshold voltages were also quite high, which is impractical for low-voltage switching applications. I_{ON} / I_{OFF} was on the order of 10^3; it could be increased above its current value if the off-current could be decreased, usually by reducing environmental and measurement noise.

Fabrication/Processing Parameters: Thermal annealing was performed in order to improve film quality. The energy from heat lets the molecular groups move about more freely and in theory, allows the polymer side-chains to align more uniformly. The 150-nm thick (5,4/12) chip was first annealed to 150°C for 2 hours. After testing, it was annealed again, this time to 185°C for an hour. As shown in Figure 5, annealing produced noticeable improvement in mobility, with values increasing from 2.0×10^{-5} to 1.2×10^{-4} cm^2/V.s. Annealing the 15-nm chip to 185°C, however, caused a drop in performance. It is likely that the thinner film had different thermal properties, causing it to melt at lower temperatures than the thicker film.

In addition to controlling film thickness during fabrication, ensuring film continuity is fundamental to obtaining high quality electrical characteristics. A continuous film produced characteristic OFET output curves, whereas the current for a discontinuous film did not saturate. Also, after fabricating several devices, the polythiophene solution was found to degrade when kept in air. Freshly prepared solutions led to better performing OFETs than solutions stored in air for several days. For example, a *W*=1000 µm *L*=20 µm device made with a fresh (5,4/8) solution was found to have a mobility of $\mu = 2.1\times10^{-4}$ cm^2/V.s and a threshold voltage V_{TH}= -23 V. After 12 days, a device made with the same solution resulted in a mobility and threshold voltage of 1.2×10^{-5} cm^2/V.s and -44 V. After 27 days, no transistor behavior could be observed.

Fluorinated SAMs: Table 2 lists the contact angles measured for various SAM layers on Si/SiO$_2$ substrates. The fluorinated phosphonic acid (PFAPA) was confirmed as a more hydrophobic surface modifier than APA. PFAPA may be a good candidate for fabricating polythiophene OFETs because not only does it have a contact angle comparable to OTS, its fluorine molecules may assist with fluorine chain alignment in the semiconductor.

Conclusions

OFETs fabricated with these polythiophene derivatives achieved promising mobilities of up to 10^{-3} cm^2/V.s. Although the mobilities of these new compounds currently do not rival those of existing, high-quality polythiophenes, we have yet to fully explore the exploitation of their fluorine side-chains. Future work will involve fabricating OFETs with the fluorinated phosphonic acid SAM in hopes of creating a well-structure, ordered film. If liquid crystal formation is observed via x-ray crystallography, aligning the crystals may be another method of increasing mobility. Fabrication and processing procedures will certainly need to be optimized, such as improving deposition techniques, finding ideal annealing temperatures, and ensuring that the film is uniform and at an optimal thickness.

References

1. Newman, C. *et al. Chem. Mater.* 16, 4436 (2004)
2. Dimitrakopoulos, C. & Malenfant, P. *Adv. Mater.* 14, No. 2, Jan. 16 (2004)
3. McCulloch, I. *et al. Nat. Mater.* 5, 328-333 (2006)
4. Umeda, T. *et al. J. Appl. Phys.* 101, 054517 (2007)

Acknowledgements

This material is supported by the STC Program of the National Science Foundation No. DMR 012097. Special thanks go to Benoit Domercq, Xiaohong Zhang, Asha Sharma, and Dr. Bernard Kippelen for their support and guidance, and to Shannon Watt for her collaboration in this research.

RANBEL SUN is currently studying electrical engineering and computer science at MIT and plans on pursuing a Ph.D. upon graduation in 2010.

Improving the Power Conversion Efficiency

in Titanium Oxide/ Poly 3-Hexylthiophene Bi-layer Devices by Doping with Iron Nitrate

NATALIE A. WILHELM, Brown University
Dan Liu, Dr. Christine Luscombe, Materials Science and Engineering, University of Washington

Introduction

The motivation for this research is to create a bi-layer organic/inorganic solar cell device that is made more efficient by doping the inorganic layer with iron. In the most basic sense, solar cells convert light energy into electricity. In the current times, alternative energy sources are crucial as the earth's nonrenewable resources, such as fossil fuels, are being used up. Global warming is coming to the forefront of today's environmental concerns as the buildup of green house gases increases in the atmosphere. Solar energy offers an environmentally friendly solution to the growing energy crisis.

Although capturing solar energy is not a new idea, conventional solar panels are not affordable or transportable enough to be a viable option as a major power source. The current industrial solar cell is usually made of silicon, which is toxic and expensive to purify to a high enough quality for efficient use[1]. The silicon solar cells are also inflexible which is problematic for transportation and use in smaller devices. Alternative types of solar cells are being created using organic semiconductors, which are much lighter, thinner, and more flexible[2]. Organic semiconductors also have the potential to be a more economical solution as well[3]. Currently, organic solar cells are extremely inefficient and unstable compared to the silicon wafers. Organic solar cells are also unstable in an oxygen environment, and therefore this research must be done in an argon glove box until a suitable protective coating is created.

Solar cells work when photons strike the surface creating charged particles called excitons and then separate the charges and transport them to the two conductive electrodes, creating an electric current. Excitons consist of an electron and a positive 'hole' (fig. 1). The devices that are being constructed are composed of two semiconductors on top of indium tin oxide (ITO), which is a conductive substrate. The light energy is absorbed by the organic layer, poly 3-hexylthiophene (P3HT), which acts as the p-type semiconductor transferring the positive charge. The hole (h+) travels through the P3HT and into a silver cathode. The inorganic semiconductor is titanium oxide (TiO_2). Titanium oxide is used because the highest occupied molecular orbital (HOMO) of the P3HT corresponds well with the energy level of the valence band of the TiO_2. TiO_2 accepts the excited electrons from the P3HT and acts as an anode.

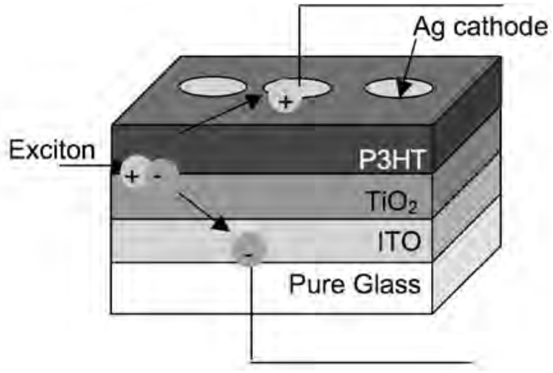

FIGURE 1. Organic/ Inorganic Bi-Layer solar device. A photon hits the device and an exciton is created at the interface of the P3HT/TiO_2 interface. Charge separation occurs and an electric current is produced.

Experimental
Cleaning and Preparation

ITO covered glass was sonicated in first Meri-suds and deionized water, second in pure deionized water, third in acetone, and forth in isopropyl alcohol. After the sonication the devices were dried with nitrogen gas and plasma cleaned with air for 10 minutes.

Inorganic layer: TiO_2

There were a few problems with the titania solution. The first recipe was a solution of titanium (IV) ethoxide, ethanol, deionized water, and hydrochloric acid in a ratio of 5:40:1:.4, respectively. The solution was made, but turned a translucent white, not clear. A new recipe was used that was simpler and had less room for error, which was used to make a working control device. The titania sol-gel was made by mixing anhydrous butanol with titanium (IV) isopropoxide (99.999%) at a 15 wt% ratio. The solution was allowed to mix for an hour, and then filtered. The ITO plated glass was spin coated with 65 μL of the sol-gel at 3,500 rpm for 60 seconds.

For the iron-doped sol-gel, a .05 atomic% of iron nitrate was weighed and added to the regular sol-gel. The solution appeared a dark yellow color. After an hour the solution was filtered into a clean vial. The devices were spin-coated with 65 μL at 3,500 rpm for 60 seconds.

After one hour of air-drying in a vented hood, the devices were calcinated in a furnace at 450° C for 30 minutes.

Organic Layer: P3HT

For each batch of devices made, two concentrations of P3HT were used: .5 wt% and .75 wt%. The P3HT was weighed and added to a septum sealed vial. Anhydrous chlorobenzene was used as the solvent. After the chlorobenzene was added, the vials were purged with nitrogen and wrapped in foil to keep out any light. The solution was allowed to mix for 3-4 hours at 45° C in a water bath.

The devices were sonicated for 5 minutes with isopropyl alcohol, and then plasma cleaned with O_2 for 1 minute. All material was now transferred into an argon glove box. The P3HT solutions were filtered into fresh vials. The devices were spin-coated at 1000 rpm with 65 µL of the P3HT solution. The devices were then annealed at 140° C for 15 minutes.

Silver Electrodes

The electrodes were deposited in a nitrogen deposition chamber. The final thickness was 85 nm. The devices were stored in an argon glove box until tested (fig. 2).

Testing

The devices were tested by connecting a circuit and applying a 1000 W light source that simulates the solar spectrum and power. The power conversion efficiency, fill factor, short circuit current (I_{sc}), and open circuit voltage (V_{oc}) were recorded. The short circuit current is the maximum current flowing through the device when there is no external resistance. The open circuit voltage is the internal electric potential difference. The maximum power output the device gives is shown in figure 3 as being the maximum 'area' of voltage and current density. The fill factor is a ratio of the maximum power divided by the $I_{sc} \times V_{oc}$. The power conversion efficiency is the maximum power divided by the sun's power on the particular device.

Results and Discussion

Currently, only one successful control device has been produced. No iron-doped devices were created in the batch, so no conclusions can be drawn about the iron-doped devices. The data from the best three electrodes from the device are listed in table 1. The best curve is shown in figure 4.

The highest PCE was the first electrode tested, and as the devices were exposed to air, they degraded and the PCE decreased.

There have been many problems with creating the control devices. A P3HT concentration study was done to see if it had an effect on the low current, but it did not. The best cells still came from the .5% and .75% P3HT concentrations, but still had extremely low currents (10^{-7} amperes). Next, a study on the thickness of the titania layer was done. The sol-gel was spin-coated at 1000, 2000, 4000, and 6000 rpm. The best devices were those at 2K and 4K, which makes sense because we had started out spinning the sol-gel at 3.5K.

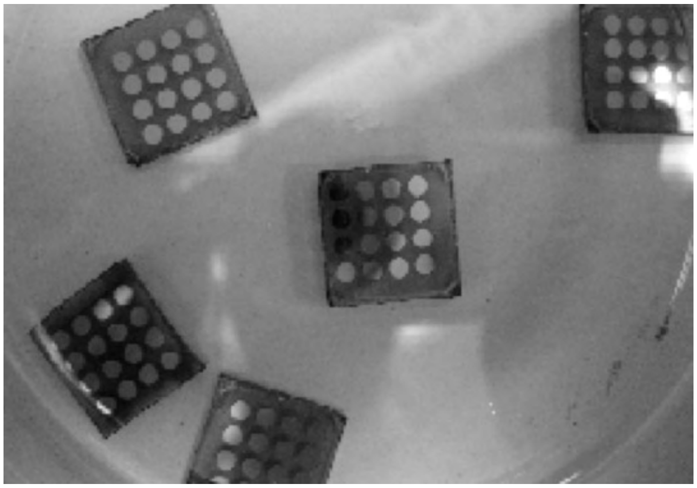

FIGURE 2. Finished devices that have not yet been tested. The P3HT and TiO_2 layer must be scraped away on one area to expose the ITO anode.

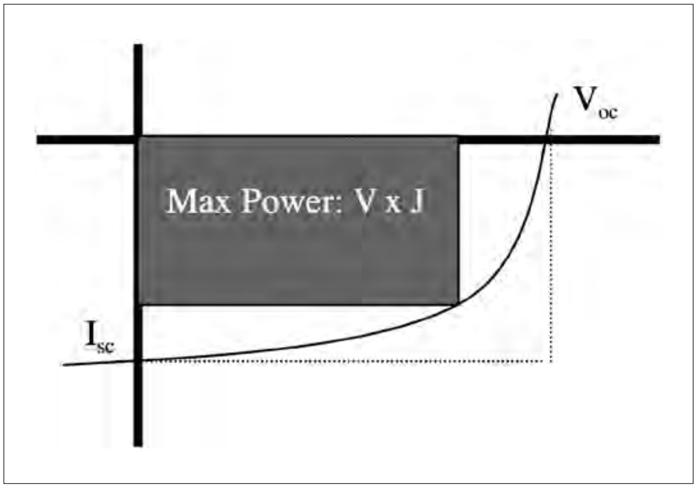

FIGURE 3. An example of solar device curve. An optimal device would have a fill factor of 1, as the bend in the curve becomes more of a sharp turn.

Device and cathode	Open Circuit Voltage (V)	Short Circuit Current (A)	Fill Factor	Power Conversion Efficiency (%)
8.11	0.603022	7.74E-06	0.474906	0.070594
8.15	0.574148	7.59E-06	0.590261	0.081911
8.12	0.433664	5.13E-06	0.338145	0.023935

TABLE 1. Data from the working control device (no iron). Different electrodes on the device were tested and data recorded.

Conclusions

For future work, a repeatable working control device with a PCE of at lease .15% needs to be made. After this has been completed, then the iron doping can start again. When the titania sol-gel was made, half the sol-gel was used for the control, and half was used to add iron nitrate. If the iron nitrate does positively affect the PCE, then an optimized procedure would be the next step to making more efficient devices.

References

1. Lorenzo, E. *Solar Electricity: Engineering of Photovoltaic Systems.* Progensa: Spain, 1994; pp. 260
2. Luscome, C. *Molecular self-assembly for electronic devices: Applications in photovoltaic devices and DNA sensors.* Presentation at UC Berkeley. 2006.
3. Gratzel, M.; *Inorg. Chem.* 2005, vol. 44, 6841-6851.

Acknowledgements

Funds for this research were provided by the Center on Materials and Devices for Information Technology Research (CMDITR), and the NSF Science and Technology Center No. DMR O120967 and the NSF grant supporting the Hooked on Photonics REU program CHE-0453596 I thank Dan Liu, my mentor, for teaching me everything she knows about organic photovoltaics. I thank Dr. Christine Luscombe for supporting me, and as well as the Luscombe group. As well as Steve Hau and Angus Yip for helping me with the machines.

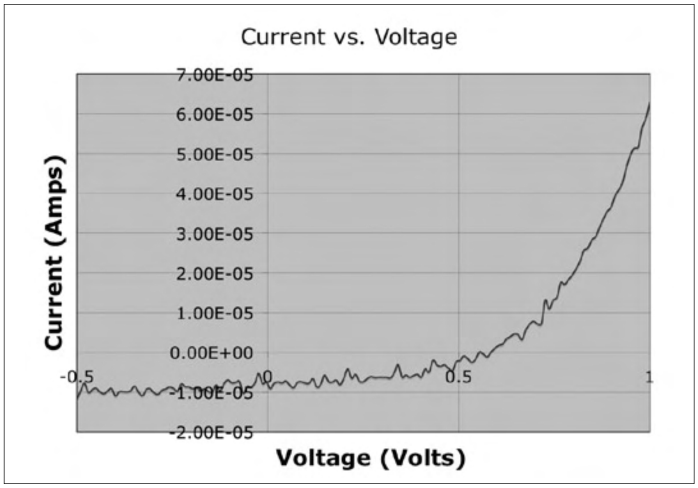

FIGURE 4. Graph of current versus voltage of the working control device. This device had a maximum PCE of .0819%.

NATALIE A. WILHELM I am a sophomore at Brown University in Providence, Rhode Island. I am a biomedical engineering major and plan to continue on with my education in medical school or graduate school.